A Numerical Investigation of the Linear Hydrodynamic Stability of Newtonian and Weakly non-Newtonian Channel Flows as described by the Orr-Sommerfeld Equation

Zareer van der Fort

Thesis presented for the degree of

Master of Science

in the Department of Mathematics and Applied Mathematics

University of Cape Town

November 2009

I know the meaning of plagiarism and declare that all of the work in this document, save for that which is properly acknowledged, is my own.

Abstract

The Orr-Sommerfeld equation describes the growth of infinitesimal disturbances to laminar solutions of the Newtonian Navier-Stokes equations. In this dissertation we consider in part idealised flows between two parallel planes of infinite extent and a finite distance apart. They are referred to as closed channel flows. The Orr-Sommerfeld equation was solved for two such Newtonian closed channel flows (i.e. plane Poiseuille and plane Couette) using the pseudospectral differentiation technique employed by Trefethen[1]. Spectral methods use series of known smooth functions to approximate solutions to differential eigenvalue problems. Our results were in complete agreement with those documented in the relevant literature. We, like Dongarra *et. al.*[2], found an additional eigenmode for plane Poiseuille flow not computed by Orszag[3]. The flow that results from the application of a constant pressure gradient along a channel half-filled with a Newtonian fluid and constant height gravity driven flow down a slope yield equivalent parabolic flow profiles. This hypothetical pressure driven flow amounts to taking the bottom half of the plane Poiseuille flow profile to model free surface (Newtonian open channel) flow. Now, solutions to the Orr-Sommerfeld equation depend only on the steady-state flow profile and boundary conditions of the flow. This motivated an attempt to extend our results to Newtonian open channel flow by using half the plane Poiseuille profile to approximate its profile in the Orr-Sommerfeld equation. Newtonian open channel flow was found to

---

[1] [Tref 01]

[2] [Dong]

[3] [Orsz]

be stable for all Reynolds numbers which contradict instabilities observed in practice. The Orr-Sommerfeld equation does not model variations in the free surface which may be responsible for the instabilities observed in practice. We also investigated the stability of non-Newtonian fluids in flow regimes where their viscosities are nearly constant, i.e. weakly non-Newtonian flows. Here we used the power-law and Ellis models. The steady-state profiles for weakly non-Newtonian power-law flows were not sufficiently smooth and the eigenmodes were numerically unstable. With the Ellis model we obtained some numerically stable results where weakly non-Newtonian pseudoplastic flow was found to be more stable than Newtonian flow. Our results suggest that the shape of a symmetric flow profile influences its stability and that the profile needs to be sufficiently smooth to obtain numerically stable spectra.

Acknowledgements

I am grateful to my supervisors, Dr. H. Laurie and Associate Professor T. G. Myers, for their contributions to this work. And I would also like to thank my family for their patience and support.

Contents

Chapter 1

Introduction

1.1 Hydrodynamic Stability

Understanding how fluids flow is important to a diverse range of fields. In medicine a thorough understanding of blood flow through the body and the heart may certainly contribute to the control or even ultimately to the elimination of heart diseases. Wilcox [Wilc] explains how there is not a branch of engineering that does not contain applications involving fluid motion. The aeronautical and mechanical engineers are responsible for the most obvious achievements, i.e., aircrafts and automobiles. When designing structures like bridges and piers, civil engineers have to consider the effects of aerodynamic and hydrodynamic forces. Electrical engineers require acid to flow in a controlled manner when manufacturing silicon microchips. And chemical engineers must accurately determine reaction rates, which become particularly complicated under turbulent flow conditions.

The Navier-Stokes equations, solved in conjunction with mass and energy conservation equations describe the flow of viscous fluids [Wilc]. But more than 150 years of mathematical analysis has yet to produce a general solution for the Navier-Stokes equation [Coll]. The equations are however easily solvable for elementary flows through simple geometries such as those considered in this dissertation. One such flow is the so-called parallel channel flow in which fluid flows between two parallel planes of infinite extent but a finite distance apart. Such idealised channels allow us to ignore the end-point (entry/exit) effects which are important in channels of finite extent, hence simplifying the analysis. We will consider two such flows, where either:

1. both planes are stationary, the flow is driven by a steady pressure gradient along the channel. The fluid velocity is maximum along the centreline, generating the plane Poiseuille flow profile as illustrated in Figure 1.1,

or

2. the planes are sheared in opposite directions creating the plane Couette flow profile (see Figure 1.2).

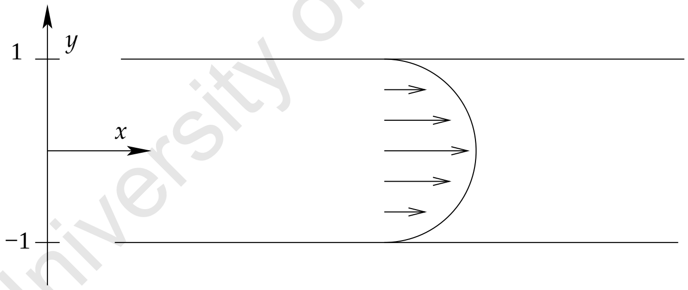

Figure 1.1: Plane Poiseuille flow profile (source: [Coll]).

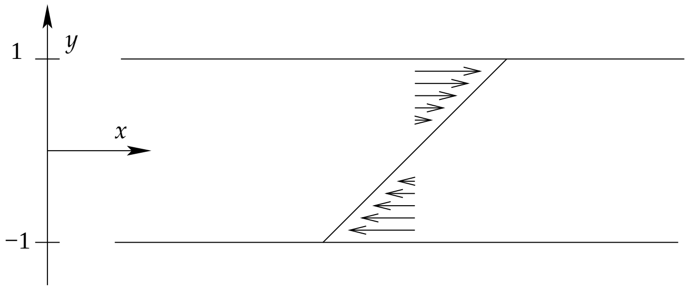

Figure 1.2: Plane Couette flow profile (source: [Coll]).

According to Wilcox [Wilc] if we look close to the solid boundaries we'll observe that the fluid 'sticks' to the planes. Its velocity relative to the boundary is therefore zero. This is known as the no-slip surface boundary condition on the velocity. Both the plane Couette and plane Poiseuille models are solved solved subject to this condition. We are particularly interested in the hydrodynamic stability of these flows, which is concerned with when and how laminar flows break down and the transition to turbulence [Draz]. Steady laminar flow derives its name from the idea that in such motion the fluid can be envisaged as a series of thin plates (i.e. laminae) sliding over each other [Peer]. This motion is not dependent on its position along a channel nor on time.

The modern-day field of hydrodynamic stability was pioneered by Helmholtz, Rayleigh, Kelvin and Reynolds [Draz]. Osbourne Reynolds's classic 19th century experiments, where he injected a streak of coloured dye into clear water flowing in glass tubes, are often used to introduce this subject. The glass tubes were approximately 1 inch, 0.5 inch and 0.25 inch in diameter and 4 feet 6 inches long. Figure 1.3 depicts the original apparatus used by Reynolds. He observed that at sufficiently low velocities the streak of colour extended in a straight line through the tube (see Figure 1.4a). As the velocity was increased, at some point along the tube the streak of dye would instantaneously mix up with the surrounding water and fill the tube with coloured water (see Figure 1.4b). The point of breakdown occurred at a considerable distance from the intake, positioning itself closer to the intake as the velocity was increased further. As depicted in Figure 1.4c, viewing the glass tubes under the light of an electric spark revealed that the mass of colour had resolved itself into distinct curls and eddies. Reynolds showed that the smooth flow (i.e. laminar flow observed at sufficiently low velocities) breaks down when the ratio $\rho U d/\mu$ between the product $\rho U d$ of the mean velocity U of the water, the density ρ of the water and the radius d of the tube and the viscosity μ of the water exceeded a critical value. Today this dimensionless quantity is known as the Reynolds number,

$$R = \frac{\rho U d}{\mu}. \tag{1.1}$$

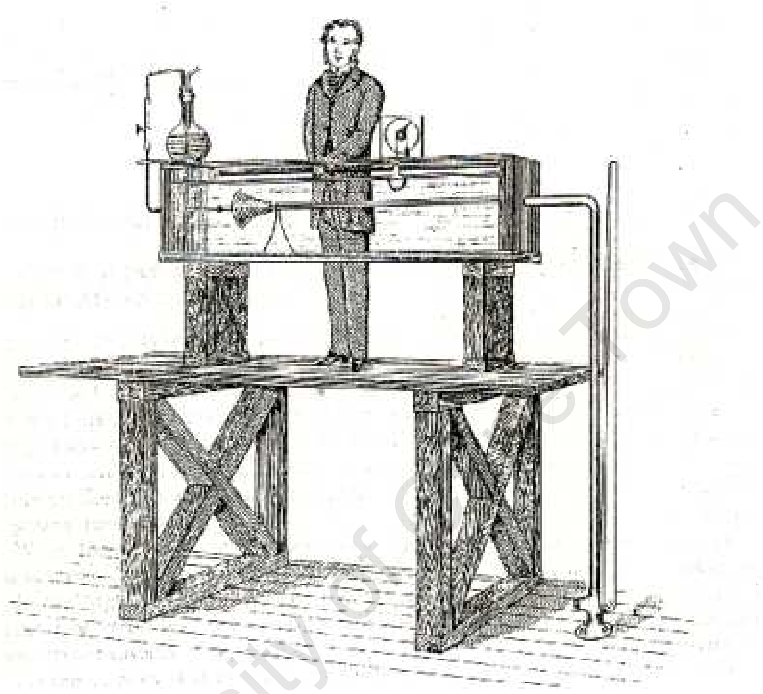

Figure 1.3: Diagram of the apparatus used by Reynolds in his pioneering experiments (source: [Frie], reproduced by scanning).

In his experiments Reynolds determined the critical R, at which his pipe-flows developed into turbulence, to be 13000. He however made it clear that this critical value was not unique. There was no single value beyond which the flow was unstable and below which stable. The matter is considerably more complicated. Reynolds wrote that the critical velocity was very sensitive to the disturbances in the water before entering the tubes, which suggests that the condition might depend on the magnitude of the disturbances. Fluid flows were found to be unstable for disturbances of a certain magnitude but stable for disturbances smaller in size. Acheson [Ache] reports that in taking great care to minimise the disturbances stable flows have been observed at Reynolds numbers up to 90000.

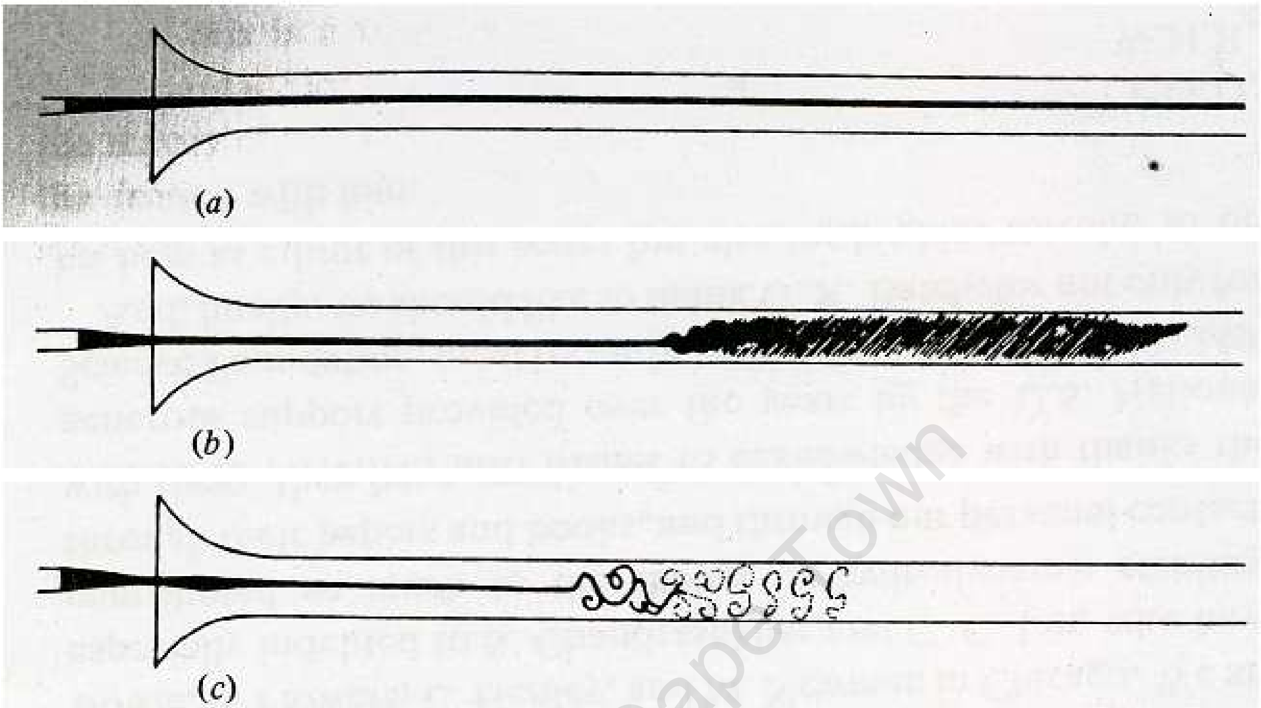

Figure 1.4: Drawings of the observations made in Reynolds's experiments (source: [Draz], reproduced by scanning).

A mathematical analogue to Reynolds experiments is a linear stability analysis of the Navier-Stokes equations. We perform a linear stability analysis, by subjecting basic laminar flow solutions of the Navier-Stokes equations to infinitesimal disturbances. These disturbances can either decay, persist or grow with time. The flow is termed asymptotically stable, neutrally stable, and unstable respectively. This analysis, in which higher orders of the perturbation are ignored, results in the derivation of the Orr-Sommerfeld equation.

1.2 Newtonian Fluids

To the layman a fluid is thought of as anything that flows, liquids and gases being the obvious examples. A more rigorous definition categorises a fluid as a substance that deforms continuously when subjected to a shearing force [Cour]. Or conversely, it is a substance that cannot be in static equilibrium whilst subjected to such a force [Wilc].

Forces acting on the surface of a fluid element (i.e., small volume of fluid) can be resolved into components normal and tangential to the surface. These forces are respectively referred to as normal (i.e., pressure) and shear stresses, where by stress we mean force per unit area. Figure 1.5 depicts a fluid's response to the normal and oblique/shear stresses that results in plane Poiseuille flow. As mentioned above this is achieved by maintaining a constant pressure gradient across the channel. Frictional forces develop at the channel walls to balance this pressure difference [Wilc]. The fluid flows in the manner it does as a result of shear that is due to this friction. Fluids exert pressure whilst stationary or in motion, but shear stresses are only present in moving fluids [Peer]. According to Peerless [Peer] and Wilcox [Wilc], this phenomenon distinguishes fluids from solids. Solid matter can exert shear stresses whilst at rest.

Fluids like honey and oil flow more sluggishly than others, e.g., water. This property which characterises a fluid's ability to resist motion is known as its viscosity and is responsible for the shear stresses mentioned above. Honey is said to be more viscous than water. Viscosity is possessed by all real fluids. Its magnitude μ is expressed as a coefficient that relates the shear stress τ to the shear rate $\dot{\gamma}$, i.e.

$$\tau = \mu\dot{\gamma}.$$

For fluids such as glycerine, water, air and ethanol μ is constant when the pressure and temperature are held constant (see the constant slope shear diagram depicted in Figure 1.6a). Such fluids are known as Newtonian. The actual viscosities of glycerine, water and air at 1 atmosphere pressure and 15°C are shown in Table 1.1.

The term rheology is derived from the Greek 'rheos' meaning flow and 'logos' meaning knowledge [Slat 86]. It therefore encompasses the science of flow phenomena, but in

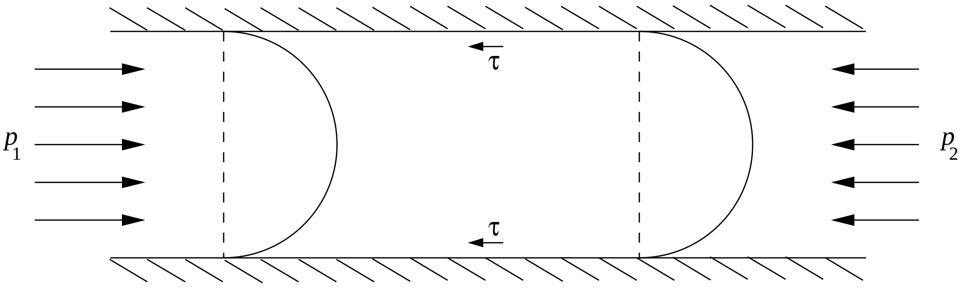

Figure 1.5: A fluid's response to oblique/shear and normal stresses, which results in plane Poiseuille flow. On the application of the pressure gradient ($p_1 > p_2$), the initially rectangular section of fluid moves at different velocities across the channel (source: [Wilc]).

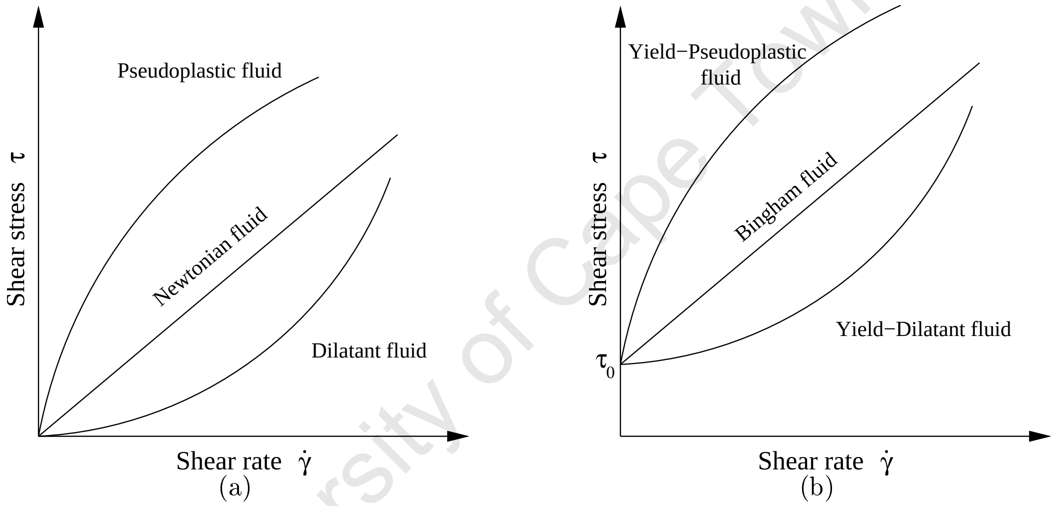

Figure 1.6: Rheograms - typical shear stress-shear strain diagrams for Newtonian and time-independent non-Newtonian fluids. On the right we have the rheograms for viscoplastic fluids that require a force in excess of a yield stress, τ_0 to initiate flow.

	Viscosity
Glycerine	2.3300
Water	1.1405
Air	0.0182

Table 1.1: The viscosities of glycerine, water and air at 1 atmosphere pressure and 15°C (source: [Govi]).

most instances is used to refer to the viscous properties of fluids. The shear diagrams depicted in Figure 1.6 are therefore also referred to as rheograms. Fluids are classified into various rheological types based on the form of their rheograms. The main division is between those fluids that can be described as viscous and those which have both viscous and elastic properties [Govi]. On the removal of a shearing force a purely viscous fluid does not recover from the deformation it may have undergone, whereas a viscoelastic fluid recovers in part. Viscous fluids can be separated into two categories, i.e., time-independent and time-dependent. Time-independent means that the duration that the fluid spends under shear does not effect its rheological behaviour [Mill, Perr]. Newtonian fluids are time-independent.

1.3 Non-Newtonian Fluids

Any fluid that does not obey the aforementioned linear relationship between the shear stress τ and the shear rate $\dot{\gamma}$ is referred to as non-Newtonian. μ becomes known as the apparent viscosity and depends on $\dot{\gamma}\,(t,T)$, where t is time and T temperature [Perr]. The slopes of their rheograms are not constant (see Figures 1.6a and 1.6b). Non-Newtonian fluids are either time-independent, time-dependent or viscoelastic. The non-Newtoninan fluids considered in this dissertation behave like Newtonian fluids for some parameter values and are referred to as generalised Newtonian fluids (GNF's) [Yama].

1.3.1 Time-independent non-Newtonian fluids

According to Perry [Perr], Bingham fluids are probably the simplest of the time independent non-Newtonian fluids. They are to some extent an idealisation, where like Newtonian fluids they exhibit a linear relationship between the shear stress and shear rate. Their respective shear diagrams differ from the Newtonian fluids' only by virtue of not passing through the origin. As depicted in Figure 1.6b, a finite shear stress, referred to as a yield stress (i.e., τ_0) is required to initiate motion. Bingham fluids thus form part of a larger category of fluids known as viscoplastic or 'yield stress' fluids. Toothpaste, chocolate and paint are common examples of Bingham fluids.

When the viscosity of a fluid decreases as its shear rate increases, it is called a shear-thinning or pseudoplastic fluid. Pseudoplastic materials form the majority of non-Newtonian fluids. They are usually solutions of large polymeric molecules in a solvent with smaller molecules. Examples of pseudoplastics include blood plasma and hair styling gel.

Dilatant or shear thickening fluids are less common and exhibit rheological properties opposite to that of pseudoplastics. The apparent viscosity of a dilatant fluid increases with an increasing shear rate. Starch in water, clay slurries and beach sand are examples of dilatant fluids.

Figure 1.6b depicts the shear diagrams of pseudoplastic and dilatant fluids with a yield stress (i.e., viscoplastic fluids). Some of the results in Chapter 4 concern dilatant and pseudoplastic flows.

1.3.1.1 Power-law fluids

Ostwald and de Waele's [Mats] shear stress-shear rate relationship,

$$\tau = K\dot{\gamma}^n, \tag{1.2}$$

is commonly used to represent the rheology of non-Newtonian fluids. These fluids are also known as power-law fluids. K and n are constants that characterise and are particular to specific fluids. n is a measure of how much the fluid deviates from the Newtonian norm and K a measure of its consistency [Hugh]. Setting $K = \mu$ and $n = 1$ reduces (1.2) to the Newtonian flow approximation. A power-law fluid's viscosity is given by

$$\mu = K\dot{\gamma}^{n-1}. \tag{1.3}$$

Both pseudoplastic and dilatant flow behaviour can be approximated using the power-law model. Experimental data are used to obtain best-fit values for K and n. Pseudoplastic and dilatant flows would have $n < 1$ and $n > 1$ respectively. Despite its common use, the power-law model is not without its drawbacks. It fails when attempting to represent the flow behaviour of fluids at very high or very low shear rates. For pseudoplastic fluids where we have $n < 1$, if the shear rate tends to infinity the model predicts that the viscosity would vanish (i.e. tend to 0) and similarly if the shear rate tends to 0 it predicts that its viscosity would be infinite. Both these situations are unrealistic unless the fluid exhibits a yield stress [Darb]. Most fluids as expressed by Darby [Darb] have a "power-law region" outside of which the model tends to be unreliable. Power-law models are therefore only recommended for approximating the flow of fluids over a certain shear rate range. Other drawbacks of this model include that the K and n determined in one flow system is different from that determined in another for the same fluid and that one of its constants has strange dimensions and is dependent on the value of the other [Mats]. In spite of its many defects, theoreticians persist in using the power-law relation outside of its ideal range, presumably as it leads to an attractive analytical model [Myer]. For its simplicity we too start by approximating non-Newtonian flow behaviour using the power-law model. Other non-Newtonian constitutive equations are presented in the context of slurry flows in Section 2.4 and in the linear stability analysis of Chapter 4.

1.3.2 Time-dependent non-Newtonian fluids

Fluids undergo structural changes when subjected to a shearing force. The shear stress observed at a given shear rate varies until an equilibrium structure is achieved. For time-independent fluids the rate of structural reformation is of the same order as the rate of structural decay and hence their fluid behaviour adjusts almost instantaneously to the applied shear stress [Govi]. For some fluids the rate of this reconstruction process is extremely slow and the changes appear to be irreversible. These fluids whose apparent viscosity seem to vary with time at a constant shear rate are classified as time-dependent. If their shear stress is observed to decrease with the duration of shear they are called thixotropic. Non-drip paint and many crude oils exhibit thixotropic behaviour. Figure 1.7a shows the rheogram for Pembina crude oil. The constitutive equations used to describe thixotropy contain several material constants. Moore [Moor] as cited in [Govi] proposed the following two relations to describe the thixotropic behaviour of a fluid without a yield stress,

$$\begin{aligned}\tau &= \frac{1}{g_c}\left(\mu_0 + c\lambda\right)\dot{\gamma} \\ \frac{d\lambda}{dt} &= a - \left(a + b\dot{\gamma}\right)\lambda.\end{aligned}$$

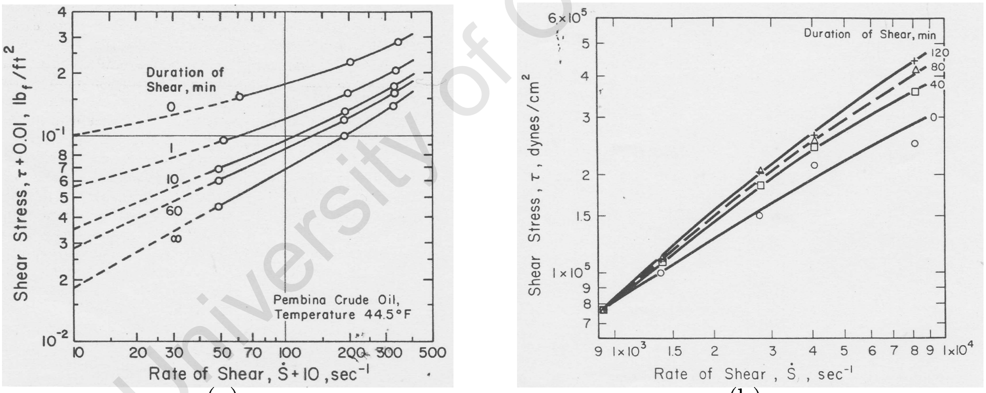

(a) (b)

Figure 1.7: Rheograms for typical (a) thixotropic (crude oil) and (b) rheopectic (2000 molecular weight polyester) fluids (source: [Govi], reproduced by scanning).

μ_0, a, b, c are material constants, g_c is a dimensional constant and λ is a structural parameter having the limit value 0 when the structural configuration of the fluid is fully broken down and 1 when its configuration is fully developed.

Rheopectic or negative thixotropic materials are less common. For such materials the rate of structural reformation, whilst still low exceeds the rate of decay. Its shear stress appears to increase under constant shear conditions. Bentonite solutions and gypsum suspensions in water are examples of Rheopectic materials [Berl]. Bentonite is a very fine clay that can absorb large amounts of water and expand to several times its normal volume. Figure 1.7b shows the rheogram of a typical rheopectic fluid.

1.3.3 Viscoelastic fluids

Viscoelastic fluids form the third category into which non-Newtonian fluids can be classified. They exhibit elastic recovery from the deformations experienced during flow, behaving both as liquids (**visco**us) and solids (**elastic**). Jelly and flour dough display such properties.

We are ultimately interested in the hydrodynamic stability of free surface non-Newtonian flow driven by gravity down an incline. Our interest in this subject stems from the experimental work of Slatter [Slat 95] presented at the end of Chapter 2. He investigates the laminar and turbulent flow of slurries in pipes and the transition between the two regimes. Slatter conducts empirical tests using samples of kaolin clay, uranium tailings and gold slimes tailings. The remainder of this chapter serves as an introduction to slurries, their characteristics and classification according to their settling velocities. To further illustrate the use of the concepts pertaining to slurries we present a study conducted by Charpin *et. al.* [Char 2]. They were tasked with deriving a criterion that can be used to determine when rocks will be set in motion by flowing water. Their analysis included a Reynolds number (equation (1.1)) where the pipe diameter was replaced with the characteristic length of the flow.

How is it that parallel channel flow (see Figures 1.1 and 1.2) can form the basis for an investigation into the hydrodynamic stability of gravity driven flow? We show in Chapter

3 that constant height gravity driven flow down an incline is mathematically equivalent to the flow that results from the application of a constant pressure gradient along a horizontal channel half-filled with a Newtonian fluid. They result in equivalent parabolic velocity profiles. Solutions to the Orr-Sommerfeld equation depend only on the steady-state velocity profile and boundary conditions of the flow. We progress from the simple Newtonian closed channel linear stability problem to the Newtonian open channel and then to the non-Newtonian closed channel by solving the Orr-Sommerfeld equation for their respective velocity profiles and boundary conditions.

Traditional hydrodynamic analysis proceeds in two stages. First the problem is linearised about the laminar solution which results for Newtonian flow in the derivation of the famous Orr-Sommerfeld equation. The Orr-Sommerfeld equation describes the growth of disturbances to the laminar solutions of the Newtonian Navier-Stokes equation. Its derivation is presented in Chapter 3 with the appropriate boundary conditions for closed and open channel flows. The second stage of the traditional stability analysis entails searching for unstable eigenvalues. Now the work of Trefethen *et. al.* [Tref 93] has cast doubt on the use of this eigenvalue analysis but this is not dealt with in this dissertation. As explained above the Orr-Sommerfeld equation applies to Newtonian fluids. We do not derive a non-Newtonian analogue of the Orr-Sommerfeld equation but we use the Orr-Sommerfeld equation to approximate the the stability of weakly non-Newtonian fluids.

Our first objective is to solve the linear hydrodynamic stability problem for plane Poiseuille and plane Couette flows (for Newtonian fluids). Results for these problems are well documented and we are therefore able to compare ours with those found in the literature. Chapter 4 details the pseudospectral numerical scheme employed to solve the Orr-Sommerfeld equation as formulated by Trefethen [Tref 01]. We take an in-depth look at the behaviour of the eigenvalues at various Reynolds numbers by plotting them in the complex plane. Our Newtonian closed channel results are in complete agreement with those found in the literature [Dong, Orsz]. Next we investigate Newtonian open channel flow, where the results seem to suggest that this flow is stable for all Reynolds numbers. The Orr-Sommerfeld equation therefore does not explain the instability observed for this flow in practise. We conclude Chapter 4 by using the OS equation to approximate the stability of weakly non-Newtonian closed channel flows. The power-law and Ellis models are considered. These results seem to indicate (as is supported by the work of Hifdi *et. al.* [Hifd]) that the shape of a symmetric profile influences its stability and that the profiles need to be sufficiently smooth to obtain numerically stable results. The weakly non-Newtonian profiles generated using the power-law model are not sufficiently smooth and hence their eigenmodes are numerically unstable. Numerically stable eigenvalues were obtained for weakly non-Newtonian Ellis flows.

Chapter 2

Slurry Flows

As mentioned in the introduction our interest in hydrodynamic stability analysis originates from experimental work done by Slatter [Slat 95] on the stability of slurry flows. This chapter serves as a brief introduction to slurries and their rheology. As part of his study which we present at the end of the chapter, Slatter showed that a 17% sample of kaolin clay is best modelled as a yield pseudoplastic fluid (see Section 1.3). He also tested how well three existing and three novel Reynolds number formulations predicted the laminar-turbulent transitions. These Reynolds number experiments were conducted using a 17% sample of kaolin clay, uranium tailings and gold slimes tailings. We also include a study conducted by Charpin *et. al.* [Char 2] where they investigated the stability of rocks immersed in water — they determined angles of slopes that will set boulders immersed in flowing water in motion.

2.1 Terminal Settling Velocity

Slurries are two-phase mixtures of small solid particles suspended in fluids. As it will emerge there are numerous variables encountered in these suspensions that cause their flow behaviour to vary over a tremendous range. Different methods of analysis are required to describe their behaviour in various flow regimes. The numerous studies that have been conducted are very specific, investigating the influence of certain variables under certain conditions.

In stationary slurries, if the densities of the suspensions and fluids are not identical, their phases have a tendency to separate and the solid particles settle. There are various factors that influence this phase separation and consequently the rheological properties of a slurry. We commence, as Govier and Aziz do [Govi], by considering a simple slurry, where smooth spherical particles are dispersed in a Newtonian fluid. The particles are scattered so as to avoid collisions and inter-particle interactions. It is also assumed that the system is under the influence of gravity and that neither electrostatic nor external centrifugal forces are present. The combined effect of the flow and gravity cause the particles to rise and fall in the mixture, which results in a drag force (i.e. Stokes drag),

$$F_D = \frac{\pi \rho V^2 d^2 C_D}{8},$$

where C_D is the drag coefficient, V the rise or fall velocity and d the diameter of the particles. ρ is the density of the fluid. Analytically it has been shown and confirmed by experiment that the drag coefficient depends only on the particle Reynolds number, $dV\rho/\mu$, where μ is the viscosity of the fluid [Govi]. Figure 2.1 gives the relationship between the particle Reynolds number and C_D as measured for solid particles with various sphericities (ψ). The sphericity, described in the next section, characterises the shape of a solid particle. The curves show four regions — for $dV\rho/\mu < 1$ the relative motion between particle and fluid is laminar; the region where $1 < dV\rho/\mu < 1000$ represents a gradually developing turbulence in the motion; $1000 < dV\rho/\mu < 2 \times 10^5$ represents fully developed turbulent flow; and for $dV\rho/\mu > 2 \times 10^5$ the boundary layer itself becomes turbulent. In the laminar regime the drag coefficient decreases as the particle Reynolds

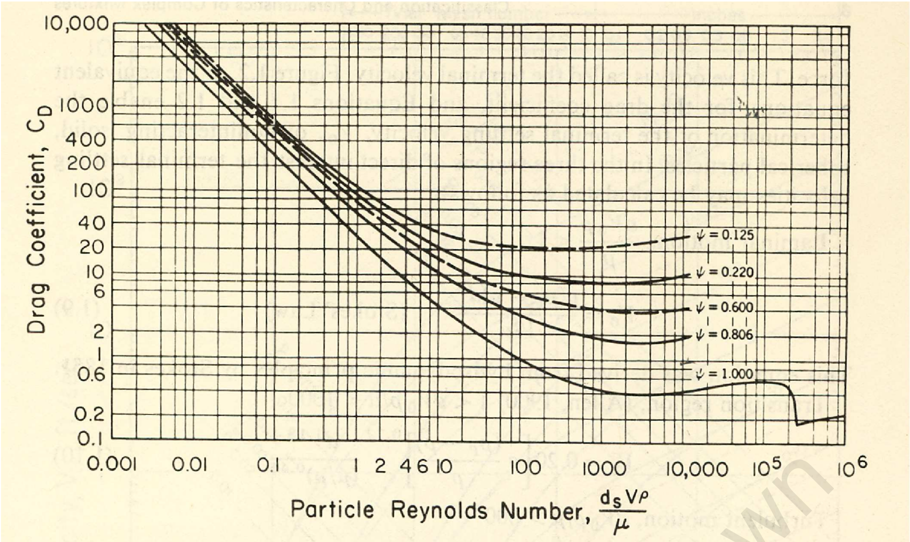

Figure 2.1: The relationship between the drag coefficient and the particle Reynolds number as measured for solid particles with various sphericities, ψ. ψ describes the shape of a solid particle (source: *Brown et. al.* [Brow] cited by [Govi], reproduced by scanning).

Shape	Sphericity, ψ	$\frac{d_s}{d_{av}}$
Sphere	1.000	1.000
Octahedron	0.847	0.965
Cube	0.806	1.240
Prisms		
$a \times a \times 2a$	0.767	1.564
$a \times 2a \times 2a$	0.761	0.985
$a \times 2a \times 3a$	0.725	1.127
Cylinders		
$h = 2r$	0.860	1.310
$h = 10r$	0.691	1.960
Disks		
$h = r$	0.827	0.909
$h = r/3$	0.594	0.630
$h = r/10$	0.323	0.422

Table 2.1: The sphericity and the value of the ratio of the equivalent diameter and screen size for some common shapes (source: *Brown et. al.* [Brow] cited by [Govi]).

number increases. During the development of turbulence, the drag coefficient reaches a minimum and in fully developed turbulence, the drag coefficient increases with the particle Reynolds number. The velocity at which the drag force balances the gravitational force is called the terminal settling velocity [Govi, Slat 95].

2.1.1 The effect of the particle shape on settling

Solid particles are characterised by their shape, size, density and surface roughness. For slurries constituted from irregularly shaped particles, the drag coefficient depends on a Reynolds number based on factors that reflect their irregularity, i.e. particle orientation, shape, etc. The shape of solid particles is expressed by a variable called its sphericity [Govi, Zhan],

$$\psi = \frac{\text{surface area of a sphere of volume equal to that of the particle}}{\text{surface area of the particle}}.$$

The sphericity of regular particles can be calculated directly as their dimensions can be determined. For irregularly shaped particles, Brown *et. al.* [Brow] have shown that

$$\psi = \frac{d_{av}}{nd_s},$$

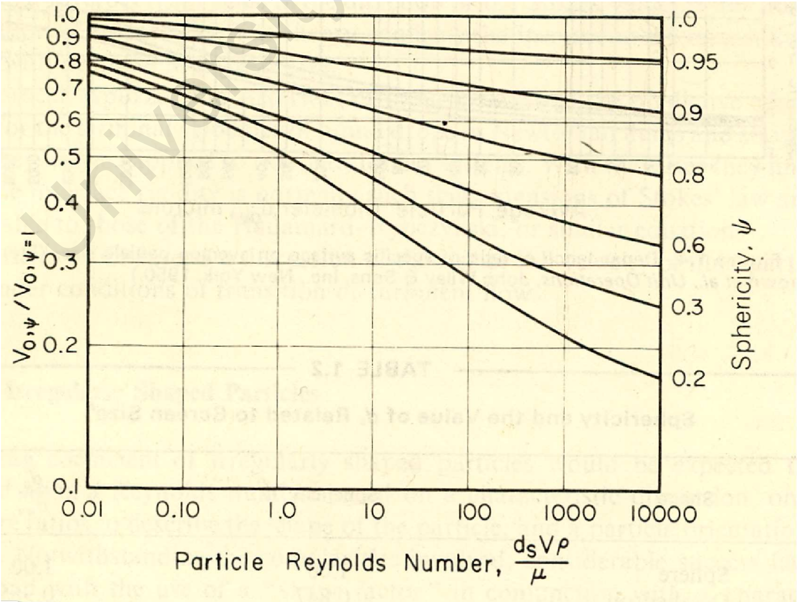

Figure 2.2: The effect of the sphericity ψ on the terminal settling velocity V_0 — for particles of a given ψ, V_0 is shown as a function of the particle Reynolds number. V_0 is scaled using the settling velocity of a perfect sphere, $V_{0,\psi=1}$ (source: [Govi], reproduced by scanning).

where d_{av} is the nominal size based on screen or microscopic analysis (i.e. average screen size), d_s is the equivalent diameter and n the ratio of the surface per unit mass of the particles to that of spheres of diameter d_{av} [Govi, Zhan]. The equivalent diameter is the diameter of a sphere having the same volume as the particle. Table 2.1 shows the sphericity and the value of d_s related to the screen size for some common shapes. A spherical particle has sphericity 1, i.e. $\psi = 1$. Figure 2.2 depicts the relationship between the sphericity and the terminal velocity, V_0. As the sphericity of a solid particle decreases, the drag that it experiences increases (see Figure 2.1) and its settling velocity decreases.

2.1.2 The effects of the particle concentration on settling

The solid-liquid ratio of suspensions are expressed in various forms. Coussot [Cous] for example recommends the use of the solid volume concentration as opposed to the solid weight concentration to quantify the relative amount of solid present in a mixture. The solid volume concentration is expressed as a ratio of the volume of the solid to the total volume of the mixture, referred to by Govier and Aziz as the volume fraction,

$$\phi = \frac{\text{volume of solid}}{\text{volume of liquid} + \text{volume of solid}}.$$

ϕ is also referred to as the solid fraction. An increase in the volume fraction of slurries increases the probability of inter-particle interactions. These interactions do not alone depend on the volume fraction, but are strongly influenced by the flow regime of the slurry (i.e. laminar or turbulent). When particles collide certain particles gain speed and others slow down. Some particles may stick together and form clusters (i.e. agglomerate). The effects of concentration increases on slurries in the laminar regime have been dealt with theoretically. Famularo and Happel [Famu] as cited by [Govi] derived an expression for the ratio of the laminar settling of vertically orientated doublet spheres to that of single spheres and showed that

$$\frac{V_c}{V_0} = \frac{1}{\lambda\left(1 + 2.8\lambda\gamma c^{\frac{1}{3}}\right)},$$

d/x	Resistance coefficient λ
0.000	1.000
0.266	0.836
0.648	0.702
1.000	0.645

Table 2.2: The dependence of λ on the centre-to-centre distance x of the spheres in the doublet (source: [Govi]).

where λ is a resistance coefficient dependent on the centre-to-centre distance in the doublet (see Table 2.2) and γ is constant in the range of 1.30 ± 0.24. V_c is the settling velocity of particles in a concentration c and V_0 is the settling velocity of a single sphere. Govier and Aziz [Govi] remark that the significance of this equation is that it shows that the agglomeration even to doublets increases the settling velocity. Where agglomeration does not occur the laminar settling velocities of slurries are reduced by an increase in concentration.

Having looked at the effects of the particle concentration on the settling velocity under laminar flow conditions, we next turn our attention to the turbulent regime. Turbulent mixing increases the number and effects of inter-particle collisions, which increases with an increase in the concentration. If the particles have no tendency to agglomerate, the larger particles slow down whilst the smaller particles gain speed when they collide. Collisions hinder the settling rates of these mixtures. The particles settle at velocities lower than when there are no or significantly fewer collisions. This process is aptly termed as hindered settling.

2.2 Slurry Case Study I - Charpin *et. al*

We now present the work of Charpin *et. al*. [Char 2] involving the turbulent free surface flow of a rock slurry. Their analysis incorporates a Reynolds number where the pipe diameter d in equation (1.1) is replaced with the characteristic length of the flow. They determine a critical value, namely the gradient of the slope that will set large rocks in motion and the effect of the slurry concentration on this value.

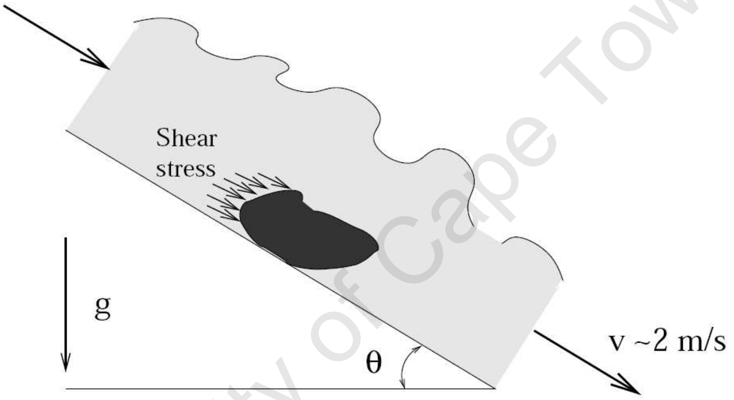

Figure 2.3: Typical configuration for large boulders in Charpin *et. al.*'s study (source: [Char 2], reproduced by scanning).

In the problem we are considering a mineral processing plant produces hundreds of thousands of tons of waste material. The waste consist of rocks ranging from less than a millimetre to 20 centimetres in diameter. High pressure water is used to wash the rocks down a slope to a pond 3km away and approximately 300m lower. The water-rock slurry carves approximately a 1 metre by 1 metre channel, whose slope decreases progressively as the waste source (mining area) slowly moves away from the pond. For the conditions under consideration the flow is turbulent with Reynolds numbers well above 10^6. Because of the high fluid velocity, the average of which is between $v = 1\text{m.s}^{-1}$ and $v = 2\text{m.s}^{-1}$, Charpin *et. al.* [Char 2] assume that the smaller particles will be carried away easily. In their study they determine criteria for which the larger rocks (i.e. typically 20 centimetres in diameter) will be set in motion.

As illustrated in Figure 2.3, the two main forces acting on a boulder are the shear stress due to the flow and gravity. The potential movement of the boulder depends on the non-dimensional Shields number, a ratio between the main forces and the shape of the boulder, i.e.

$$S = \frac{\tau}{\triangle \rho g D}, \tag{2.1}$$

where τ is the shear stress, $\triangle\rho$ is the difference between the densities of the boulder and water, g gravity and D the diameter of the rock. Charpin *et. al.* use the critical Shields number to derive an analytical expression for the minimum angle of the slope of the channel required to move the larger boulders. Critical Shields numbers can be found in [Juli] as cited by [Char 2]. Below this critical value gravity dominates and the boulder remains stationary, but as soon as it is exceeded the shear stress is dominant and the boulder is set in motion. For the turbulent flow under consideration τ according Patel [Pate] as cited in [Char 2] may be expressed as

$$\tau = \frac{f}{8}\rho_f u^2, \tag{2.2}$$

where the friction factor is,

$$f = \frac{0.292}{Re^{\frac{1}{4}}}, \tag{2.3}$$

and the Reynolds number is,

$$Re = \frac{\rho_f u L}{\mu_f}. \tag{2.4}$$

L is a typical length of the flow, u the fluid velocity, ρ_f the density of the mixture and μ_f its dynamic viscosity. L is typically around 1m. The density of the mixture and viscosity vary significantly with the concentration of soil particles in the fluid mixture [Char 2]. The density increases with the particle concentration, c,

$$\rho_f = \rho_w + c\left(\rho_b - \rho_w\right), \tag{2.5}$$

where ρ_b and ρ_w are the densities of soil and pure water respectively. The dynamic viscosity may be approximated by

$$\mu_f = \mu_w \left(1 + \frac{0.75c}{0.605 - c}\right)^2, \tag{2.6}$$

where μ_w is the dynamic viscosity of pure water, see [Cous] in [Char 2]. Combining equations (2.2)-(2.6) for these terms together with the Shields number (2.1) results in the following expression for the fluid velocity,

$$u^{7/8} = \sqrt{\frac{8gDS\left(\rho_b - \rho_w - c\left(\rho_b - \rho_w\right)\right)}{0.292\left(\rho_w + c\left(\rho_b - \rho_w\right)\right)}} \left(\frac{\left(\rho_w + c\left(\rho_b - \rho_w\right)\right)L}{\mu_w\left(1 + \frac{0.75c}{0.605-c}\right)^2}\right)^{1/4}. \tag{2.7}$$

The velocity may be related to the slope of the channel using the Glaucker-Manning formula,

$$u = \frac{1}{n} R_H^{2/3} \sqrt{\sin\theta}, \tag{2.8}$$

where n is the Manning coefficient and R_H denotes the hydraulic radius ([Chan] as cited in [Char 2]). The Manning coefficient and the hydraulic radius are measures of roughness and a river's ability to move water and sediment respectively. R_H is used by engineers to assess the likelihood of flooding. For the earth's surface $n = 0.025$ and for gravel $n = 0.029$. Charpin *et. al.* takes $n = 0.027$. Substituting (2.7) into (2.8), the slope of the channel may be expressed as

$$\theta = \arcsin\left[\frac{n^2}{R_H^{\frac{4}{3}}}\left(\frac{8gDS}{0.292}\left(\rho_b-\rho_w\right)\left(1-c\right)\right)^{\frac{8}{7}}\left(\frac{1}{\left(\rho_w+c\left(\rho_b-\rho_w\right)\right)^3}\frac{L}{\mu_w\sqrt{1+\frac{0.75c}{0.605-c}}}\right)^{\frac{2}{7}}\right]. \tag{2.9}$$

It has been mentioned that the critical Shields number can be obtained from the literature. Corresponding to the current setting the critical Shields number reads

$$S_c = 0.06\tan\phi_s,$$

where ϕ_s is the angle of repose (Julien [Juli] cited by Charpin *et. al.*). The angle of repose is the critical angle of the channel floor to the horizontal that would cause a boulder to move without fluid motion. For a sphere, the angle of repose equals 0 and it increases with angularity. The angularity is a shape factor analogous to the sphericity discussed in Section 2.1.1. It is the degree to which a rock has sharp or rounded edges or corners [Mars]. To finally arrive at an analytical expression for the angle of the slope needed to set a boulder in motion, Charpin *et. al.* replace S in (2.9) with S_c,

$$\begin{aligned}\theta = {} & \arcsin\left[\frac{n^2}{R_H^{\frac{4}{3}}}\left(1.64gD\tan\phi_s\left(\rho_b-\rho_w\right)\left(1-c\right)\right)^{\frac{8}{7}}\right.\\ & \left.\times\left(\frac{1}{\left(\rho_w+c\left(\rho_b-\rho_w\right)\right)^3}\frac{L}{\mu_w\sqrt{1+\frac{0.75c}{0.605-c}}}\right)^{\frac{2}{7}}\right].\end{aligned}$$

For a given boulder θ depends on characteristics which include its angle of repose and diameter. Figures 2.4a and 2.4b show the θ required to move boulders with a diameter varying up to 0.2m and an angle of repose up to 50° in volumetric concentrations of $c = 0.1$ and $c = 0.3$ respectively. The numerical results of Charpin *et. al.* indicate that:

- θ decreases with particle concentration,

- as expected, θ is significantly lower for small particles, and
- θ increases as ϕ_s increases, i.e. the larger the boulder's angle of repose, the steeper the slope of the channel required to move it.

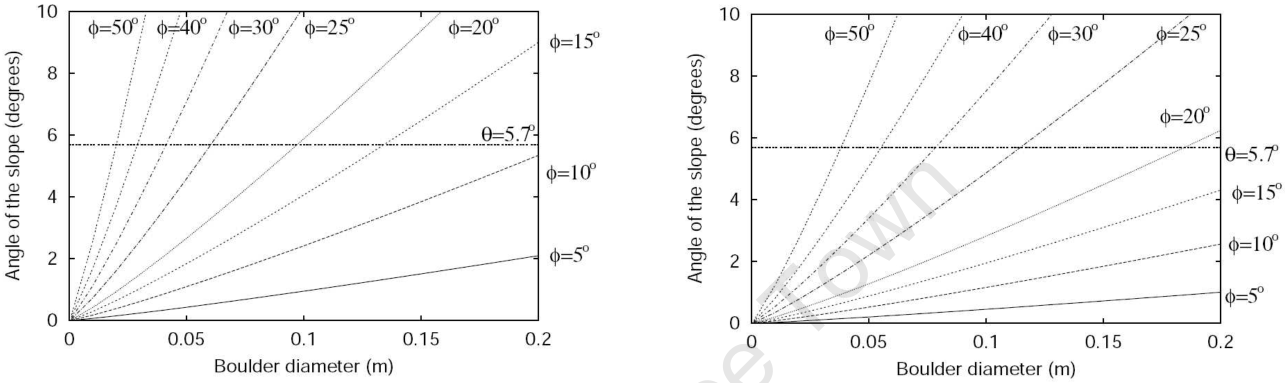

(a)

(b)

Figure 2.4: Slope angle, θ required to move a boulder as a function of its diameter and angle of repose, ϕ. ϕ is a measure of angularity (i.e. a shape factor). The particle volumetric concentration $c = 0.1$ in (a) and $c = 0.3$ in (b) (source: [Char 2], reproduced by scanning).

2.3 Slurry Categorisation

From the short discussion on phase separation (Section 2.1) it is evident that a range of variables influence the terminal settling velocities of slurries. The size, shape, density and concentration of the particle and density and viscosity of the fluid are among these factors. It is widely accepted that there are basically two broad categories into which slurries can be classified, i.e., heterogeneous and homogeneous. These classifications can be made according to the settling velocities of the respective slurries but they are neither absolute nor exclusive.

As mentioned in the introduction, slurries that settle quickly, like those comprised of large particles (e.g., coarse sand) are referred to as heterogeneous or settling slurries

[Bake, Slat 95, Govi]. These slurries have high settling velocities. Under the influence of gravity some particles settle and the suspensions are no longer uniformly distributed, i.e. heterogeneous. The continuum assumption, where the fluid's physical characteristics are assumed to be continuous in time and space becomes void [Cous, Darb].

Homogeneous slurries, as referred to by Slatter [Slat 95] and Darby [Berl] amongst others, have low settling velocities. But no mixture consisting of two different phases is truly homogeneous. Hence, Govier & Aziz [Govi] prefer to refer to them as pseudo-homogeneous slurries. The term homogeneous is used by authors to convey the idea that the solid particles are uniformly distributed. The particles are normally fine and in high concentrations (e.g., fine clay). This alters the rheological behaviour of the fluid and the mixtures often display non-Newtonian viscous effects. The flow regime affects the settling of particles and would affect the categorisation of a slurry. Certain mixtures normally classified as heterogeneous in the laminar regime, may remain homogeneous as result of the mixing action under turbulent conditions. Thomas [Thom 64, Thom 61a, Thom 61b] as cited in [Govi] has shown that a dilute suspension of fine particles becomes homogeneous as a result of a lift force that develops under turbulent flow conditions. The force prevents a large scale deposition of the particles on the pipe boundary.

Eventually the larger dense particles of slurry mixtures settle and form a bed on the bottom boundary. Particles in the bed tend to form 'dunes' and if the shearing force is large enough, these dunes appear to slide along the bottom. If this force is not large enough, the bulk of the bed remains stationary but particles at the surface may move along in a bouncing-type motion called saltation [Darb]. Slurries comprised of particles of varying settling velocities are called mixed regime slurries [Slat 95]. Such slurries are both homogeneous and heterogeneous in that the larger particles will settle, whilst and the smaller fine particles remain suspended.

2.4 Slurry Rheology

Model name	**Viscosity function**
Power-Law	$\tau = K\dot{\gamma}^n$
Bingham	$\tau = \tau_0 + \mu_\infty\dot{\gamma}$
Hershel-Bulkley	$\tau = \tau_0 + K\dot{\gamma}^n$
Casson	$\tau^{\frac{1}{2}} = \tau_0^{\frac{1}{2}} + (\mu_\infty\dot{\gamma})^{\frac{1}{2}}$

Table 2.3: Viscosity functions commonly used to model slurry flows (source: [Darb, Kita]).

At sufficiently dilute concentrations, slurries normally behave as Newtonian fluids [Char 1, Govi]. Their viscous properties deviate from this Newtonian norm as their solid volume fractions increase. We focus on the rheological behaviour of homogeneous slurries. They are mixtures of high concentrations of solid particles and are commonly modelled as non-Newtonian fluids. Various rheological data are required to appropriately classify these slurries as particular non-Newtonian fluids. But generalisations based largely on empirical observations have been made. The fluid model parameters are applied to get a best fit to the experimental data. This involves constructing a rheogram (i.e., shear stress versus shear rate plot). Many of the early studies seemed to suggest that non-Newtonian flows approximated Bingham fluids. Baker and Jacobs [Bake] remark on the difficulty associated with gathering reliable and accurate rheological data. As a result researchers experienced great trouble in distinguishing between Bingham fluids and pseudoplastic fluids. In response, Hershel and Bulkley proposed combining the Bingham and power-law models, to form what is today known as the Hershel-Bulkley model listed in Table 2.3. If $\tau_0 > 0$ then this generalised model characterises Bingham, yield pseudoplastic and yield dilatant fluids for $n = 1$, $n < 1$ and $n > 1$ respectively, i.e. the viscoplastic fluids reviewed in Section 1.3.

Having briefly looked at a development of non-Newtonian fluid models, we take a closer look at such models commonly used to represent slurry flow behaviour, i.e. the Bingham, Hershel-Bulkley, power-law and Casson models. Recall from Section 1.3 that the power-law model is only useful for representing fluid flow over a finite range and that it cannot be used to extrapolate beyond this range. The Casson and Bingham models resemble each other. They both exhibit a yield stress (i.e. τ_0), a limiting viscosity (μ_∞) and shear thinning behaviour. Their viscosities as functions of the shear rate respectively read

$$\begin{aligned} \mu &= \frac{\tau_0}{\dot{\gamma}} + \mu_\infty && \text{(Bingham)} \\ \mu &= \left[\left(\frac{\tau_0}{\dot{\gamma}} \right)^{1/2} + (\mu_\infty)^{1/2} \right]^2 . && \text{(Casson)} \end{aligned}$$

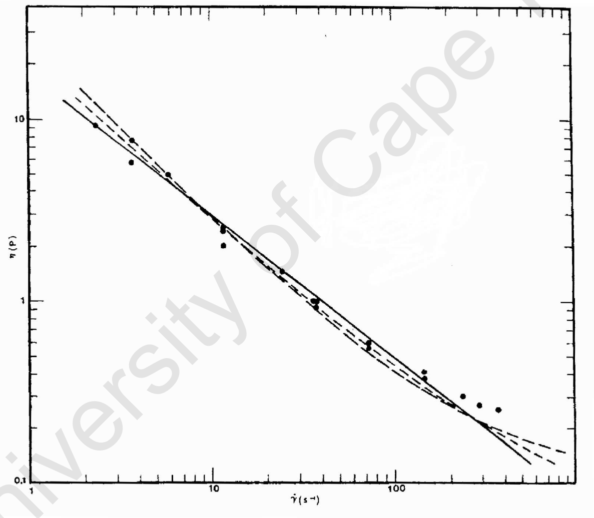

Figure 2.5: Viscosity vs. shear rate for 45% lignite in methanol. (——) – best fit by power-law model; (— —) – best fit by Bingham model; (– – –) – best fit by Casson model (source: [Darb], reproduced by scanning).

As the shear rate (stress) increases both these models approach Newtonian behaviour with viscosity μ_∞. At low shear rates (i.e. tending to zero) they predict that a fluid's viscosity would be infinite, meaning that the fluid possesses a yield stress. Therefore unlike the power-law model, the Casson and Bingham models exhibit the appropriate limiting behaviour at both high and low shear rates. Concentrated slurries exhibit a yield stress. Both these models are therefore very useful for representing their viscous properties [Darb]. The Casson model is the most broadly used model to represent blood flow [Neof]. The Hershel-Bulkley model is essentially a power-law model with a yield stress. It has an additional parameter, n which makes it more flexible than the Bingham model when determining a best-fit to the data. But despite its additional flexibility, at high shear rates the Hershel-Bulkley model has the same drawbacks as the power-law model — for $n < 1$ they both predict that the viscosity is negligible at high shear rates. Vlasak and Chara [Vlas] state that a great number of fine-grained slurries are modelled as yield pseudoplastic fluids. Wilson and Thomas [Thom 87] fitted data obtained from experiments performed on a 7.5% kaolin clay sample to both a Bingham and Hershel-Bulkley models. Statistically the latter provided the better fit. They continued to examine the rheology of kaolin clay at various concentrations and discovered that the best-fit value of n in the Hershel-Bulkley model decreases with an increasing concentration. Their claim that this behaviour is typical of most slurries is supported by [Vlas], who added that the consistency index K and the yield stress τ_0 increase with an increasing concentration. In his review of the hydrodynamics of slurries, Darby presents a similar study, where the flow of lignite suspensions in methanol at 45% and 60% solid weight concentrations were investigated. Figure 2.5 depicts his least squares fit to the Casson, Bingham and power-law models for a 45% concentration of the suspension. Statistically the Casson model provided the best fit and the power-law model the worst-fit to the 45% sample, whereas the power-law and Bingham provided the best and worst fits respectively to the 60% sample. These differences appear to be negligible for the shear rate range in which these measurements were obtained (see Figure 2.5). Either of these models could provide adequate representations of the lignite-methanol mixture's rheology. If it were necessary to extrapolate beyond this range, the Casson and Bingham models would be preferred because of their limiting behaviour.

2.5 Slurry Case Study II - Slatter

Model	τ_0	K	n	Error
Yield pseudoplastic	7.040	0.26710	0.5880	0.66
Pseudoplastic	-	5.03700	0.1723	0.86
Bingham plastic	8.192	0.02779	1.0000	0.76

Table 2.4: Best fit values for the rheological parameters of the yield pseudoplastic, pseudoplastic and Bingham models computed by [Slat 95] using data obtained from [Xujg] (source: [Slat 95]).

As part of his doctoral thesis, Slatter [Slat 95] examined the laminar and turbulent flow of slurries in pipes and the transition from the former regime to the latter. He conducted empirical tests using samples of kaolin clay, uranium tailings and gold slimes tailings. In his analysis he showed that the laminar flow of these slurries are best modelled using the Hershel-Bulkley (yield pseudoplastic) model described in Section 2.4. Slatter's primary objective was to construct a non-Newtonian Reynolds number. He first tested existing non-Newtonian Reynolds number formulations and thereafter three of his own.

For the laminar flow analysis, Slatter used experimental data obtained from Xu *et. al.* [Xujg] who conducted tests on a 17% sample of kaolin clay. He performed a least squares fit to compute the optimum values of τ_0, n and K in

$$\frac{8V}{D} = \frac{4n}{K^{\frac{1}{n}}\tau_w^3}\left(\tau_w - \tau_0\right)^{\frac{1+n}{n}}\left[\frac{\left(\tau_w - \tau_0\right)^2}{1+3n} + \frac{2\tau_0\left(\tau_w - \tau_0\right)}{1+2n} + \frac{\tau_0^2}{1+n}\right], \tag{2.10}$$

for the yield pseudoplastic, pseudoplastic ($\tau_0 = 0$) and Bingham ($n = 1$) models. $\tau_w = D\triangle p/4L$ is the wall shear stress, V is the mean slurry velocity and $\triangle P$ is the pressure difference across a pipe of length L and diameter D. Equation (2.10) is derived from the yield pseudoplastic model. A full derivation of this "supermodel" (i.e., it reduces to various other models for special parameter values) is provided in [Govi] and [Slat 95]. Table 2.4 shows the optimum values for these models according to the least squares error function.

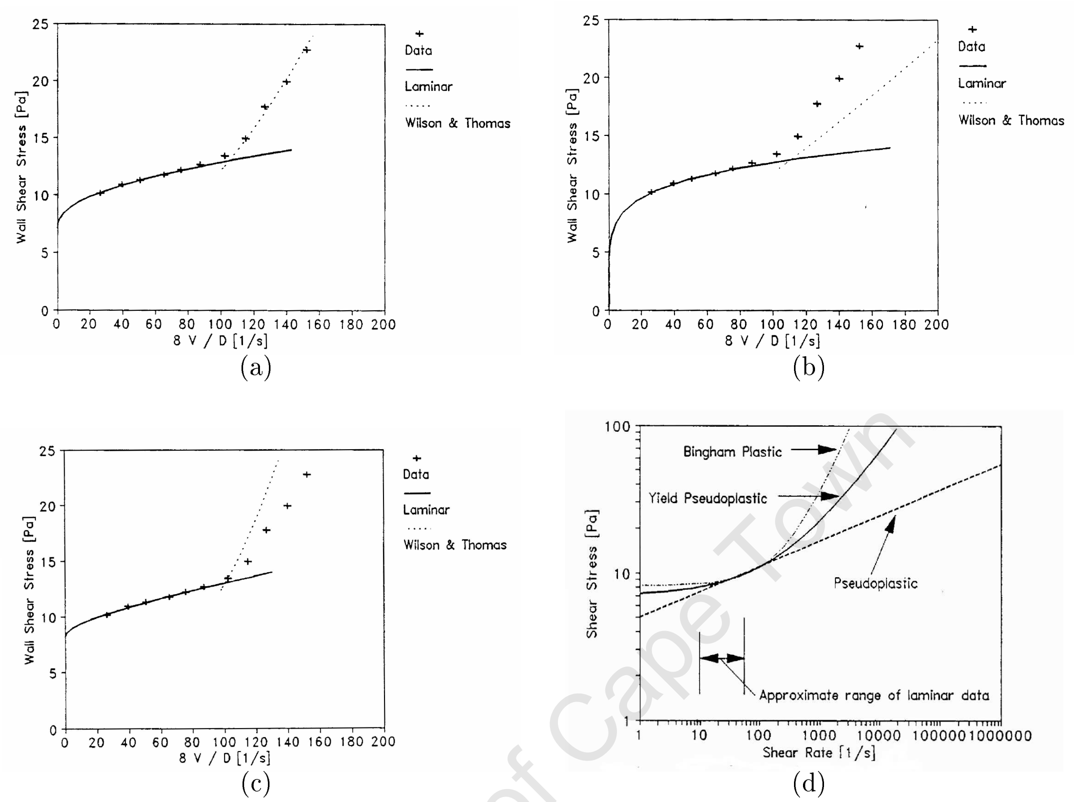

(a) (b)

(c) (d)

Figure 2.6: (a) Yield pseudoplastic, (b) pseudoplastic and (c) Bingham least squares fits for a 17% sample of kaolin clay. (d) depicts the models extrapolated to high shear rates (source: [Slat 95], reproduced by scanning).

Figures 2.10a - 2.10c depict the resulting fits to the yield pseudoplastic, pseudoplastic and Bingham models respectively together with the Wilson & Thomas ([Thom 85] as cited in [Slat 95]) turbulent flow predictions. Each of these laminar models appear to predict the laminar flow of the slurry sample equally well but at high shear rates they differ (see Figure 2.10d).

The transition from the laminar to turbulent flow regime of a specific Newtonian fluid in a given pipeline is determined by a critical fluid velocity. Provided disturbances to the flow are kept sufficiently small, Reynolds and many others after him have suggested that this transition occurs at a fixed value of the ratio between the inertial and viscous forces called the Reynolds number,

$$R = \frac{\rho V D}{\mu}, \tag{2.11}$$

where ρ is the fluid density, V the average fluid velocity, D the pipe diameter and μ the fluid viscosity [Ache, Draz, Slat 95]. Slatter used $R = 2100$ as the critical Reynolds number for Newtonian flows. His objective was to provide a single laminar/turbulent transition criterion for non-Newtonian slurries which proves to be considerably harder. There are many different approaches but no guidelines as to which is more accurate. He commences by investigating the success with which three existing formulations/models predict the transition. We present the details of two of these formulations,

$$R_{\text{newt}} = \frac{\rho V D}{\mu'} \quad \text{and} \quad R_{\text{mr}} = \frac{8\rho V^2}{K'\left(\frac{8V}{D}\right)^{n'}}. \tag{2.12}$$

R_{newt} is based on the standard Newtonian theory where the Reynolds number is given as in (2.11). But for non-Newtonian fluids we know that the viscosity function is no longer constant. It is therefore replaced with an apparent or secant viscosity, $\mu' = \frac{\tau_w}{-\frac{\partial u}{\partial r}\big|_w}$ derived from the Hershel-Bulkley model in Table 2.3, where w denotes the pipe wall and r the distance from its centre. As illustrated in Figure 2.7, for a given shear rate measurement, μ' is the slope of the straight line extended from the origin to the corresponding τ_w-value on the shear stress-shear rate curve of a particular fluid. μ' is not constant and needs to be computed for each value in the shear rate/shear stress range. It is also evident that for any fluid with a yield stress, μ' is arbitrarily large at infinitesimally small shear rates (i.e. $\mu' \to \infty$ as $-\frac{\partial u}{\partial r} \to 0$ - see Figure 2.7).

Metzner and Reed developed a generalised Reynolds number, R_{mr} [Metz]. It is not based on a specific fluid's rheological properties or an existing model (e.g., Bingham, Yield pseudoplastic, etc.). We provide a brief overview of their derivation. The Rabinowitsch-

Mooney equation,

$$-\left.\frac{\partial u}{\partial r}\right|_w = \frac{8V}{D}\left(\frac{3n'+1}{4n'}\right), \tag{2.13}$$

relates the true wall shear rate, $-\left.\frac{\partial u}{\partial r}\right|_w$ to the measurable pseudo shear rate, $\frac{8V}{D}$. n' is obtained geometrically by determining the slope of a logarithmic plot of $D\triangle P/4L$ vs. $8V/D$.

$$n' = \frac{\partial\left(\ln D\triangle P/4L\right)}{\partial\left(\ln \frac{8V}{D}\right)}, \tag{2.14}$$

where $\triangle P$ is the pressure difference across a pipe of length L and diameter D. For a great number of non-Newtonian fluids Metzner and Reed report [Metz] that n' was found to be nearly constant over wide shear stress ranges. Hence for such a shear stress range equation (2.14) reduces to

$$\frac{D\triangle P}{4L} = K'\left(\frac{8V}{D}\right)^{n'}, \tag{2.15}$$

where K' is a constant. Denoting the shear stress at the pipe wall $D\triangle P/4L$ as τ_w and combining equations (2.13) and (2.15) results in,

$$\tau_w = K'\left(\frac{4n'}{3n'+1}\right)^{n'}\left(\left.\frac{-\partial u}{\partial r}\right|_w\right)^{n'},$$

where for $n' = 1$ we have the Newtonian viscosity relation. K' and n' are like the fluid consistency and flow behaviour indices of the power-law model (see Section 1.3). The larger the value of K' the thicker or more viscous the fluid. n' is a measure of the degree of the fluid's non-Newtonian behaviour, for $n' < 1$ the fluid is pseudoplastic in character and for $n' > 1$ it would exhibit dilatant behaviour. Slatter [Slat 95] refers to K' and n' as the apparent fluid consistency and flow behaviour indices respectively. In the final step of this mathematical development, Metzner and Reed relate the pressure drop to the Fanning friction factor which enables the measurement of the latter and consequently

R_{mr}. The friction factor is a dimensionless quantity defined in terms of the shear stress at the pipe wall,

$$f = \frac{2g_c\tau_w}{\rho V^2},$$

where $g_c = 32.2\mathrm{ft.lb.}$ is a conversion factor [Metz, Wilc]. Setting $f = 16/R$ as for laminar Newtonian flow, results in Metzner and Reeds's generalised Reynolds number (R_{mr} in equation (2.12)). The significance of these equations are that they state that all fluids must follow the $f = 16/R_{\mathrm{mr}}$ relation in the laminar regime. Metzner and Reed suggested that this relation even be used to test the accuracy of experimental data. If perfect coincidence is not achieved with the $f = 16/R_{\mathrm{mr}}$ line in the laminar regime then either the data or calculations are in error or the fluids exhibit rheopectic or thixotropic behaviour.

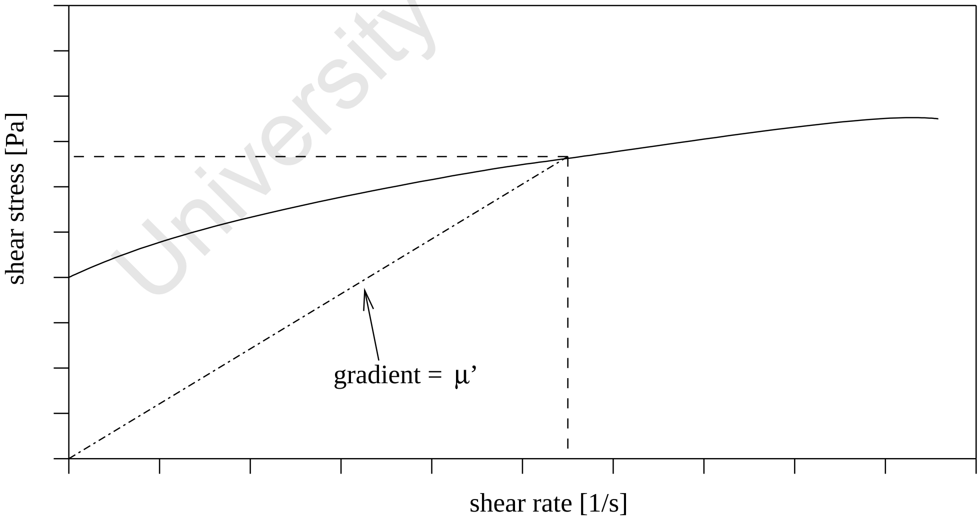

Figure 2.7: Illustration of the apparent viscosity μ' for some fluid (source: [Slat 95], reproduced by scanning).

A full reading of the Torrance/Clapp Reynolds number, R_{torr} the third formulation tested by Slatter may be found in [Clap].

	R_{newt}	R_{mr}	R_{torr}
Average	5715	3268	10057
Std Deviation	2912	981	8535
Std Deviation %	51	30	85
Minimum	2169	1516	2382
Maximum	12610	6451	40183
Range	10441	4935	37801

Table 2.5: Non-Newtonian Reynolds numbers - computed using the rheological parameters obtained from the least squares fits and the observed critical velocities. The results have been reduced to their averages, standard deviations and ranges (source: [Slat 95]).

In addition to the three existing Reynolds numbers, Slatter analysed the accuracy with which the intersection method and a stability function predicts the laminar/turbulent transition. The intersection method is a purely practical approach where the transition is predicted by the intersection of the theoretical laminar and turbulent models. Its success depends on the accuracy of these models. Xu *et. al.* [Xujg] reports that the Wilson and Thomas model produces good turbulent flow predictions and Slatter also uses it. Unlike the Newtonian Reynolds number which is based on fundamental assumptions regarding the viscous and inertial forces, the intersection approach has no mechanistic interpretation.

Slatter used the observed critical velocities and rheological constants determined for each of his tests to compute the Reynolds numbers and intersection velocities. Table 2.5 contains a summary of the Reynolds number results, which have in each case been reduced to its average, standard deviation and range. The intersection velocity obtained by the intersection method was compared on a percentage error basis with the actual observed critical velocity [Slat 95]. Remember that Slatter's primary objective was to obtain a single laminar/turbulent transition criterion for non-Newtonian slurries. For these models to be deemed successful they would have to obtain values close enough to some fixed constant. Figure 2.8 shows the theoretical models plotted against the experimental data obtained by Slatter for a kaolin clay mixture. Statistically the intersection method produced the best overall results. However for small pipe diameters, where Slatter reports the flow conditions to be primarily Newtonian, the intersection method becomes less accurate. The other models are more accurate for small pipe diameters. This can be explained as the intersection method does not take the rheology of the fluid into account. According to Slatter, each of the other models revert to the Newtonian model as the pipe diameter decreases [Slat 95]. For large pipe diameters the critical velocity becomes independent of the pipe diameter, i.e., the data approach an asymptote as depicted in Figure 2.8 [Slat 95]. Only the intersection method and R_{mr} were able to predict this. Among the Reynolds numbers, R_{mr} best predicted the transition, followed by Ryan and Johnson's [Ryan] stability criterion and the Newtonian approximation (i.e. R_{newt}). Figure 2.8 shows that the Torrance/Clapp Reynolds number (i.e. R_{torr}) performed the worst. It was unable to predict the transition.

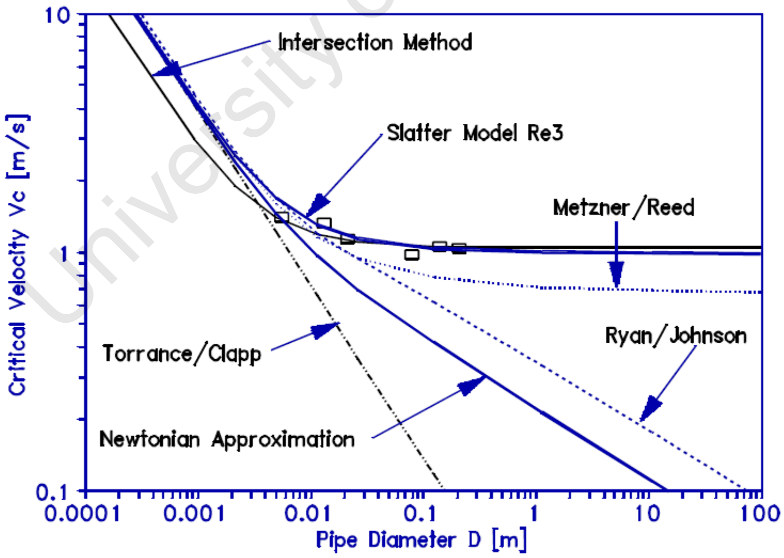

Figure 2.8: The critical velocity vs. pipe diameter for a kaolin clay slurry together with the theoretical models (source: [Slat 95], reproduced by scanning).

Slatter tested three of his own Reynolds number formulations. R_{mr} is used widely, but n' and K' need to be computed for every value of τ_w. In his first approach, Slatter aimed at simplifying Metzner and Reed's criterion. He defines, $R_1 = 16/f$, where f is the laminar Fanning friction factor. R_1 and R_{mr} yield the same results, but evaluating the former is less cumbersome.

Slatter's second formulation is derived from the fundamental assumption that the Reynolds number is proportional to the ratio between the inertial and viscous forces,

$$R \propto \frac{\text{inertial force}}{\text{viscous force}},$$

where

$$\text{inertial force} \propto \rho D^2 V^2 \qquad \text{and} \qquad \text{viscous force} \propto D^2 \tau_{\mathrm{visc}} \;\cdot$$

For a yield pseudoplastic fluid the viscous stress τ_{visc} is related to the shear rate by the following constitutive relation,

$$\tau_{\mathrm{visc}} = \tau_0 + K \left(\frac{8V}{D} \right)^n ,$$

where $(8V/D)$ is used as the representative shear rate. Combining the three equations above results in

$$R_2 \propto \frac{\rho V^2}{\tau_0 + K \left(\frac{8V}{D} \right)^n}.$$

The proportionality constant is set to a value of 8. R_2 then reduces to (2.11) under Newtonian conditions ($\tau_0 = 0$, $K = \mu$ and $n = 1$). The final form of Slatter's second Reynolds number reads

$$R_2 = \frac{8\rho V^2}{\tau_0 + K \left(\frac{8V}{D} \right)^n}.$$

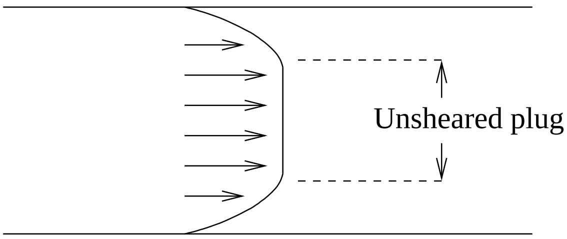

Figure 2.9: Velocity distribution across a pipe section (source: [Slat 95]).

Finally, Slatter used the concept of plug flow to derive a third Reynolds number. An unsheared core concentric with the pipe axis exists within the laminar flow of the slurries tested by Slatter (see Figures 2.9 and 2.10). The unsheared core acts as a boundary and it is well known as reported by Slatter that solid boundaries inhibit turbulence. With reference to Figure 2.10 the third formulation reads,

$$R_3 = \frac{8\rho V_{\text{ann}}^2}{\tau_0 + K\left(\frac{8V_{\text{ann}}}{D_{\text{shear}}}\right)^n},$$

where V_{ann} is the mean velocity of the annulus and $D_{\text{shear}} = 2\left(r_{\text{pipe}} - r_{\text{plug}}\right)$.

Table 2.6 shows a summary of the results for R_1, R_2 and R_3 where they too were reduced to their averages, standard deviations and ranges. Combining the results for all the Reynolds numbers investigated by Slatter including his own, we find based on its lower variance (percentage standard deviation) that R_3 out-performed all of its predecessors (see Tables 2.5 and 2.6). Figure 2.8 shows that R_3 better predicts the asymptotic relation between the critical velocity and pipe diameters than both R_{mr} and the intersection method. Slurries are two-phase mixtures of solid particles immersed in fluid. Their categorisation depends on their settling velocities. The settling velocity is the minimum fluid velocity required to keep the particles suspended in the mixture. This settling amongst others, depends or is influenced by the flow regime and concentration of the particle. The lift force within a turbulent regime normally keeps the particles a float. Homogeneous slurries, so called because the particles maintain a uniform distribution, have a low settling velocities. Their flows have been modelled using well-known non-Newtonian fluid models like the power-law, Casson and Hershel-Bulkley. Heterogeneous slurries have high settling velocities and usually maintain the rheology of the fluid.

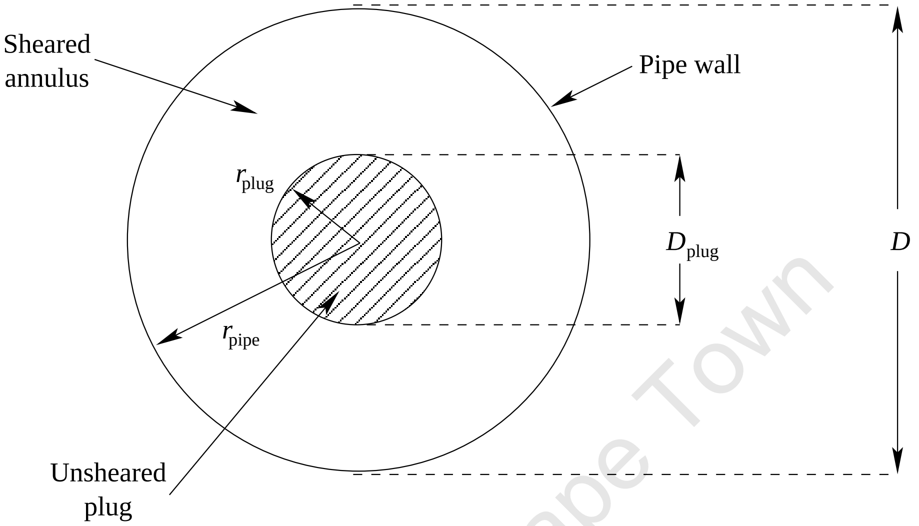

Figure 2.10: Unsheared plug geometry (source: [Slat 95]).

	R_1	R_2	R_3
Average	3268	3742	2643
Std Deviation	981	1178	658
Std Deviation %	30	31	25
Minimum	1516	1740	1310
Maximum	6451	7577	4606
Range	4935	5837	3296

Table 2.6: Slatter's Non-Newtonian Reynolds numbers - computed using the rheological parameters obtained from the least squares fits and the observed critical velocities. The results have been reduced to their averages, standard deviations and ranges (source: [Slat 95]).

Charpin *et. al.* [Char 2] investigated the minimum angle of the slope required to set boulders immersed in fluid into motion. These flows were highly turbulent, with Reynolds numbers reaching 10^6. This is well outside of the range flows of interest to us. Slatter [Slat 95] as part of his doctoral thesis tested how well three existing and three novel non-Newtonian Reynolds number formulations predicted the laminar-turbulent transition for slurries of kaolin clay, uranium tailings and gold slime tailings. The non-Newtonian parameters of his flows are way out of the weakly non-Newtonian range which would render the classical techniques employed in this dissertation inapplicable.

Chapter 3

Linear Stability Analysis

3.1 Introduction

The geometry and/or rheology of most flows are too complex for detailed hydrodynamic stability analyses. Researchers have thus been forced to only study a few classes of simple laminar flows. However these simplified scenarios obscure some general aspects of the instabilities [Draz]. We are ultimately interested in the hydrodynamic stability of free surface non-Newtonian flow down an incline. This work proceeds from the mathematical fact (which is not necessarily physically realisable), as shown below, that constant height free surface flow driven by gravity down an incline is equivalent to the flow that results from the application of a constant pressure gradient along a horizontal channel half-filled with a Newtonian fluid (see Figure 3.1). The flow of finite height and characteristic length L is driven only by applying p_1 at the intake and p_2 ($< p_1$) at the outlet. Hence $p_x = \frac{p_2 - p_1}{L}$. For this flow the incompressible Newtonian Navier-Stokes equation reduces to

$$u_{yy} = \frac{p_x}{\mu}. \tag{3.1}$$

As mentioned in the introduction, for standard incompressible Newtonian flow, the Navier-Stokes equatios are solved subject to the no-slip boundary conditions on the velocity, i.e. $u\left(0\right)=u\left(2H\right)=0$. This implies zero shear at $y=H$, i.e. $u_y\left(H\right)=0$. Integrating (3.1) and applying $u\left(0\right)=u_y\left(H\right)=0$ results in

$$u=\frac{p_x}{2\mu}y\left(y-2H\right).$$

For a flow of constant height down a slope, solely under the influence of gravity, the incompressible Newtonian Navier-Stokes equation reduces to

$$u_{yy}=-\frac{\rho g\sin\theta}{\mu},$$

and is solved subject to zero shear at the free surface $\left(u_y\left(h\right)=0\right)$ and no-slip at the bottom boundary $\left(u\left(0\right)=0\right)$. The solution reads

$$u=-\frac{\rho g\sin\theta}{2\mu}y\left(y-2h\right).$$

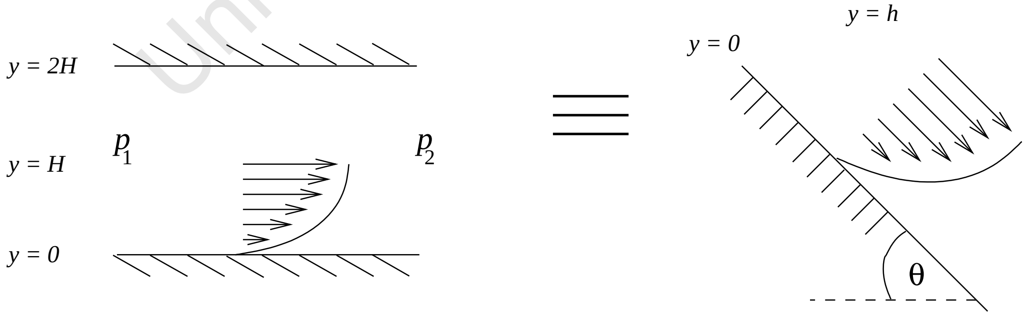

Figure 3.1: Illustration of the mathematical equivalence between pressure driven Newtonian flow (i.e. where $p_1>p_2$) and constant height gravity driven Newtonian flow down an incline of magnitude θ.

Setting $p_x=-\rho g\sin\theta$ and $h=H$ results in the same parabolic flow profiles. Newtonian gravity driven free surface flow and pressure driven horizontal flow (as described above) is therefore equivalent in the sense that their velocity profiles are identical. This motivates an attempt to extend the stability analyses from closed channel flow to open channel flow. $\theta = \frac{\pi}{2}$ is meaningless. In our investigation we are interested in flows equivalent to $\theta \ll \frac{\pi}{2}$. The growth of infinitesimal disturbances to laminar closed channel flow is described by the Orr-Sommerfeld equation. The solutions to the Orr-Sommerfeld equation depend only on the velocity profile and the boundary conditions of the flow. In the rest of this chapter we give a derivation of the Orr-Sommerfeld equation. In Chapter 4 we present a numerical investigation of the Orr-Sommerfeld equation for various profiles covering Newtonian and weakly non-Newtonian fluids and a variety of boundary conditions.

As mentioned before, hydrodynamic stability is concerned with when and how laminar flow breaks down, its subsequent development and its eventual transition to turbulence [Draz]. But unlike Reynolds we conduct theoretical experiments, like many others (see the annual review [Eckh]) subjecting known laminar flow solutions of the Navier-Stokes equations to infinitesimal disturbances. If the disturbed flow returns to its original laminar state the flow is termed as stable, but if the perturbation grows and never dies out the flow is termed as unstable [Draz, Schm, Coll]. Assuming that the disturbance is infinitesimal allows one to linearise the resulting equations. But as soon as disturbance velocities grow a few percent above the base laminar flow the linearised equations are unable to adequately predict the development of the disturbance. Despite their limitations the linear equations are important in detecting physical growth mechanisms and identifying dominant disturbances [Schm].

Linear stability theory and energy stability theory [Duto] form two well-known methods for obtaining critical values that separate different types of flow, for example laminar from turbulent. But unlike linear stability theory where it is assumed that the perturbations are small, energy stability theory places no restrictions on the size of the disturbance.

In this theory an equation describing the evolution of the energy of the disturbance is derived. Incidentally Reynolds was the first to derive such an equation in 1895. Schmid and Henningson [Schm] state that in most instances the kinetic energy of the disturbance contained in a volume V,

$$E_V = \frac{1}{2}\int_V |\overline{u}|^2 \, dV \tag{3.2}$$

constitutes a natural choice for the size of a disturbance where $\overline{u}$ is the velocity vector of the disturbance. Following Joseph [Jose], Schmid and Henningson use the magnitude of the disturbance (i.e. E_V as defined in (3.2)) to provide formal definitions of stability:

1. **Stability -** A solution to the Navier-Stokes equations is *stable* to perturbations if the perturbation energy satisfies

   $$\lim_{t\to\infty} \frac{E_V(t)}{E_V(0)} \to 0.$$

2. **Conditional Stability -** If there exists a threshold energy $\delta > 0$ such that the solution is stable when $E_V(0) < \delta$, then the solution is said to be *conditionally stable.*

3. **Global Stability -** If the threshold energy is infinite, i.e. $\delta \to \infty$, the solution is said to be *globally stable.*

4. **Monotonic Stability -** If

   $$\frac{dE_V(t)}{dt} < 0, \quad \forall t > 0$$

   then the solution is said to be *monotonically stable.*

In Reynolds' initial experiments he discovered that beyond a certain critical Reynolds number, pipe flow became turbulent. Like Schmid and Henningson [Schm] we take a

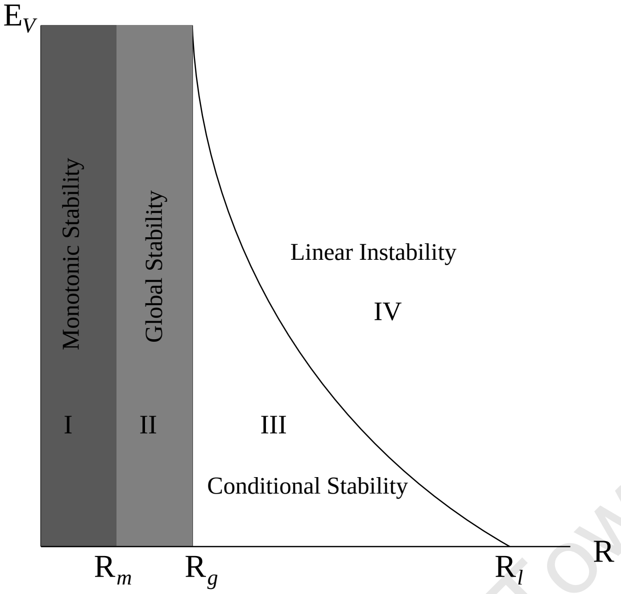

Figure 3.2: Illustrates the three critical Reynolds numbers, R_m, R_g and R_l that define the regions in which initial perturbations are monotonically, globally and conditionally stable respectively (source: [Schm]).

closer look at the above definitions to unearth which of them correspond to the stability/instability sought by our analysis. Hydrodynamic stability in its most general sense is defined as the asymptotic limit of the ratio between the energy of the perturbation, $E_V(t)$ and its initial energy, $E_V(0)$. A solution is conditionally stable if the initial energy of the perturbation, $E_V(0)$ is below a given energy threshold, δ. Conditional stability is a special case of the more general global stability, where there is no limit placed on the initial size of the perturbation. Hence a solution that is globally stable is also conditionally stable but the reverse does not necessarily apply. Monotonic stability is the most rigid criterion, requiring that the perturbation decays for all time. We introduce three critical Reynolds numbers R_m, R_g and R_l, below which initial perturbations are possibly monotonically, globally or conditionally stable respectively. Figure 3.2 depicts the regions where solutions to the Navier-Stokes equations are defined as above. In Region I where $R < R_m$, all perturbations decay monotonically with time (i.e. for all time) and solutions to the Navier-Stokes are hence referred to as monotonically stable. R_m can be derived analytically from the Reynolds-Orr equation which describes the evolution of the kinetic energy of a disturbance [Schm]. If $R_m < R < R_g$ (i.e Region II) perturbations may grow, but ultimately decay as time evolves. R_g is difficult to derive analytically but may be determined by bifurcation analysis [Schm]. Recall that solutions are conditionally stable (Region III, $R_g < R < R_l$) if disturbances of a given size (i.e. with an initial energy less than some bound, $E_V(0) < \delta$) decay with time. Conditional stability is sought when conducting the linear hydrodynamic stability analysis where infinitesimal disturbances are expected to decay. For $R > R_l$ (Region IV) perturbations grow with time and fluid flows are said to be linearly unstable or alternatively not conditionally stable. In this region at least one infinitesimal disturbance is unstable.

3.2 Deriving the Orr-Sommerfeld Equation

The Orr-Sommerfeld equation describes the growth of disturbances to the laminar solutions of the Newtonian incompressible Navier-Stokes equation for closed channel flow. Its solution involves Squire's theorem. Squire's theorem states that to obtain a minimum critical Reynolds number it is sufficient to consider only two-dimensional disturbances to the laminar flow [Coll, Draz]. In the derivation that follows we restrict ourselves to the two-dimensional co-ordinate system depicted in Figure 3.3. Once we've introduced the necessary mathematics a full reading of Squire's theorem is presented, which should justify the use of this simplified system. The restriction also allows us to conveniently express the governing equations in terms of a stream function.

The incompressible Navier-Stokes equations in two dimensions read

$$\rho \frac{\partial \overline{u}}{\partial t} = -\rho \left(\overline{u} \cdot \nabla \right) \overline{u} - \nabla p + \nabla \cdot \left(\mu \nabla \overline{u} \right) \tag{3.3}$$

$$\nabla \cdot \overline{u} = 0, \tag{3.4}$$

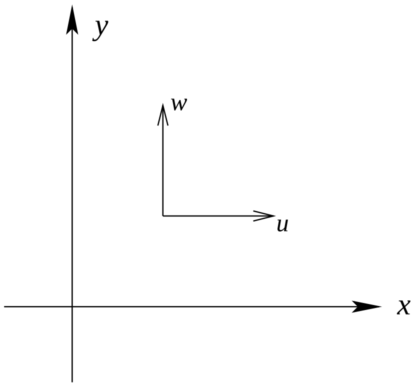

Figure 3.3: Two dimensional co-ordinate system that we employ throughout.

where ρ is the fluid density, $\overline{u} = (u\,(x,y,t)\,, w\,(x,y,t))$ and $\nabla = \left(\frac{\partial}{\partial x}, \frac{\partial}{\partial y}\right)$. If we introduce the following dimensionless quantities,

$$\tilde{\overline{u}} = \frac{\overline{u}}{V}, \quad \tilde{p} = \frac{p}{\rho V^2}, \quad \tilde{t} = \frac{tV}{L}, \quad \tilde{x} = \frac{x}{L}, \quad \tilde{y} = \frac{y}{L}$$

and drop the tildes, then for constant viscosity Newtonian flow (3.3) yields

$$\frac{\partial \overline{u}}{\partial t} = -\left(\overline{u} \cdot \nabla\right) \overline{u} - \nabla p + \frac{1}{R} \nabla \cdot \left(\nabla \overline{u}\right), \tag{3.5}$$

where $R \equiv \rho V L / \mu$ is the Reynolds number. V is a characteristic velocity and L is a characteristic length. Define the stream function ψ by

$$\begin{aligned} u &= \frac{\partial \psi}{\partial y}, \\ w &= -\frac{\partial \psi}{\partial x}. \end{aligned}$$

We substitute these expressions for u and w into the Navier-Stokes equation (3.5) and differentiate its x-component with respect to y and its y-component with respect to x to reach

$$\begin{aligned}&\frac{\partial^3\psi}{\partial y\partial t\partial y}+\frac{\partial^2\psi}{\partial y^2}\frac{\partial^2\psi}{\partial x\partial y}+\frac{\partial\psi}{\partial y}\frac{\partial^3\psi}{\partial y\partial x\partial y}-\frac{\partial^2\psi}{\partial y\partial x}\frac{\partial^2\psi}{\partial y^2}-\frac{\partial\psi}{\partial x}\frac{\partial^3\psi}{\partial y^3}\\&+\frac{\partial^2 p}{\partial y\partial x}-\frac{1}{R}\left(\frac{\partial^4\psi}{\partial y\partial x^2\partial y}+\frac{\partial^4\psi}{\partial y^4}\right)=0\end{aligned}\tag{3.6}$$

and

$$\begin{aligned}&-\frac{\partial^3\psi}{\partial x\partial t\partial x}-\frac{\partial^2\psi}{\partial x\partial y}\frac{\partial^2\psi}{\partial^2 x}-\frac{\partial\psi}{\partial y}\frac{\partial^3\psi}{\partial^3 x}+\frac{\partial^2\psi}{\partial x^2}\frac{\partial^2\psi}{\partial y\partial x}+\frac{\partial\psi}{\partial x}\frac{\partial^3\psi}{\partial x\partial y\partial x}\\&+\frac{\partial^2 p}{\partial x\partial y}+\frac{1}{R}\left(\frac{\partial^4\psi}{\partial x^4}+\frac{\partial^4\psi}{\partial x\partial y^2\partial x}\right)=0.\end{aligned}\tag{3.7}$$

(3.7) is then subtracted from (3.6) and (assuming continuity of the derivatives) we are left with an equation that is without the pressure term

$$\frac{\partial}{\partial t}\triangle\psi+\frac{\partial\psi}{\partial y}\frac{\partial}{\partial x}\triangle\psi-\frac{\partial\psi}{\partial x}\frac{\partial}{\partial y}\triangle\psi-\frac{1}{R}\triangle^2\psi=0,$$

where $\triangle=\left(\frac{\partial^2}{\partial x^2}+\frac{\partial^2}{\partial y^2}\right)$. We let $\psi=\psi_0(y)+\widehat{\psi}(x,y,t)$, where $\psi_0=\int U(y)\,dy$, $U(y)$ is the steady-state laminar flow slow solution to (3.5) and $\widehat{\psi}$ is a perturbation of the stream function. Then

$$\frac{\partial}{\partial t}\triangle\widehat{\psi}+\left(U+\frac{\partial\widehat{\psi}}{\partial y}\right)\frac{\partial}{\partial x}\triangle\widehat{\psi}-\frac{\partial\widehat{\psi}}{\partial x}\left(U_{yy}+\frac{\partial}{\partial y}\triangle\widehat{\psi}\right)=\frac{1}{R}\triangle^2\widehat{\psi}.\tag{3.8}$$

Since we assumed that the disturbance was small we are able to ignore higher order terms. The linearised version of equation (3.8) reads

$$\frac{\partial}{\partial t}\triangle\widehat{\psi}+U\frac{\partial}{\partial x}\triangle\widehat{\psi}-U_{yy}\frac{\partial\widehat{\psi}}{\partial x}=\frac{1}{R}\triangle^2\widehat{\psi}.$$

The perturbation that we impose on the laminar solution has the form of a traveling wave

$$\widehat{\psi} = \phi(y) \exp\left[i(\alpha x + ct)\right], \tag{3.9}$$

where $\phi(y)$ is the complex amplitude, α the real wavenumber and c is the complex wave speed. Substituting this wave expression for the disturbance results in the famous Orr-Sommerfeld (OS) equation

$$\lambda\left(\phi_{yy} - \alpha^2\phi\right) + i\alpha U\left(\phi_{yy} - \alpha^2\phi\right) - i\alpha\phi U_{yy} = \frac{1}{R}\left(\phi_{yyyy} - 2\alpha^2\phi_{yy} + \alpha^4\phi\right), \tag{3.10}$$

where $\lambda = ic$, attributed to William Orr and Arnold Sommerfeld [Coll]. Within this theory when $\Im(c) < 0$ and hence $\Re(\lambda) > 0$, the disturbance grows with time, indicating the onset of turbulence. $\Im(c)$ and $\Re(\lambda)$ denote the imaginary and real parts of c and λ respectively. Therefore, given any $\alpha > 0$ and $R > 0$ we are left with solving the Orr-Sommerfeld equation (3.10) for the eigenvalues λ. The critical Reynolds number, which we denote as R_{crit}, is that number beyond which at least one disturbance is unstable (i.e. for R_{crit} there exists at least one $\Re(\lambda) > 0$). Equation (3.9) defines only some of the possible perturbations, i.e. those which assume the form of a traveling wave. Coussot also reminds us that the linear stability analysis results only in a sufficient condition. Hence there may be disturbances which lead to instabilities whose $\Re(\lambda) < 0$ [Cous]. As promised we now present a full reading of Squire's theorem. Here we consider three-dimensional flow in a channel of infinite length and breadth. For the thee-dimensional disturbances the corresponding perturbation (3.9) would read

$$\widehat{\psi} = \phi(y) \exp\left[i(ax + bz + ct)\right],$$

where a and b are the real wavenumbers and c the complex wave speed. Squire's theorem as given in [Coll] states

- **Squire's Theorem.** If $R_L = R\left(a, b\right)$ is the critical Reynolds number given a and b then

$$\min_{a,b} R_L\left(a, b\right) = \min_{a} R_L\left(a, 0\right).$$

As explained the OS equation describes the growth of disturbances to the laminar solutions of the Newtonian Navier-Stokes equation. These laminar solutions are denoted as U in (3.10). We now derive these U for the flows which we'll be investigating along with the relevant boundary conditions.

3.2.1 Closed channel uniform flow approximations

First we investigate the stability of parallel shear flows between two planes of infinite length, which we refer to as closed channel flows (see Figures 1.1 and 1.2). This simplifying assumption, where the planes are assumed to be of infinite length, allows us to ignore the influences of the respective entry and exit conditions. As noted earlier, the equation of motion is

$$\mu\frac{d^2u}{dy^2} = \frac{dp}{dx} \tag{3.11}$$

and here it is solved subject to the no-slip boundary conditions, where it is assumed that the layers of fluid adjacent to the boundaries stick to them, i.e. $u(\pm1) = 0$ for Poiseuille flow and $u(1) = 1$ and $u(-1) = -1$ for Couette flow [Hugh, Wilc]. The plane Poiseuille profile reads

$$U(y) = 1 - y^2.$$

One way in which to achieve plane Couette flow is by shearing the planes in opposite directions at constant velocities whilst maintaining constant pressure across the channel, i.e. $\frac{dp}{dx} = 0$. Its laminar flow profile reads

$$U(y) = y.$$

3.2.2 Closed channel boundary conditions

For closed channel flows the Navier-Stokes equation (3.3) and consequently the OS equation (3.10) is solved subject to the no-slip boundary conditions (see Section 3.2.1) and $w(\pm 1) = 0$. The stream function representations of the boundary conditions for plane Poiseuille flow translate as

$$\begin{aligned} \text{For } y = \pm 1: \quad u = 0 \quad &\Longrightarrow \frac{\partial}{\partial y}\left[\psi_0 + \widehat{\psi}\right] = U + \phi_y \exp\left[i\left(\alpha x + ct\right)\right] = 0 \\ &\Longrightarrow \phi_y\left(\pm 1\right) = 0, \end{aligned}$$

and

$$\begin{aligned} \text{For } y = \pm 1: \quad w = 0 \quad &\Longrightarrow \frac{\partial}{\partial x}\left[\psi_0 + \widehat{\psi}\right] = i\alpha\phi\left(y\right) \exp\left[i\left(\alpha x + ct\right)\right] = 0 \\ &\Longrightarrow \phi\left(\pm 1\right) = 0. \end{aligned}$$

Similarly it can be shown that for plane Couette flow, the OS equation should be solved subject to $\phi_y(\pm 1) = 0$ and $\phi(\pm 1) = 0$.

3.2.3 Open channel flows and their boundary conditions

We showed in Section 3.1 that the open channel Newtonian steady-state flow profile is parabolic in y. It is in fact half the plane Poiseuille profile, restricting its domain to $[-1; 0]$, i.e. $U(y) = 1 - y^2$ for $y \in [-1; 0]$. In this sense, open channel Newtonian flow is equivalent to a combined Couette-Poiseuille flow. Since the numerical technique that we employ is defined for $y \in [-1;1]$ and to keep the domains in which we are working consistent (i.e. $[-1;1]$]), we scale the parabolic plane Poiseuille profile such that $U(1) = 1$ and $U(-1) = 0$ (see Figure 3.4). The resulting expression for the open channel profile reads,

$$U\left(y\right) = -\frac{y^2}{4} + \frac{y}{2} + \frac{3}{4}.$$

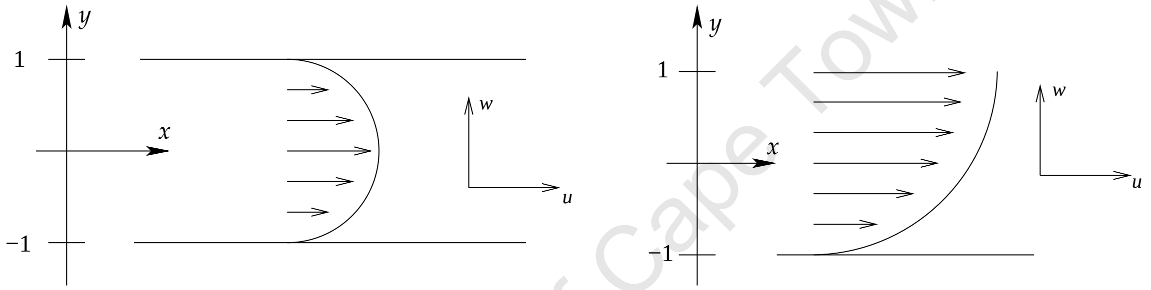

Figure 3.4: Plane Poiseuille and open channel flow profiles, i.e. $U\left(y\right) = 1 - y^2$ and $U\left(y\right) = -\frac{y^2}{4} + \frac{y}{2} + \frac{3}{4}$ respectively.

As for closed channel flows the OS equation is solved subject to the no-slip boundary condition, where the velocity of the fluid relative to the wall is zero, i.e. $u\left(-1\right) = 0$, and $w\left(\pm 1\right) = 0$. A free surface is one where nothing touches it — we regard the shear of air on a liquid as negligible, employing the zero shear boundary condition at this interface, i.e. $u_y\left(1\right) = 0$ [Hugh]. This is consistent with the derivation in Section 3.1. For $y = -1$ the boundary conditions translate as for closed channel flows, namely

$$u = w = 0 \Longrightarrow \phi_y\left(-1\right) = \phi\left(-1\right) = 0.$$

For $y = 1$:

$$\begin{aligned} u_y = 0 \quad &\Longrightarrow \frac{\partial^2}{\partial y^2}\left[\psi_0 + \widehat{\psi}\right] = U_y\left(1\right) + \phi_{yy}\exp\left[i\left(\alpha x + ct\right)\right] = 0 \\ &\Longrightarrow \phi_{yy} = 0 \end{aligned}$$

and again as for closed channel flows

$$\begin{aligned} &w = 0 \\ &\Longrightarrow \phi\left(1\right) = 0. \end{aligned}$$

Hence for Newtonian open channel flow the OS equation is solved subject to $\phi\left(\pm 1\right) = \phi_y\left(-1\right) = \phi_{yy}\left(1\right) = 0$.

3.3 Marginal Stability Curve

For the purpose of explaining Figure 3.5 we digress briefly on an equivalent form of the OS equation. Acheson uses $\widehat{\psi} = \phi\left(y\right)\exp\left[i\left(kx - \omega t\right)\right]$ as his definition of the perturbation (3.9) [Ache]. With reference to equation (3.10), this is equivalent to having $k = \alpha$ and $\omega = -c$. Laminar flows thus become turbulent when $\Im\left(\omega\right) > 0$, whereas a disturbance as we have it defined becomes unstable when $\Im\left(c\right) < 0$. Depicted in Figure 3.5 is a marginal stability curve for Poiseuille flow, which represents the unstable disturbances as a function of the Reynolds and wave- numbers. Given any R, for each k in the shaded region at least one disturbance in unstable, i.e. for that R and k there exists at least one ω with a negative imaginary part. The critical Reynolds number, R_{crit} is the least R for which there exists an unstable disturbance. For plane Poiseuille flow this is reported to be around 5772.2 [Ache, Chap, Draz, Schm, Tref 01]. This unstable disturbance is called a Tollmien-Schlitchting wave and its wavenumber is close to 1.02 [Schm, Draz]. Tollmien and Schlitchting first discovered that the OS equation has unstable disturbances for flows without inflection points (i.e. laminar flow profiles without inflection points) [Schm].

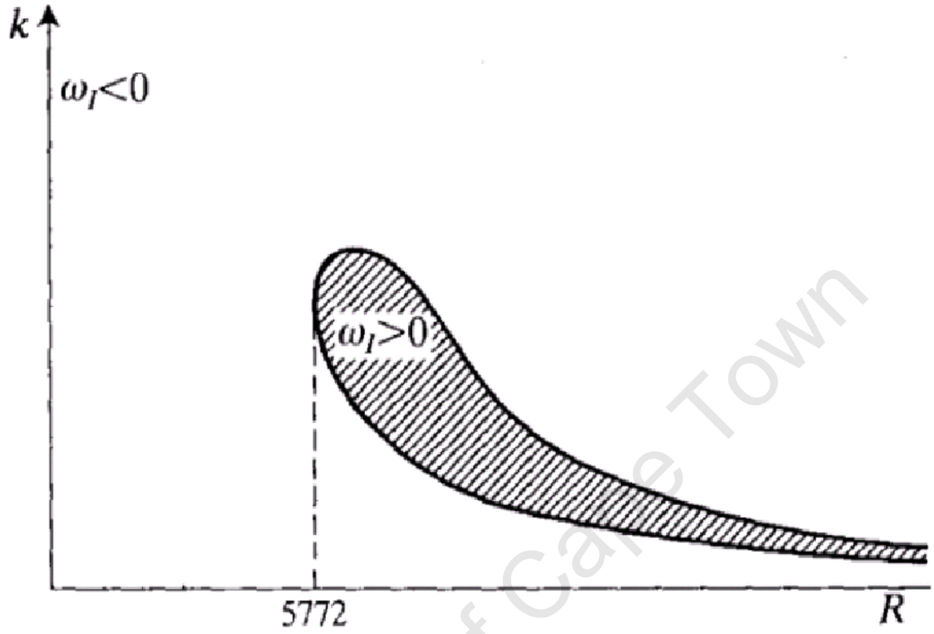

Figure 3.5: Marginal stability curve for plane Poiseuille flow where disturbances become unstable when the the $\Im(\omega) > 0$ (source: [Ache], reproduced by scanning).

Until now we have assumed that the viscosity is constant. The OS equation which is derived on this assumption therefore only applies to Newtonian fluids and GNF's where the visosity is constant. However, we are also interested in situations where the fluid is non-Newtonian. The rheological models used to describe non-Newtonian flow contain constants that indicate their non-Newtonian character, i.e. 'non-Newtonianess' (see Sections 1.3 and 2.4). For example with power-law flow the larger $|n-1|$, the larger the variation in the viscosity with the shear rate. In the following chapter we do not derive a non-Newtonian analogue of the OS equation but we do investigate the stability of weakly non-Newtonian fluids. By weakly we mean that the viscosity is close to constant and assume that the OS equation holds, e.g. power-law fluids with n near 1. We do this using both the power-law and Ellis models. However with the Ellis model it's not the simple case of a single parameter determining the non-Newtonian nature of the flow. The Ellis model predicts that a non-Newtonian fluid behaves like a Newtonian fluid, either at very low shear rates or for $\gamma \ll 1$. For the Ellis model weakly non-Newtonian could therefore imply investigating the stability using (3.10) for flows just outside of this Newtonian shear rate range.

The boundary conditions derived for closed and open channel Newtonian flow are also used for weakly non-Newtonian fluids (see Sections 3.2.2 and 3.2.3 respectively). Our first objective in the following chapter is to replicate the marginal stability curve for plane Poiseuille flow depicted in Figure 3.5. Thereafter we seek to determine a critical Reynolds number for Newtonian open channel flow and investigate the stability of weakly non-Newtonian fluids employing both the power-law and Ellis models.

Chapter 4

Solutions to the Orr-Sommerfeld Equation

We develop a solution for the Newtonian OS equation using plane Poiseuille flow as an example. Thereafter we extend the numerical scheme to more complex flows. Written as a differential eigenvalue problem we approximate the second and fourth order derivative operators of the OS equation using the pseudospectral method employed by Trefethen [Tref 01].

4.1 Pseudospectral Method for Solving the OS Equation

Spectral methods, an alternative to finite difference and finite element methods [Huan], use series of known smooth functions to approximate solutions to differential equations and differential eigenvalue problems [Gott 77]. Trefethen [Tref 01] uses polynomials of degree N, that pass through the Chebyshev-Lobatto points,

$$x_j = \cos\left(\frac{j\pi}{N}\right), \quad j = 0, 1, 2, ..., N, \tag{4.1}$$

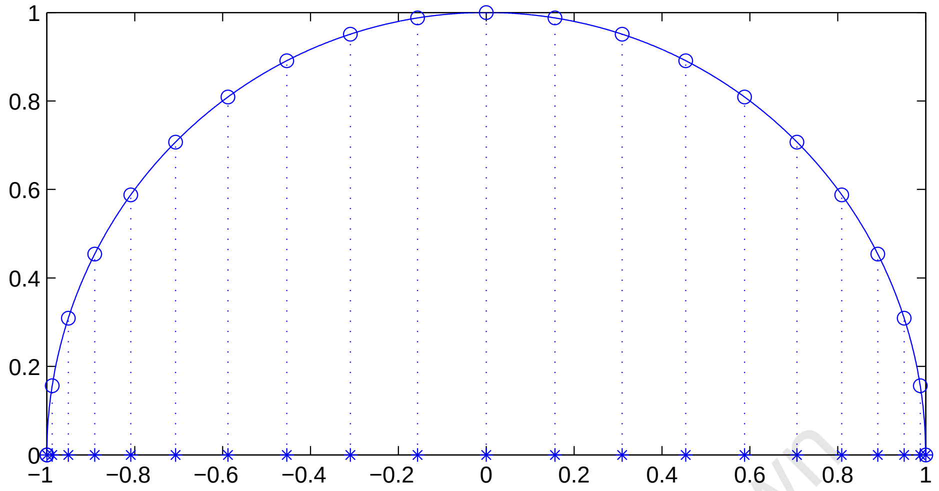

Figure 4.1: The Chebyshev-Lobatto points (4.1) form the x values of equally spaced points on the unit circle, which cluster near the end points. Here we have $N = 20$.

to construct interpolants for the derivatives of the OS equation. The Chebyshev-Lobatto points cluster near the end points of the $[-1;1]$-interval over which they are distributed and form the extrema of N^{th} order Chebyshev polynomial. Figure 4.1 shows that they are the x values of equally spaced points on the unit circle. Polynomial interpolants based on equally spaced discretisations are poor at approximating smooth functions. As the number of collocation points increases, the interpolating polynomial may fail to converge and the approximation may get worse at a rate as great as 2^N where N is the number of intervals in the grid [Gott 84, Tref 01]. The spectral derivative obtained by differentiating such an interpolant would be in error by a similar factor [Tref 01]. The pseudospectral approximation of the derivative of some function $f(x)$ is achieved in two steps. (1) The N^{th} degree polynomial interpolant, $l(x)$ of $f(x)$ is given by the Lagrange form of the interpolating polynomial,

$$l(x) = \sum_j \left(\prod_{k \neq j} \frac{x - x_j}{x_j - x_k} \right) v_j, \tag{4.2}$$

where $v_j = f(x_j)$. (2) The discrete derivatives, $w_j = l'(x_j) \approx f'(x_j)$ are obtained by differentiating $l(x)$ and expressing it in terms of v_j [Gott 84]. v_j are scalar and since differentiation is a linear operation w_j, the approximate derivatives at the Chebyshev-Lobatto points, can be obtained with a single matrix operation. That is, by multiplying $f(x_j)$ by an $(N+1) \times (N+1)$ matrix, which Trefethen denotes as D_N, i.e.

$$w = D_N \times v.$$

These N degree polynomial interpolants are equivalent to a linear combination of N Chebyshev polynomials. Hence when referring to the number of polynomials in this work we mean the number of Chebyshev polynomials used to construct the interpolant. We illustrate, by way of example, how these differentiation matrices are constructed. For $N = 3$ (i.e. $j = 0, 1, 2, 3$) the collocation points are $x_0 = 1$, $x_1 = 0.5$, $x_2 = -0.5$, and $x_3 = -1$, and the Lagrange interpolant reads

$$\begin{aligned} l(x) &= \frac{2}{3}\left(x^3 + x^2 - \frac{x}{4} - \frac{1}{4}\right) v_0 - \frac{4}{3}\left(x^3 + \frac{1}{4}x^2 - x - \frac{1}{4}\right) v_1 \\ &\quad + \frac{4}{3}\left(x^3 - \frac{1}{4}x^2 - x + \frac{1}{4}\right) v_2 - \frac{2}{3}\left(x^3 - x^2 - \frac{x}{4} + \frac{1}{4}\right) v_3. \end{aligned} \tag{4.3}$$

Differentiating $l(x)$ and evaluating the resulting function, $l'(x)$ at the x_j for $N = 3$ we obtain

$$\begin{pmatrix} w_0 \\ w_1 \\ w_2 \\ w_3 \end{pmatrix} = D_3 \begin{pmatrix} v_0 \\ v_1 \\ v_2 \\ v_3 \end{pmatrix},$$

where

$$D_3 = \begin{pmatrix} \frac{19}{6} & -4 & \frac{4}{3} & -\frac{1}{2} \\ 1 & -\frac{1}{3} & -1 & \frac{1}{3} \\ -\frac{1}{3} & 1 & \frac{1}{3} & 1 \\ \frac{1}{2} & -\frac{4}{3} & 4 & -\frac{19}{6} \end{pmatrix}.$$

For an arbitrary positive integer N, general formulae for the entries of these differentiation matrices, D_N may be derived as described by Trefethen [Tref 01]. The Lagrange interpolants of degree N used to compute the column entries of D_N can be written as

$$l_j(x) = \frac{1}{a_j} \prod_{\substack{k=0 \\ k \neq j}}^{N} (x - x_k), \tag{4.4}$$

where all the $x_0, x_1, x_2, ..., x_N$ are distinct real numbers and

$$a_j = \prod_{\substack{k=0 \\ k \neq j}}^{N} (x_j - x_k).$$

For $N = 3$, $l_j(x)$ are the polynomial coefficients of the v_j terms in equation (4.3), i.e. the bracketed expressions in (4.3). We take the logarithm of equation (4.4),

$$\begin{aligned} \ln(l_j(x)) &= \ln\left(\frac{1}{a_j} \prod_{\substack{k=0 \\ k \neq j}}^{N} (x - x_k)\right) \\ &= \sum_{\substack{k=0 \\ k \neq j}}^{N} \ln(x - x_k) - \ln(a_j), \end{aligned} \tag{4.5}$$

then differentiate (4.5) to obtain

$$l'_j(x) = l_j(x) \sum_{\substack{k=0 \\ k \neq j}}^{N} (x - x_k)^{-1}.$$

We evaluate $l_j'(x)$ at the collocation points to derive the formulae that constitute the entries of Chebyshev differentiation matrices, D_N. The diagonal entries read as follows, for $i = j$,

$$\begin{aligned} (D_N)_{ii} \quad &= \frac{1}{a_i} \prod_{\substack{k=0 \\ k \neq i}}^{N} (x_i - x_k) \sum_{\substack{k=0 \\ k \neq i}}^{N} (x_i - x_k)^{-1} \\ &= \sum_{\substack{k=0 \\ k \neq i}}^{N} (x_i - x_k)^{-1} . \end{aligned}$$

For $i \neq j$,

$$\begin{aligned} (D_N)_{ij} \quad &= \frac{1}{a_j} \frac{(x_i - x_1)(x_i - x_2) \ldots (x_i - x_i) \ldots (x_i - x_N)}{(x_i - x_j)} \times \left(\frac{1}{x_i - x_0} + \frac{1}{x_i - x_1} + \ldots \right. \\ &\left. + \frac{1}{x_i - x_i} + \ldots + \frac{1}{x_i - x_N} - \frac{1}{x_i - x_j} \right) = \frac{1}{a_j} \prod_{\substack{k=0 \\ k \neq i,j}}^{N} (x_i - x_k) = \frac{a_i}{a_j (x_i - x_j)} \end{aligned}$$

But since the collocation points, x_j are the Chebyshev-Lobatto points, where $x_j = -x_{N-j}$ for $j = 0, 1, ..., H$ ($H = \frac{N}{2}$, if N is even and $H = \frac{N+1}{2}$, if odd), Gottlieb *et. al.* [Gott 84] reduces the formulae for D_N to the following,

$$\begin{aligned} (D_N)_{00} = \frac{2N^2+1}{6}, \quad (D_N)_{NN} = -\frac{2N^2+1}{6} \\ (D_N)_{jj} = \frac{-x_j}{2\left(1 - x_j^2\right)}, \quad j = 1, \ldots, N-1 \\ (D_N)_{ij} = \frac{c_i}{c_j} \frac{(-1)^{i+j}}{(x_i - x_j)}, \quad i \neq j, \ i, j = 1, \ldots, N-1, \end{aligned}$$

where

$$c_i = \begin{cases} 2 & i = 0 \, \text{or} \, N, \\ 1 & \text{otherwise}. \end{cases}$$

We have illustrated that to approximate numerically the derivative of some function, $f(x)$ we simply apply D_N to a vector of samples of $f(x)$. This results in approximations of the derivative, $f'(x_j)$ at the Chebyshev-Lobatto collocation points. Consequently its n^{th} derivative can be obtained by the matrix multiplication of the n^{th} power of D_N with $f(x)$, i.e. $f^n(x) \approx D_N^n f(x)$, where $f(x)$ denotes the vector of function values at the x_j. The above algorithm for D_N is coded as cheb.m in [Tref 01] (see appendix A).

4.2 Newtonian Closed Channel Flow

4.2.1 Plane Poiseuille flow

Writing the OS equation as a differential eigenvalue problem

$$\left[\frac{1}{R}\left(\mathrm{D}^4 - 2\alpha^2\mathrm{D}^2 + \alpha^4\right) - i\alpha U\left(\mathrm{D}^2 - \alpha^2\right) + i\alpha U_{yy}\right]\phi = \lambda\left(\mathrm{D}^2 - \alpha^2\right)\phi, \tag{4.6}$$

where D^2 and D^4 are the second and fourth order derivative operators respectively for $-1 \leq y \leq 1$, we are left with having to solve for its eigenvalues, λ. λ describes the growth of the disturbance with time. If, for a given R and some α, the real part of λ is positive (i.e. $\Re(\lambda) > 0$) then that flow is unstable. The least R for which this is the case indicates the onset of turbulence as predicted by the linear stability theory. This is defined as the critical Reynolds number, R_{crit}. We now focus on a particular flow, solving (4.6) for a specific U with the corresponding boundary conditions on ϕ. For plane Poiseuille the discrete OS eigenvalue problem reads

$$A\overrightarrow{v} = \lambda B\overrightarrow{v}, \tag{4.7}$$

where

$$\begin{aligned} A \quad &= \frac{1}{R}\left(\widetilde{\mathrm{D}^4} - 2\alpha^2\widetilde{\mathrm{D}^2} + \alpha^4 I\right) - i\alpha\mathrm{diag}\left(1 - y_j^2\right)\left(\widetilde{\mathrm{D}^2} - \alpha^2 I\right) - 2i\alpha I \\ B \quad &= \widetilde{\mathrm{D}^2} - \alpha^2 I. \end{aligned}$$

I is the $(N-1)\times(N-1)$ identity matrix, diag $\left(1 - y_j^2\right)$ a diagonal matrix, $v_j = \phi\left(y_j\right)$ and y_j the Chebyshev-Lobatto points for $j = 1, 2, 3, ..., N-1$. $\widetilde{\mathrm{D}^2}$ and $\widetilde{\mathrm{D}^4}$ are the second and fourth derivative operator approximates respectively. When implementing the boundary conditions on the polynomial interpolants for this pseudospectral method, one may either add equations that enforce the conditions or restrict oneself to interpolants that satisfy the conditions. It is the second of these approaches that we employ.

Trefethen [Tref 01] imposes homogeneous Dirichlet boundary conditions, i.e., $\phi(\pm 1) = 0$ as follows. He takes the interior Chebyshev points $y_1, ..., y_{N-1}$ (defined by (4.1)) as his computational grid with $[v_1, ..., v_{N-1}]^T$ as the corresponding vector of unknowns. Spectral differentiation is performed by letting $p(y)$ be the unique polynomial interpolant of degree $\leq N$ with $p(\pm 1) = 0$ and $p(y_j) = v_j$, $1 \leq j \leq N-1$. A second derivative approximate, w_j is consequently obtained by differentiating p twice, i.e. $w_j = p''(y_j)$, $1 \leq j \leq N-1$. Now the square of the Chebyshev differentiation matrix, D_N^2 maps a vector $[v_0, ..., v_N]^T$ to a vector $[w_0, ..., w_N]^T$. The procedure of implementing the homogeneous Dirichlet boundary conditions as described amounts to fixing v_0 and v_N at zero, and ignoring w_0 and w_N. This implies that the first and last columns of D_N^2 have no effect since they are multiplied by zero, and the first and last rows have no effect since they are ignored. $\widetilde{\mathrm{D}^2}$ is thus constructed by squaring D_N and removing its first and last rows and columns.

When approximating the fourth order derivative operator each of the four boundary conditions are enforced. Two of these conditions have to be imposed on the first derivative of the interpolating polynomial, which adds to the complexity. This is achieved as follows.

We set the interpolant

$$u\left(y\right)=\left(1-y^{2}\right)q\left(y\right),$$

where $q\left(y\right)$ is a polynomial of degree $\leq N$ with $q\left(\pm1\right)=0$. $u\left(y\right)$ thus corresponds to a polynomial of degree $\leq N+2$ with $u\left(\pm1\right)=u_{y}\left(\pm1\right)=0$. We differentiate $u\left(y\right)$ four times to obtain

$$u_{yyyy}\left(y\right)=\left(1-y^{2}\right)q_{yyyy}\left(y\right)-8yq_{yyy}\left(y\right)-12q_{yy}\left(y\right),$$

but since $q\left(y_{j}\right)=\frac{u\left(y_{j}\right)}{\left(1-y_{j}^{2}\right)}$, the fourth order derivative operator approximate reads

$$\widetilde{\mathrm{D}^{4}}=\left[\operatorname{diag}\left(1-y_{j}^{2}\right)D_{N}^{4}-8\operatorname{diag}\left(y_{j}\right)D_{N}^{3}-12D_{N}^{2}\right]\times\operatorname{diag}\left(1/\left(1-y_{j}^{2}\right)\right),$$

where D_{N}^{2}, D_{N}^{3} and D_{N}^{4} have their first and last rows and columns removed as before. The OS operators are coded as orrsom.m in Appendix B [Tref 01].

Marginal stability diagrams, like the one depicted in Figure 4.2, indicate for which R there exist perturbations that grow with time. These perturbations (3.9) have negative imaginary wave speeds, i.e., $\Im\left(c\right)<0\Longrightarrow\Re\left(\lambda\right)>0$. Given R and α we compute the eigenvalues, λ, of the discrete eigenvalue problem (4.7). The R and α corresponding to λ with positive real parts lie within the curve shown in Figure 4.2. We used version 2.1.73 of the Octave numerical package to compute our results [Octa]. Since it does not have a generalised eigenvalue solver we reduce the problem to a standard problem, computing the eigenvalues for $B^{-1}A$ instead. The resulting marginal stability curve, Figure 4.2, was produced using a polynomial interpolant of degree ≤ 202 (i.e. $N+2=202$ or it could be said the interpolant was constructed using $N=200$ Chebyshev polynomials). Trefethen [Tref 01] reports that the most sensitive perturbation has a dependence on y close to $\exp\left(1.02iy\right)$ (see also the Tollmien-Schlitchting wave in Section 3.3.). Our computations

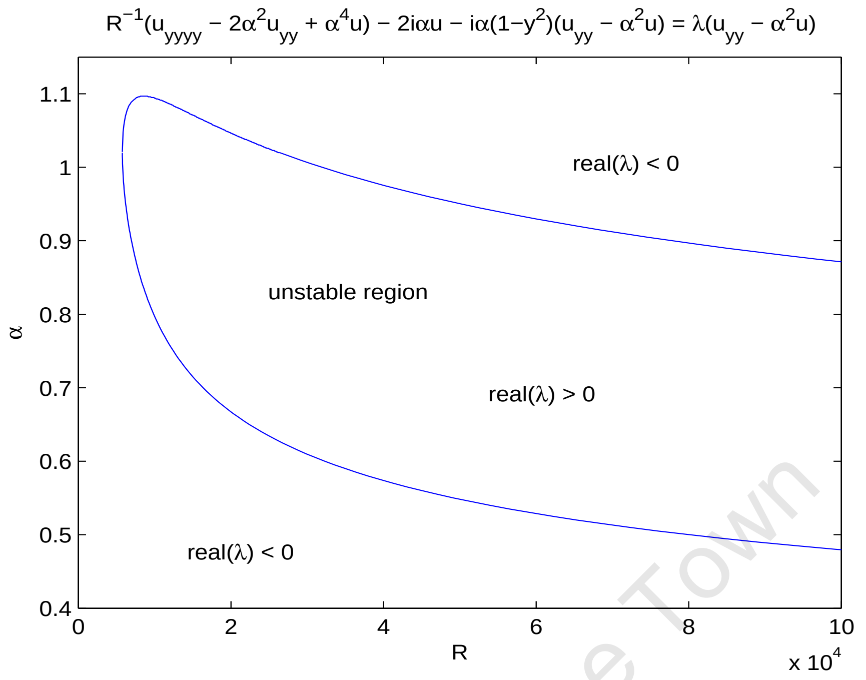

Figure 4.2: Marginal stability curve for plane Poiseuille flow. These solutions to the OS equation were obtained using a pseudospectral differentiation technique [Tref 01] and the Octave numerical package (see Appendices A and B).

concur, where the corresponding R_{crit} is computed as 5772.23 and $\alpha = 1.02$. We generated the curve in Figure 4.2 by employing a dichotomous search akin to the one employed by Liu and Oritz [Luio] for computing R_{crit} for plane Poiseuille flow. They used the Tau method described in [Luio] to solve high order OS differential eigenvalue problems. For a given α we chose two Reynolds numbers, one of which corresponded to not having any eigenvalues with a positive real part and the other as having (i.e. R_{min} and R_{max}). We would then repeatedly shrink and shift the interval until the difference between the Reynolds numbers was less than a desired tolerance parameter (for example 0.001) and that they satisfied the condition held by the initial R_{min} and R_{max}.

It is well documented that in practise the transition to turbulence for plane Poiseuille flow is much lower than predicted by the linear theory. Trefethen *et. al.* [Tref 93] reports that experiments have shown the critical Reynolds number to be around 1000. Slatter

[Slat 95] reports it to be around 2100. Similarly with plane Couette flow where the linear theory predicts the flow to be stable for all Reynolds numbers, in practise the transition to turbulence occurs at a Reynolds number of approximately 350. The resolution of these paradoxes is a long standing problem of fluid mechanics. Traditional hydrodynamic analysis as we have illustrated proceeds in two stages. First the problem is linearised about the laminar solution and then we search for unstable eigenvalues, i.e., λ with positive real parts. Initially it was speculated that the discrepancies between the linear theory and observed results were due to non-linearities, i.e., the first step. But it has emerged that the failure of the eigenvalue analysis may be attributed to the second stage. Two vectors ($\overrightarrow{u}$ and $\overrightarrow{v}$) are said to be orthogonal if their dot product $\overrightarrow{u} \cdot \overrightarrow{v} = 0$ (i.e. they are perpendicular) and a matrix/operator whose eigenfunctions/eigenvectors are orthogonal is said to be normal. Now if all the eigenvalues of a linear system are distinct, lie well inside the lower half-plane but their eigenfunctions are not orthogonal to one another then inputs to that system may be amplified by arbitrarily large factors [Tref 93]. As it happens both the operators that arise in plane Poiseuille and plane Couette flow are far from normal. These discoveries prompted Trefethen *et. al.* to investigate the possibilities of conducting hydrodynamic stability without the use of eigenvalues [Tref 93].

N	200	250	300
Standard Solver	0.26813148 − 0.00175034i	0.26813148 − 0.00175034i	0.26813148 − 0.00175034i
	0.94996175 − 0.04961370i	0.94996175 − 0.04961370i	0.94996175 − 0.04961370i
	0.94999384 − 0.04966078i	0.94999384 − 0.04966078i	0.94999384 − 0.04966078i
	0.33569896 − 0.05968989i	0.33569896 − 0.05968989i	0.33569896 − 0.05968989i
	0.90987242 − 0.08909505i	0.90987242 − 0.08909505i	0.90987242 − 0.08909505i
General Solver	0.26813149 − 0.00175040i	0.26813652 − 0.00174811i	0.26810103 − 0.00174742i
	0.94996179 − 0.04961375i	0.94996174 − 0.04961375i	0.94996115 − 0.04961346i
	0.94999385 − 0.04966073i	0.94999383 − 0.04966075i	0.94999407 − 0.04966055i
	0.33569892 − 0.05968995i	0.33569861 − 0.05968970i	0.33571393 − 0.05969680i
	0.90987241 − 0.08909505i	0.90987250 − 0.08909516i	0.90987394 − 0.08909491i

Table 4.1: 5 least stable eigenvalues computed for the plane Poiseuille problem using both Octave's standard and Matlab®'s general eigenvalue solvers. $R = 5000$, $\alpha = 1$.

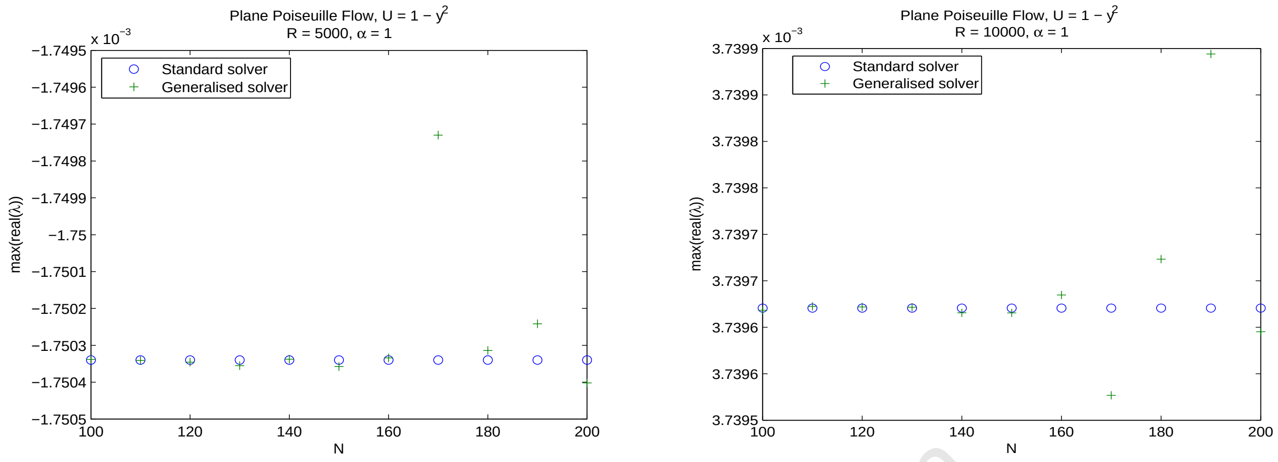

(a) $R = 5000, \alpha = 1$

(b) $R = 10000, \alpha = 1$

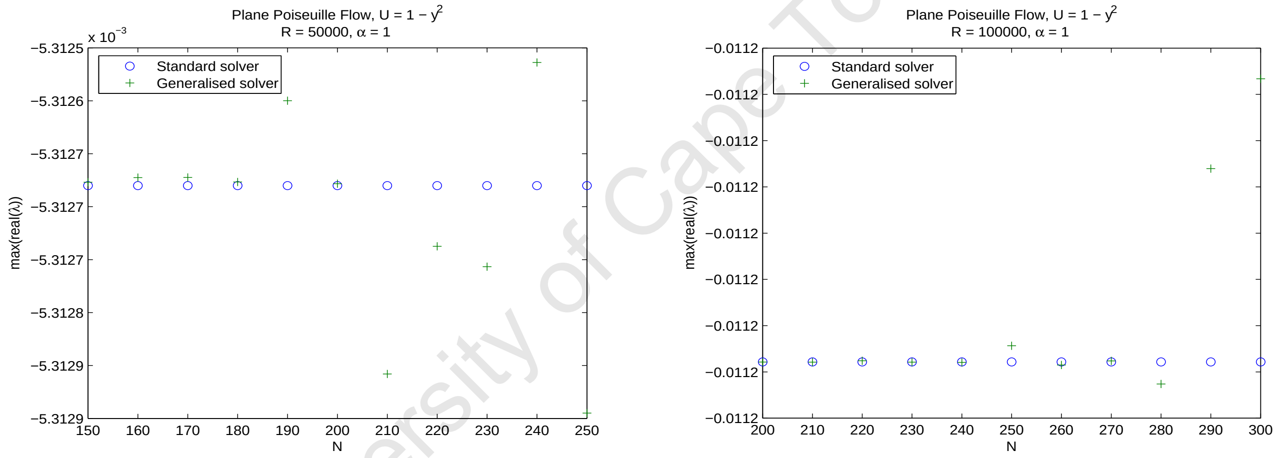

(c) $R = 50000, \alpha = 1$

(d) $R = 100000, \alpha = 1$

Figure 4.3: Comparison between Matlab®'s generalised and Octave's standard eigenvalue solvers. The real part of the most unstable eigenmode as a function of N for plane Poiseuille flow.

As mentioned above we used the Octave numerical package by reducing the problem to a standard eigenvalue problem, computing the eigenmodes for $B^{-1}A$ instead. In an attempt to determine whether there were any serious drawbacks to this approach we compare the eigenvalues that result from using Matlab®'s generalised eigenvalue solver to those from Octave's standard solver. In Figures 4.3a - 4.3d we have the maximum real part of $\lambda \equiv ic$ plotted as function of N (i.e., the number of intervals/number of polynomials used) for both the general and standard eigenvalue solvers. $\alpha = 1$ and $R = 5000$, $R = 10000$,

$R = 50000$ and $R = 100000$ in Figures 4.3a to 4.3d respectively. Table 4.1 shows the five modes with the largest real part of λ, which we refer to as the five most unstable or five least stable modes. They were computed using the general and standard solvers for $\alpha = 1$ and $R = 5000$ and $N = 200$, 250, 300. For the eight significant figures quoted there is no disagreement in the eigenmodes computed using the standard solver as N increases. This is not the case with the general solver where at best five significant figure agreement is achieved for either the real or imaginary parts (never both) of some eigenvalues. It is in this sense that we regard the standard eigenvalue solver more accurate but this requires further investigation. Throughout this work we take results to be more accurate if they agree to a higher number of significant figures. It will become evident as has been observed before [Dong] that computing the eigenmodes at high Reynolds numbers is extremely difficult. Hence the decrease in the accuracy of the results in Figure 4.3a to Figure 4.3d where R increases from 5000 to 100000.

Since both the plane Poiseuille and plane Couette hydrodynamic stability problems had previously been solved, we are able to compare our results with those found. The first solutions date as far back as the 1950's. Orszag [Orsz] reports that Shen [Shen], using asymptotic analysis developed by Lin [Linc] found $R_{\text{crit}} = 5360$, $\alpha_{\text{crit}} = 1$. Thomas [Thom 53] and Nachtsheim [Nach] as cited in [Orsz] both using finite difference methods found $R_{\text{crit}} = 5780$, $\alpha_{\text{crit}} = 1.026$ and $R_{\text{crit}} = 5767$, $\alpha_{\text{crit}} = 1.02$ respectively. Many authors compare their spectra for plane Poiseuille with those computed by Orszag in the aptly titled article, "Accurate solution of the Orr-Sommerfeld stability equation" [Orsz]. We follow suit. Chebyshev polynomials form the basis of Orszag's approximations to the eigenfunctions of the OS equations. He explains why they are better suited to the solutions of hydrodynamic stability problems than expansions in some other sets of orthogonal functions and finite difference methods. An important difference between Chebyshev and finite difference approximations is their order of accuracy. Orszag states that finite difference approximations provide only a finite order of accuracy in the sense that their errors behave asymptotically like $(\triangle x)^r$ for some finite r when the grid scale $\triangle x$ approaches zero. On the other hand if the steady-state velocity profile $U(y)$ in (3.10) is infinitely differentiable then the Chebyshev polynomials which he uses are of an infinite order in the sense that errors decrease more rapidly than any power of $1/M$ as $M \to \infty$, where M is the number of polynomials used in his approximation. This result can also be shown to hold for Legendre polynomials. Orszag, using single precision arithmetic, found $R_{\text{crit}} = 5772.22$, $\alpha_{\text{crit}} = 1.02056$; our computations concur (see Figure 4.2). As mentioned in Section 3.3, various authors define the perturbation (3.9) in different equivalent forms, which alters the way in which the instability criterion reads. Dongarra *et. al.* [Dong] as well as Acheson [Ache] define the perturbation as $\widehat{\psi} = \phi(y) \exp[i(\alpha x - bt)]$, where flows become linearly unstable when the $\Im(b) > 0$. Henceforth, when referring to the eigenvalues of the OS equation, we may either be referring to λ or a complex multiple thereof. In almost all instances unless otherwise stated we will be referring to $i\lambda = -c = b$. Orszag [Orsz, Table 5] also approximated the 32 least stable modes for $R = 10^4$, $\alpha = 1$. Setting $N = 94$, our results reached complete agreement with one exception (see below) with his list. The least stable eigenmode reads

$$-c = 0.23752649 + 0.00373967\text{i},$$

and is significant to 8 decimal places (i.e., as N increases the approximation converges and agrees to at least 8 significant figures). We however found an additional eigenvalue between positions 17 and 18 of [Orsz, Table 5],

17	$0.19005925 - 0.18282193\text{i}$
	$0.21272578 - 0.19936069\text{i}$
18	$0.79438839 - 0.20322067\text{i}$

More recently, Dongarra *et. al.* [Dong] also using Chebyshev polynomials as basis functions for approximations to the eigenfunctions of the OS equations, solved both the plane Poiseuille and plane Couette stability problems. They focused on determining the spectra in high Reynolds number ranges, which have previously proved to be very difficult. Arising in these difficult eigenvalue problems are highly sensitive spurious (unstable) eigenvalues. Spurious eigenvalues oscillate between very large negative and very large positive values as N changes. Having tested the sensitivity of the eigenvectors, Dongarra *et. al.* [Dong] concluded that the presence of spurious eigenvalues is connected to the discretisation procedure as opposed to the algorithms used to compute the eigenvalues. They believe that their Chebyshev tau-QZ algorithm is generally more accurate and efficient than finite difference methods. We continue by comparing our results with those of Dongarra *et. al.* [Dong], who takes a closer look at the behaviour of the eigenvalues. Since the eigenvalues are complex, it is both convenient and more informative to represent them graphically. As will become evident and is supported by [Dong], we are only able to compute the 'top ends' of the true eigenvalue spectra. In depictions of the spectra that follow we restrict our attention to this 'top end', considering only those eigenvalues ($i\lambda$) with imaginary parts greater than -1. In Figure 4.4, we have the spectra for plane Poiseuille flow approximated using a ≤ 202 degree polynomial and that reproduced from [Dong] for $R = 10^4$, $\alpha = 1$. Their [Dong] eigenvalues (i.e., for $R = 10^4$, $\alpha = 1$) are also in agreement with those computed by Orszag [Orsz, Table 5] and they also found the additional eigenvalue in between positions 17 and 18 stated above. In standard fluid dynamics notation, the left, right and lower branches of the plane Poiseuille spectra depicted in Figure 4.4 and those that follow, are known as the A, P and S branches respectively.

We mentioned that Dongarra *et. al.* focused on the more complex high Reynolds number calculations. Figures 4.5b, 4.5d and 4.5f depict the partial spectra for $R = 27000$ and $\alpha = 1$, computed using various numbers of polynomials. Next to them are the spectra reproduced from Dongarra *et. al.*. They determined the odd and even modes separately using M polynomials in each case. Figures 4.5a, 4.5c and 4.5e show only the (even) modes that result from using even Chebyshev polynomials. If $N = 2M$ then the even modes obtained when using N Chebyshev polynomials equal the modes obtained when using M even Chebyshev polynomials. Hence double the number of even and odd polynomials need to be employed to obtain (full) spectra equivalent to the spectra obtained when using only even polynomials. In Figures 4.5b, 4.5d and 4.5f, $N = 170$, $N = 400$ and $N = 600$ respectively. They depict the eigenvalues associated with both odd and even polynomials (i.e. the full spectrum). 64 bit arithmetic was used to compute Figures 4.5a - 4.5d and 4.5f, whereas extended precision (128 bit arithmetic) was employed to compute Figure 4.5e. These results reveal that the splitting of the tail of the approximate spectra (i.e. the S branch), is a consequence of employing too few polynomials. The splitting is therefore overcome by simply increasing the number of polynomials (N) used, even when only even polynomial interpolants are employed (see Figures 4.5a - 4.5d). Dongarra *et. al.* report that the eigenvalues near the intersection of the A, P and S branches are highly sensitive to round-off error. Increasing N from 400 to 600 as we do in Figures 4.5c and 4.5f does not result in the convergence to the 'limit' form observed in Figure 4.5e. They dub this the "triangle of numerical instability". It may be remedied by employing extended precision as illustrated by Figure 4.5e. To further highlight the complexities associated with solving the OS equation in high Reynolds number ranges we have in Table 4.2 the 12 least stable modes for $R = 10^5$, $\alpha = 1$. They were computed using $N = 100$ and $N = 300$. Together with these results we have the 12 least stable eigenmodes computed by Dongarra *et. al.*. As mentioned above they determined the even and odd modes separately, using $M = 200$ polynomials in each case. This is equivalent to using $N = 400$ polynomials for the full problem. For $N = 140$ we were able to match their [Dong] results to at least 7 significant figures and in some cases more than 7. Another phenomenon prevalent in these difficult computations is mode crossing. As R increases eigenvalues change positions in the sense that the imaginary part of one eigenvalue increases or decreases relative to another. Table 4.3 shows the 8 leading eigenvalues for $R = 80822$, $R = 80828$ and 80830. The structure of the eigenmodes observed for $R = 80822$ in Table 4.3 is maintained from $R = 10^4$ [Dong]. But at $R = 80828$ the two least stable modes exchange positions and then at $R = 80830$ the second and the third modes exchange positions. Mode crossing supports the argument that it is not sufficient when dealing with the stability of shear driven flows to simply trace the progression of a single supposedly least stable eigenvalue — at least a certain portion of the spectrum is required. Abdullah and Lindsay [Abdu] cited in [Dong] observe further mode crossing at higher Reynolds numbers.

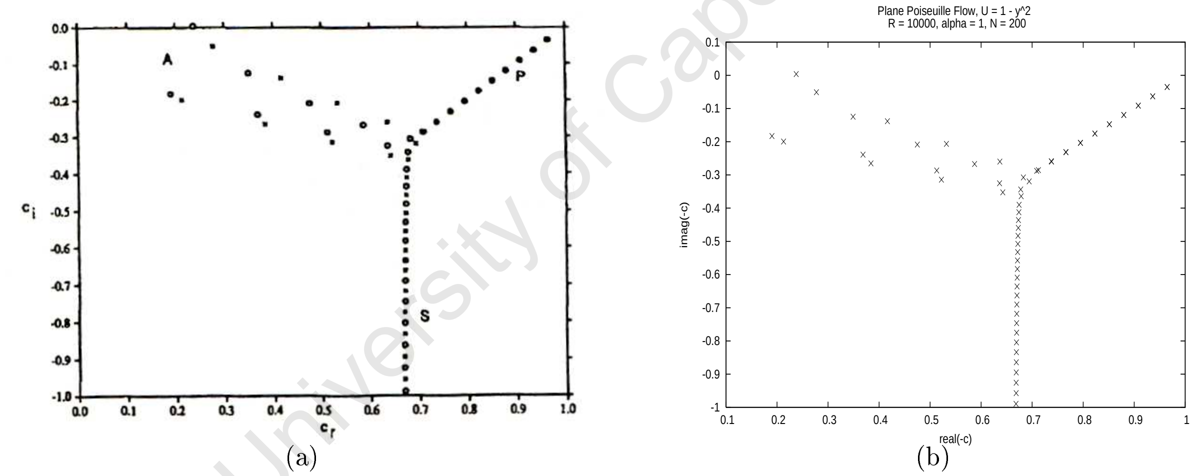

(a) (b)

Figure 4.4: Eigenvalue spectra for plane Poiseuille flow. $R = 10000$, $\alpha = 1$. (a) is reproduced from Dongarra *et. al.* [Dong] and (b) computed using 64 bit arithmetic with $N = 200$.

We observed that for plane Poiseuille flow as R increases more polynomials are required to accurately approximate the eigenmodes. For $R = 10^4$ using fewer than 100 polynomials we were able to reach complete agreement with Orszag's 32 least stable eigenvalues presented in [Orsz, Table 5]. By contrast, for $R = 10^5$ we required 140 polynomials to match Dongarra' *et. al.*'s 12 least stable modes listed in Table 4.2. However it seems that if one is only interested in a single most unstable mode, employing relatively few polynomials

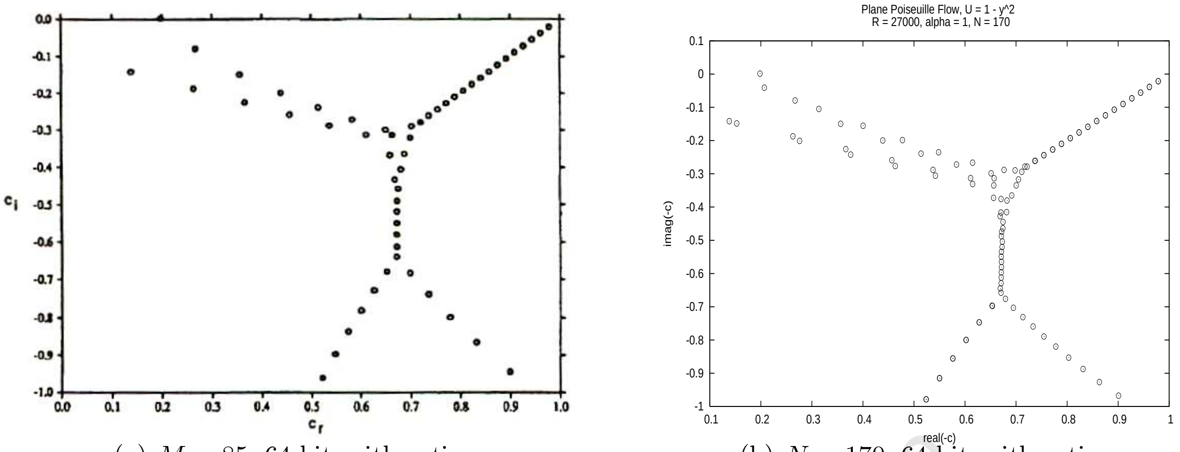

(a) $M = 85$, 64 bit arithmetic. (b) $N = 170$, 64 bit arithmetic.

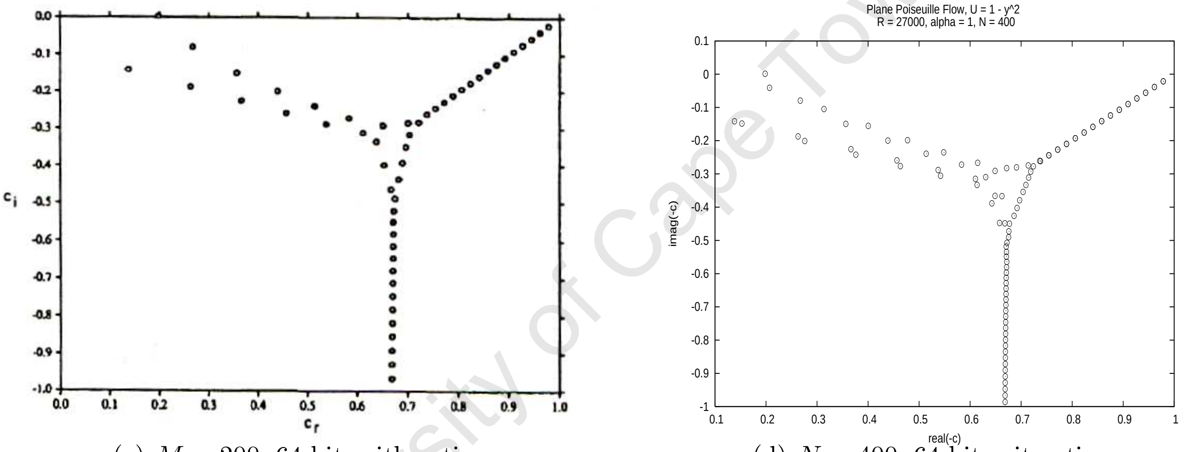

(c) $M = 200$, 64 bit arithmetic. (d) $N = 400$, 64 bit aritmetic.

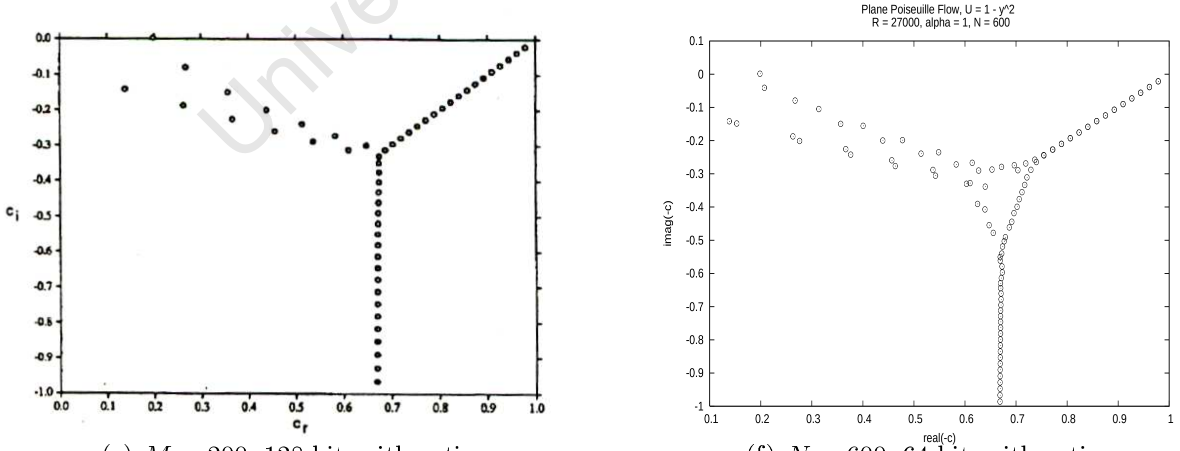

(e) $M = 200$, 128 bit arithmetic. (f) $N = 600$, 64 bit arithmetic

Figure 4.5: Eigenvalue spectra for plane Poiseuille flow. $R = 27000$, $\alpha = 1$. (a), (c) and (e) are reproduced from Dongarra *et. al.* [Dong] where they used M even polynomials. (b), (d) and (f) are full (i.e. both odd and even polynomials were employed) spectra.

$N = 100$	$N = 300$	Dongarra *et. al.* [Dong]
0.9888191009 − 0.0111625783i	0.9888191058 − 0.01116257892i	0.9888191058 − 0.01116257893i
0.9888195983 − 0.0111636079i	0.9888195933 − 0.01116360699i	0.9888195933 − 0.01116360699i
0.1459247885 − 0.0150420427i	0.1459247885 − 0.01504204266i	0.1459247829 − 0.01504203085i
0.9798754507 − 0.0200846843i	0.9798738045 − 0.02008374162i	0.9798738045 − 0.02008374163i
0.9798735582 − 0.0200854227i	0.9798751271 − 0.02008635541i	0.9798751271 − 0.02008635538i
0.9707368045 − 0.0289798271i	0.9709280339 − 0.02900433538i	0.9709280339 − 0.02900433538i
0.9711144244 − 0.0289991336i	0.9709305304 − 0.02900898109i	0.9709305305 − 0.02900898101i
0.1373944866 − 0.0295636002i	0.1373944864 − 0.02956360013i	0.1373944878 − 0.02956356969i
0.9622955057 − 0.0342319983i	0.1982003544 − 0.03733101359i	0.1982003566 − 0.03733100660i
0.9561584759 − 0.0345394387i	0.9619817790 − 0.03792441474i	0.9619817790 − 0.03792441466i
0.9486175992 − 0.0348922613i	0.9619857992 − 0.03793148468i	0.9619857994 − 0.03793148490i
0.9409921941 − 0.0352947965i	0.9530350178 − 0.04684401412i	0.9530350180 − 0.04684401422i

Table 4.2: The 12 least stable eigenvalues for plane Poiseuille flow. $R = 10^5$, $\alpha = 1$.

	$R = 80822$	$R = 80828$	$R = 80830$
1	0.15555539 − 0.0124140i	0.98756345 − 0.0124138i	0.98756360 − 0.0124136i
2	0.98756299 − 0.0124142i	0.15555211 − 0.0124151i	0.98756425 − 0.0124149i
3	0.98756364 − 0.0124156i	0.98756410 − 0.0124151i	0.15555102 − 0.0124154i
4	0.97761258 − 0.0223345i	0.97761341 − 0.0223337i	0.97761369 − 0.0223334i
5	0.97761435 − 0.0223379i	0.97761518 − 0.0223371i	0.97761546 − 0.0223368i
6	0.14702381 − 0.0312463i	0.14702035 − 0.0312457i	0.14701919 − 0.0312455i
7	0.96766152 − 0.0322540i	0.96766273 − 0.0322528i	0.96766313 − 0.0322524i
8	0.96766488 − 0.0322601i	0.96766608 − 0.0322589i	0.96766648 − 0.0322585i

Table 4.3: 8 least stable eigenvalues for $R = 80822$, $R = 80822$ and $R = 80830$, which serves as evidence of the phenomenon known as mode crossing. $\alpha = 1$, $N = 400$.

may be sufficient. In dealing with these sensitive eigenvalue approximations, it is not simply a case of employing additional polynomials to increase their accuracy. Increasing the number of polynomials compounds the round-off error. A balance needs to be struck between employing a sufficient number of polynomials and the precision employed.

4.2.2 Plane Couette flow

We have shown in Section 3.2 that the plane Couette hydrodynamic stability problem is solved subject to the same boundary conditions as the plane Poiseuille problem. The only differences in their respective OS equations and consequently their numerical schemes

R	$N = 100$	$N = 150$	$N = 200$
10^5	$-0.9118645 - 0.0234866i$	$0.9118645 - 0.0234866i$	$-0.9118645 - 0.0234866i$
	$0.9118645 - 0.0234866i$	$-0.9118645 - 0.0234866i$	$0.9118645 - 0.0234866i$
	$0.0000000 - 0.0333195i$	$-0.8630792 - 0.0546212i$	$0.8630792 - 0.0546212i$
	$0.0314801 - 0.0333518i$	$0.8630792 - 0.0546212i$	$-0.8630792 - 0.0546212i$
	$-0.0314801 - 0.0333518i$	$-0.9347750 - 0.0651843i$	$0.9347750 - 0.0651843i$
	$0.0629304 - 0.0334489i$	$0.9347750 - 0.0651843i$	$-0.9347750 - 0.0651843i$
	$N = 300$	$N = 400$	$N = 500$
10^6	$0.9588871 - 0.0107536i$	$0.9588871 - 0.0107536i$	$0.9588871 - 0.0107536i$
	$-0.9588871 - 0.0107536i$	$-0.9588871 - 0.0107536i$	$-0.9588871 - 0.0107536i$
	$-0.9361798 - 0.0251774i$	$0.9361798 - 0.0251774i$	$-0.9361798 - 0.0251774i$
	$0.9361798 - 0.0251774i$	$-0.9361798 - 0.0251774i$	$0.9361798 - 0.0251774i$
	$-0.0000000 - 0.0299679i$	$-0.9699552 - 0.0303560i$	$0.9699552 - 0.0303560i$
	$-0.0104905 - 0.0299711i$	$0.9699552 - 0.0303560i$	$-0.9699552 - 0.0303560i$
	$N = 150$	$N = 400$	$N = 500$
10^{12}	−9.9912E-01 + 3.9719E-06i	5.2283E-13 − 5.2521E-08i	−5.4435E-12 − 8.2317E-08i
	9.9912E-01 + 3.9719E-06i	−1.5707E-02 − 5.2533E-08i	1.2566E-02 − 8.2330E-08i
	2.0942E-02 − 7.1993E-09i	1.5707E-02 − 5.2533E-08i	−1.2566E-02 − 8.2330E-08i
	−2.0942E-02 − 7.1993E-09i	−3.1411E-02 − 5.2572E-08i	2.5130E-02 − 8.2368E-08i
	−6.2791E-02 − 7.2233E-09i	3.1411E-02 − 5.2572E-08i	−2.5130E-02 − 8.2368E-08i
	6.2791E-02 − 7.2233E-09i	−4.7107E-02 − 5.2635E-08i	3.7690E-02 − 8.2433E-08i

Table 4.4: 6 least stable eigenmodes for plane Couette flow. $\alpha = 1$, 64 bit arithmetic.

arise as a result of their steady profiles (i.e. U and consequently U_{yy} in (3.10)). Remember that Couette flow is achieved by shearing the top plate whilst holding the bottom plate stationary or shearing both plates in opposite directions, i.e., $U(y) = y$. Our results concur with the linear theory predictions found in the literature [Chap, Draz], where Couette flow was found to be stable for all R. We were not able to find a numerically stable eigenmode with a positive imaginary part, i.e., $\Im(\mathrm{i}\lambda) > 0 \Longrightarrow \Re(\lambda) > 0$. Here the modes appear as conjugate pairs. In Table 4.4 we have the 6 least stable eigenmodes computed for $R = 10^5$, 10^6 and 10^{12}. We varied N to establish how many polynomials are needed to achieve numerically stable results. As observed with Poiseuille flow, as R increases the number of polynomials required also increases. For $R = 10^5$, $N = 150$ was sufficient to compute the 6 least stable modes in Table 4.4, whereas for $R = 10^6$ more than double the number of polynomials were required. Using $N = 150$ for $R = 10^{12}$ we found an unstable eigenmode but as can be observed from Table 4.4, for R of this order the results are no longer numerically stable.

We turn our attention to plotting the spectra for Couette flow and comparing it with results found in [Dong]. It becomes evident that this is no trivial eigenvalue problem. Dongarra *et. al.* relates that a colleague of theirs experienced great difficulty with computing the eigenvalues for R as low as 2000. Figures 4.6a - 4.6d depict the approximate spectra computed for $R = 5000$, 4000, 3000 and 2000 respectively using 64 bit arithmetic. The numerical instability that results from rounding off is visible at Reynolds numbers lower than 3000. As with plane Poiseuille flow, it is the eigenvalues in the region of the intersection of the A, P and S branches that are most sensitive to round-off error (see Figures 4.6a - 4.6c). Dongarra *et. al.* [Dong] observed breakdown near the intersection at approximately $R = 3500$. This is overcome again by increasing the precision, employing 128 bit arithmetic. Using extended precision they [Dong] proceeded to compute accurate spectra for R up to 13000. Figure 4.7 shows the spectra computed for $R = 13000$ and $\alpha = 1$ using 200 polynomials and 128 bit arithmetic. In comparison with its Poiseuille counterpart where an accurate spectra for $R = 10^4$ was computed using 64 bit arithmetic, for Couette flow 128 bit arithmetic is required for R as low as 3000. We should however remember that in practise plane Couette flow develops into turbulence, whereas the linear stability theory predicts that it is stable for all R. This eigenvalue analysis may therefore not be an appropriate tool for determining its instability.

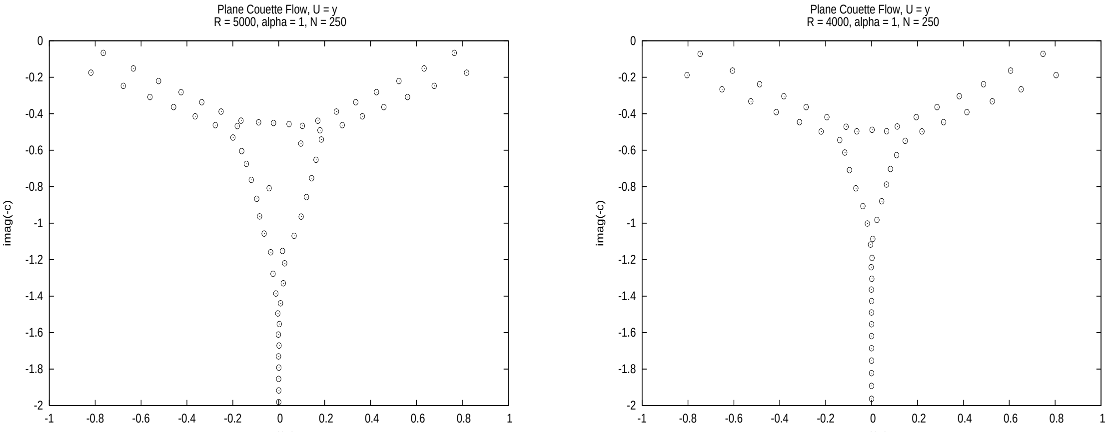

(a) $R = 5000, N = 250$ (b) $R = 4000, N = 250$

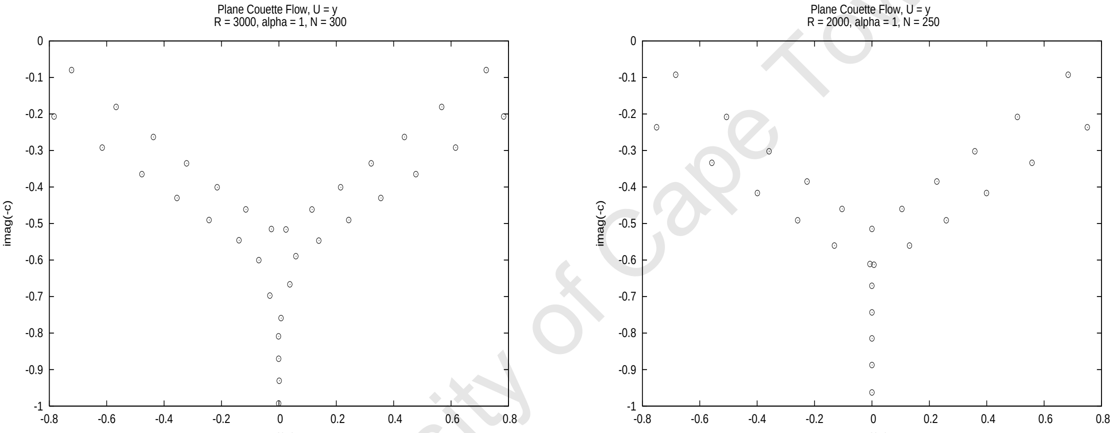

(c) $R = 3000, N = 300$ (d) $R = 2000, N = 250$

Figure 4.6: Approximate spectra for plane Couette flow. $\alpha = 1$, 64 bit arithmetic.

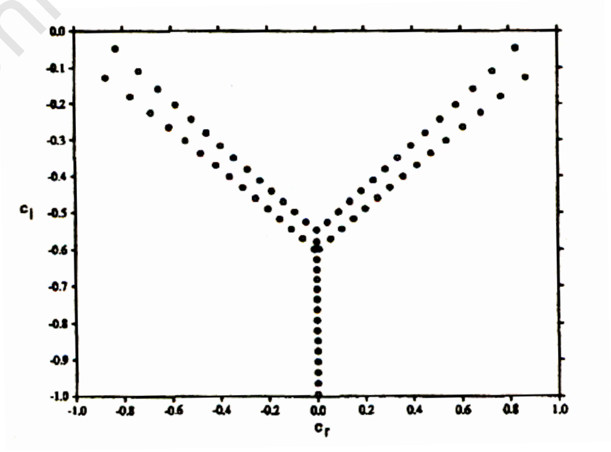

Figure 4.7: The spectrum for plane Couette flow reproduced from Dongarra *et. al.* [Dong] using 200 polynomials. $R = 13000$, $\alpha = 1$, 128 bit arithmetic.

4.3 Newtonian Open Channel Flow

We recall from Sections 3.2.3 that the Newtonian open channel OS (3.10) problem, where

$$U = -\frac{y^2}{4} + \frac{y}{2} + \frac{3}{4}, \tag{4.8}$$

is solved with $\phi(\pm 1) = \phi_y(-1) = \phi_{yy}(1) = 0$. Here the OS eigenvalue problem differs from the plane Poiseuille equivalent in two respects. First with regard to their steady-state profiles, U and consequently U_{yy}, and second with regard their boundary conditions. The first difference as with plane Couette flow, simply involves setting the values of U and U_{yy} in (3.10) to as they apply for open channel flow (4.8). There are two differential operators in the OS problem which we need to approximate, i.e., D^2 (second order) and D^4 (fourth order) in (4.6). As described in Section 4.2.1 we enforce the homogeneous Dirichlet boundary conditions, $\phi(\pm 1) = 0$ when approximating D^2. Its approximation, $\widetilde{\mathrm{D}^2}$ is thus the square of the Chebyshev differentiation matrix, D_N with its first and last, rows and columns removed. With D^4, all four boundary conditions need to be imposed. For closed channel flows the boundary conditions were only imposed up to the first derivative of the interpolating polynomials, but for open channel flow a boundary condition needs to be imposed on the second derivative of ϕ. Remember from Section 4.2.1 that we implement the boundary conditions by restricting ourselves to interpolants that satisfy them. We thus set the polynomial interpolant

$$u(y) = s(y)\, q(y), \tag{4.9}$$

where $q(y)$ is a polynomial of degree $\leq N$ with $q(\pm 1) = 0$. For plane Poiseuille flow we had $s(y) = 1 - y^2$. $u(y)$ thus corresponded to a polynomial of degree $\leq N + 2$ with

$u(\pm 1) = u_y(\pm 1) = 0$. Since

$$\begin{aligned} u_y &= s_y q + s q_y \\ u_{yy} &= s_{yy} q + 2 s_y q_y + s q_{yy}, \end{aligned}$$

we require an $s(y)$ with $s(\pm 1) = s_y(1) = 0$ to satisfy $u(\pm 1) = u_y(-1) = u_{yy}(1) = 0$. A polynomial of the lowest degree satisfying these conditions must be a cubic, for example $s(y) = y^3 - y^2 - y + 1$. Hence we set

$$u(y) = \left(y^3 - y^2 - y + 1\right) q(y).$$

$u(y)$ now corresponds to a polynomial of degree $\leq N+3$ with $u(\pm 1) = u_y(-1) = u_{yy}(1) = 0$. We continue as we did when deriving an approximate for D^4 for closed channel flow, by differentiating $u(y)$ four times to obtain

$$u_{yyyy}(y) = \left(y^3 - y^2 - y + 1\right) q_{yyyy}(y) + 4\left(3y^2 - 2y - 1\right) q_{yyy}(y) + 6(6y - 2) q_{yy} + 24 q_y,$$

but since $q(y_j) = \frac{u(y_j)}{\left(y_j^3 - y_j^2 - y_j + 1\right)}$, the fourth derivative operator approximate for open channel flow reads

$$\begin{aligned} \widetilde{\mathrm{D}^4} = & \left[\operatorname{diag}\left(y_j^3 - y_j^2 - y_j + 1\right) D_N^4 + 4\operatorname{diag}\left(3y_j^2 - 2y_j - 1\right) D_N^3 + 6\operatorname{diag}(6y_j - 2) D_N^2 \right. \\ & \left. + 24 D_N\right] \times \operatorname{diag}\left(1 / \left(y_j^3 - y_j^2 - y_j + 1\right)\right), \end{aligned}$$

where D_N is a Chebyshev differentiation matrix as defined in Section 4.1. D_N, D_N^2, D_N^3 and D_N^4 have their first and last rows and columns removed.

Table 4.5 shows the 5 least stable eigenmodes computed for $R = 10^2$, 10^3 and 10^4 using 150, 250 and 350 polynomials. We observe a strange phenomenon where the imaginary part of the leading eigenmode is large positive and increases as N increases. This is

R	$N = 150$	$N = 250$	$N = 350$
10^2	$0.998244 + 612517.614893i$	$0.998920 + 4698694.792179i$	$0.999221 + 18005012.833740i$
	$0.615117 - 0.148587i$	$0.615095 - 0.148623i$	$0.615089 - 0.148636i$
	$0.704725 - 0.326278i$	$0.704704 - 0.326278i$	$0.704699 - 0.326277i$
	$0.678341 - 0.367567i$	$0.678274 - 0.367561i$	$0.678256 - 0.367556i$
	$0.645372 - 0.586218i$	$0.645432 - 0.586311i$	$0.645446 - 0.586337i$
10^3	$0.998244 + 61251.761489i$	$0.998920 + 469869.479218i$	$0.999221 + 1800501.283374i$
	$0.884552 - 0.076235i$	$0.884535 - 0.076238i$	$0.884530 - 0.076239i$
	$0.354605 - 0.077553i$	$0.354596 - 0.077587i$	$0.354593 - 0.077596i$
	$0.918253 - 0.116700i$	$0.918238 - 0.116710i$	$0.918234 - 0.116713i$
	$0.792065 - 0.157370i$	$0.792042 - 0.157377i$	$0.792036 - 0.157375i$
10^4	$0.998244 + 6125.176149i$	$0.998920 + 46986.947922i$	$0.999221 + 180050.128337i$
	$0.962735 - 0.024624i$	$0.962725 - 0.024626i$	$0.962723 - 0.024626i$
	$0.974814 - 0.037349i$	$0.974806 - 0.037355i$	$0.974803 - 0.037356i$
	$0.181299 - 0.040482i$	$0.181295 - 0.040502i$	$0.181294 - 0.040508i$
	$0.932800 - 0.051028i$	$0.932786 - 0.051032i$	$0.932782 - 0.051033i$

Table 4.5: 5 least stable approximate eigenmodes for Newtonian open channel flow that result from setting $s(y) = y^3 - y^2 - y + 1$ in (4.9). $\alpha = 1$.

R	$N = 150$	$N = 250$	$N = 350$
10^2	$0.499416 + 618541.905403i$	$0.499640 + 4726561.308263i$	$0.499740 + 18081448.501308i$
	$0.498191 + 612517.615144i$	$0.498901 + 4698694.805991i$	$0.499211 + 18005012.826478i$
	$0.615031 - 0.148673i$	$0.615064 - 0.148654i$	$0.615075 - 0.148650i$
	$0.704669 - 0.326243i$	$0.704683 - 0.326265i$	$0.704688 - 0.326272i$
	$0.678285 - 0.367468i$	$0.678253 - 0.367525i$	$0.678243 - 0.367540i$
10^3	$0.499416 + 61854.190128i$	$0.499640 + 472656.130737i$	$0.499740 + 1808144.850098i$
	$0.498191 + 61251.761926i$	$0.498901 + 469869.480688i$	$0.499211 + 1800501.282680i$
	$0.884553 - 0.076235i$	$0.884535 - 0.076238i$	$0.884530 - 0.076239i$
	$0.354479 - 0.077611i$	$0.354550 - 0.077607i$	$0.354569 - 0.077606i$
	$0.918253 - 0.116700i$	$0.918238 - 0.116710i$	$0.918234 - 0.116713i$
10^4	$0.499416 + 6185.414895i$	$0.499640 + 47265.612184i$	$0.499740 + 180814.484686i$
	$0.498190 + 6125.180311i$	$0.498901 + 46986.948958i$	$0.499211 + 180050.128592i$
	$0.962735 - 0.024624i$	$0.962725 - 0.024626i$	$0.962723 - 0.024626i$
	$0.974814 - 0.037349i$	$0.974806 - 0.037355i$	$0.974803 - 0.037356i$
	$0.181169 - 0.040516i$	$0.181248 - 0.040514i$	$0.181270 - 0.040514i$

Table 4.6: 5 least stable approximate eigenmodes for Newtonian open channel flow that result from setting $s(y) = y^4 - 2y^2 + 1$ in (4.9). $\alpha = 1$.

observed for Reynolds numbers as low as 10^{-2}, which would erroneously imply that there are not any stable open channel flows. One would expect the flow to be stable at a sufficiently low R. The next four eigenmodes, where they are arranged according to the magnitudes of their imaginary parts, are numerically stable but not to the degree observed for the previous flows investigated. We also observe that for a given N as the Reynolds number increases by a factor of ten (e.g. from 10^2 to 10^3) the imaginary part of the leading eigenvalue decreases by almost exactly the same factor (see Table 4.5).

We continue with our open channel eigenvalue stability investigation by increasing the degree of the polynomial interpolant used to approximate D^4 to $\leq N+4$ and observe the behaviour of the eigenmodes. An $s(y)$ in (4.9) of degree 4 that satisfies $s(\pm 1) = s_y(1) = 0$ is required. We set $s(y) = y^4 - 2y^2 + 1$. $\widetilde{\mathrm{D}^4}$ now reads

$$\begin{aligned}\widetilde{\mathrm{D}^4} \;=\; & \Big[\mathrm{diag}\left(y_j^4 - 2y_j^2 + 1\right) D_N^4 + 4\mathrm{diag}\left(4y^3 - 4y_j\right) D_N^3 + 6\mathrm{diag}\left(12y_j^2 - 4\right) D_N^2 \\ & +96\mathrm{diag}\left(y_j\right) D_N + \mathrm{diag}\left(24\right)\Big] \times \mathrm{diag}\left(1/\left(y_j^4 - 2y_j^2 + 1\right)\right).\end{aligned}$$

In Table 4.6 we have the resulting 5 most unstable eigenmodes computed for $R = 10^2$, 10^3 and 10^4 using 150, 250 and 350 polynomials. Apart from the two least stable eigenvalues, the rest are in agreement with those computed using the polynomial interpolant of degree $\leq N+3$ (see Table 4.5). We found an additional eigenvalue, less stable than the leading eigenvalue shown in Table 4.5. Hence eigenmode i in Table 4.5 corresponds to eigenmode $i+1$ in Table 4.6, where they are ordered according to decreasing imaginary part and $i = 1, \ldots., N-2$. The real part of eigenmode 2 in Table 4.6 is approximately half that of what it was in Table 4.5 (i.e., eigenmode 1), but their corresponding imaginary parts are the same. The two leading eigenvalues display the same peculiar numerical instability. Their imaginary parts are large positive and increase with N. We also observe that as R increases by a factor of 10 the imaginary parts of these eigenmodes also decrease by a factor of 10. Both the $\leq N+3$ and $\leq N+4$ degree interpolants used to approximate D^4 in the open channel OS problem satisfy the necessary boundary conditions and the latter obtains the eigenmodes computed by the former.

Assuming that the boundary conditions are implemented correctly, these leading eigenvalues behave like spurious modes described in Section 4.2.1. Though they do not oscillate between large positive and negative values, they are large positive and increase with N. Spurious eigenmodes are common in these complex problems. If it be the case that these leading eigenmodes are spurious then they should be ignored when testing for the onset of turbulence. In doing so we did not find any numerically stable unstable eigenmodes (i.e. numerically stable λ where $\Re(\lambda) > 0$). This implies that according to the linear stability theory, open channel flow like plane Couette flow is stable for all Reynolds numbers. We are reminded that in practice the latter develops into turbulent flow at a Reynolds number lower than that for plane Poiseuille. The linear theory predicts that plane Poiseuille flow becomes unstable at $R \approx 5772.3$.

We briefly return to plane Poiseuille flow as our results concur with those found in the relevant literature (see Section 4.2.1). Recall that if we set $s(y) = 1 - y^2$ in (4.9), the resulting fourth derivative approximate is the one we used to solve the Newtonian closed channel problems. In Table 4.7 we have the 10 most unstable eigenmodes computed for $R = 10^4$, $\alpha = 1$ and $N = 400$ using the fourth derivative operator approximates that result from setting $s(y) = 1 - y^2$, $s(y) = y^3 - y^2 - y + 1$ and $s(y) = y^4 - 2y^2 + 1$ in (4.9). Each of the resulting operator approximates satisfy the boundary conditions implemented by the preceding approximate, i.e., the polynomial interpolant (4.9) constructed using $s(y) = y^4 - 2y^2 + 1$ satisfies the boundary conditions imposed by the interpolant constructed using $s(y) = y^3 - y^2 - y + 1$. The same relation holds for $s(y) = y^3 - y^2 - y + 1$ and $s(y) = 1 - y^2$. Each of the interpolants therefore satisfy the closed channel OS boundary conditions, i.e. $\phi(\pm 1) = \phi_y(\pm 1) = 0$. From Table 4.7 it is observed that each interpolant obtains the eigenvalues of the preceding interpolant and a new leading eigenvalue. These new eigenvalues obtained when setting $s(y) = y^3 - y^2 - y + 1$ and $s(y) = y^4 - 2y^2 + 1$ are numerically unstable displaying similar characteristics to those observed for the leading eigenvalues in Tables 4.5 and 4.6 for Newtonian open channel flow. Their imaginary parts are large positive and increase with N. Now, the eigenmodes computed by setting $s(y) = 1 - y^2$ are correct in that they agree with those quoted in the literature [Dong, Orsz]. All three of the resulting interpolants satisfy the boundary conditions for plane Poiseuille flow. The additional misbehaving eigenvalues that we obtain with the increase in the order of the $s(y)$ do not form part of the plane Poiseuille hydrodynamic solution as quoted earlier in this chapter, which strongly suggest that they are spurious eigenvalues (see Section 4.2.1). They could be as a result of the extra zeros for u in (4.9), introduced with the increases in the degree of s. It would seem that these observations support our initial speculations that the leading unstable eigenvalues computed for Newtonian open channel flow do not form part of the solution and hence according to the linear stability theory Newtonian open channel flow is stable for all Reynolds numbers.

	$s(y) = 1 - y^2$	$s(y) = y^3 - y^2 - y + 1$	$s(y) = y^4 - 2y^2 + 1$
1	0.2375265 + 0.0037397i	−0.0027677 + 306914.6930824i	−0.0009118 + 308055.5078213i
2	0.9646309 − 0.0351673i	0.2375264 + 0.0037396i	−0.0027678 + 306914.6662283i
3	0.9646425 − 0.0351866i	0.9646309 − 0.0351673i	0.2374975 + 0.0037396i
4	0.2772043 − 0.0508987i	0.9646425 − 0.0351866i	0.9646309 − 0.0351673i
5	0.9363165 − 0.0632015i	0.2771713 − 0.0508999i	0.9646425 − 0.0351866i
6	0.9363518 − 0.0632516i	0.9363165 − 0.0632016i	0.2771713 − 0.0508999i
7	0.9079831 − 0.0912227i	0.9363518 − 0.0632516i	0.9363165 − 0.0632015i
8	0.9080563 − 0.0913129i	0.9079829 − 0.0912227i	0.9363518 − 0.0632516i
9	0.8796273 − 0.1192329i	0.9080563 − 0.0913129i	0.9079831 − 0.0912227i
10	0.8797557 − 0.1193707i	0.8796272 − 0.1192323i	0.9080563 − 0.0913129i

Table 4.7: 10 least stable eigenmodes for plane Poiseuille flow. They are computed using the interpolants that result from setting $s(y) = 1 - y^2$, $s(y) = y^3 - y^2 - y + 1$ and $s(y) = y^4 - 2y^2 + 1$ in (4.9). $R = 10^4$, $\alpha = 1$, $N = 400$.

It could be that the open channel OS operators, like the plane Poiseuille and plane Couette operators, are non-normal and hence this eigenvalue analysis is inappropriate for determining its instability. Alternatively the instability observed in practice for open channel flow is not the result of viscous but possibly free surface effects. Our current hydrodynamic stability model does not capture the instability introduced as a result of variation in the free surface height. Either way alternate hydrodynamic stability analyses are needed.

4.4 Non-Newtonian Closed Channel Flow

We have reproduced the marginal stability curve for plane Poiseuille flow and examined the behaviour of the eigenvalues for both the plane Poiseuille and plane Couette hydrodynamic stability problems. Our results are in accordance with those presented in the relevant fluid dynamics literature [Orsz, Dong]. It is with this knowledge that we aim to extend our results, investigating the linear stability of non-Newtonian closed channel flow next.

The OS equation is derived on the assumption that viscosity of the fluid remains constant. With non-Newtonian fluids this assumption no longer holds and hence the OS equation does not necessarily apply. But for some non-Newtonian fluids in some flow regimes, the departure from constant viscosity may be quite small. It is for these weakly non-Newtonian fluids or shear rate ranges that we postulate the OS equation would form a reliable approximation of their linear hydrodynamic stability. In the analyses that follow we, like Myers [Myer] for two-dimensional thin film flow, set $\dot{\gamma} = |u_y|$. The shear rate is at a maximum at the channel walls.

As mentioned before, despite its many drawbacks theoreticians persist in using the power-law model (Section 1.3.1.1). Its flow profiles are simple and predominantly used as a starting point. We follow suit. Thereafter we use the Ellis model to approximate non-Newtonian flow and investigate its stability. The Ellis model unlike the power-law model exhibits the proper limiting behaviour.

4.4.1 Closed channel power-law flow

In power-law fluids the shear stress-strain relation can be expressed by

$$\tau = K\dot{\gamma}^{n}$$

and its viscosity by

$$\eta = K\dot{\gamma}^{n-1}.$$

n is the measure by which the respective fluid deviates from the Newtonian norm ($n = 1$ for a Newtonian fluid). Their flow in a horizontal channel is governed by

$$K\left|u_y\right|^{n-1}\left|u_y\right| = p_x y \tag{4.10}$$

and driven in the positive x direction by a negative pressure gradient, $p_x < 0$ [Myer]. (4.10) is solved subject to the no-slip boundary conditions, i.e. $u(\pm 1) = 0$. The resulting steady-state profile reads

$$u = \frac{n\left(\frac{p_x}{K}\right)^{\frac{1}{n}}}{n+1}\left(1 - |y|^{1+\frac{1}{n}}\right)$$

for $-1 \leq y \leq 1$. Given the fluid flux,

$$Q = \int_{-1}^{1} u dy,$$

we compute the pressure gradient required to drive the flow. It is

$$p_x = -K\left(\frac{Q(1+2n)}{2n}\right)^{n}.$$

This implies that u is linear in Q, hence the fluid flux does not influence the shape of the flow profile, only the maximum velocity attained across the channel. Figure 4.8 shows examples of power-law closed channel steady-state flow profiles for $n < 1$ (a pseudoplastic fluid) and $n > 1$ (a dilatant fluid). Figure 4.9 depicts power-law viscosity curves as functions of the shear rate at the channel wall (i.e. $y = \pm 1$) for various n. It is evident from both these figures that the larger $|n-1|$, the more the viscosity changes with the the shear rate. This means the larger $|n-1|$, the more non-Newtonian the flow. Power-law fluids with n near 1 have nearly constant viscosity and are therefore weakly non-Newtonian. We use the OS equation to approximate their hydrodynamic stability.

We consider the power-law profile in the following form

$$U = 1 - |y|^{1+\frac{1}{n}}, \tag{4.11}$$

where its maximum velocity, like that of both the Newtonian profiles investigated is 1. For the OS solver we also need

$$U_{yy} = -\frac{n+1}{n^2} \mid y \mid^{\frac{1-n}{n}} .$$

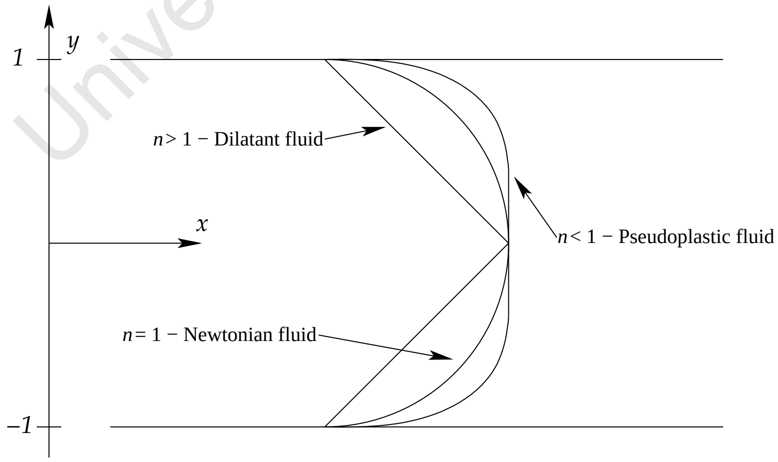

Figure 4.8: Closed channel power-law steady-state flow profiles (4.11).

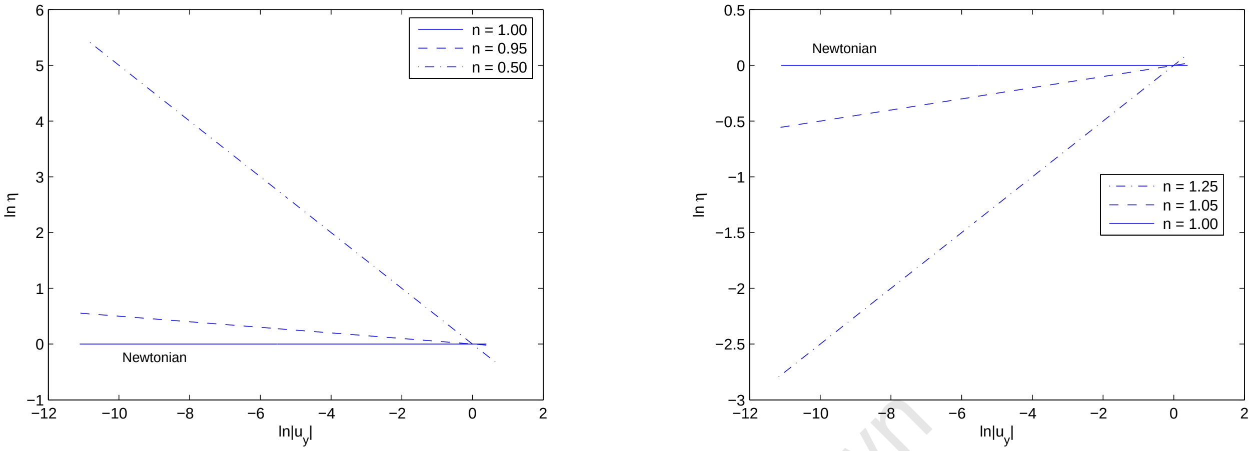

Figure 4.9: Power-law viscosity curves (1.3). $K = 1$.

R_{unstable}	n							
N	1.25	1.01	1.00	0.99	0.97	0.90	0.50	0.40
200	∞	5620.2	5772.3	5927.9	6237.7	7351.2	24312.0	38397.1
225	3625.0	5651.3	5772.3	5897.3	6159.8	7231.2	24309.4	38397.1
250	∞	5625.7	5772.3	5921.2	6219.7	7323.0	24311.3	38397.1
275	3624.4	5651.2	5772.3	5897.4	6160.2	7232.4	24309.7	38397.1
300	∞	5629.5	5772.3	5917.0	6208.4	7305.6	24311.0	38397.1
325	3624.1	5651.2	5772.3	5897.5	6160.4	7233.3	24309.8	38397.1
350	∞	5633.3	5772.3	5913.3	6199.4	7293.5	24310.7	38397.1
375	3623.8	5651.1	5772.3	5897.5	6160.6	7233.9	24309.9	38397.1
400	∞	5634.5	5772.3	5911.8	6195.2	7285.5	24310.6	38397.1
425	3623.7	5651.1	5772.3	5897.6	6160.7	7234.4	24310.0	38397.1
450	∞	5636.2	5772.3	5910.1	6191.0	7279.2	24310.5	38397.1
475	3623.5	5651.0	5772.3	5897.6	6160.9	7234.7	24310.0	38397.1
500	∞	5637.6	5772.3	5908.8	6187.7	7274.3	24310.4	38397.1
575	3623.4	5651.0	5772.3	5897.6	6160.0	7235.3	24310.0	38397.1
600	∞	5639.8	5772.3	5906.9	6182.9	7267.2	24310.4	38397.1

Table 4.8: The least R with an unstable eigenmode (R_{unstable}), computed using $N = 200, 225, 250, \ldots, 500, 575, 600$ for $\alpha = 1.02$ and $n = 1.25, 1.01, 1.00, 0.99, 0.97, 0.90, 0.50, 0.40$ in (4.11). The eigenmodes for some n behave differently depending on whether odd or even N is used. ∞ denotes that there were not any numerically stable unstable modes for $R < 10^{10}$.

In Table 4.8 for $\alpha = 1.02$ and $n = 1.25, 1.01, 1.00, 0.99, 0.97, 0.90, 0.50, 0.40$, we list the least R with an unstable eigenmode (i.e. $\Re(\lambda) > 0$). We refer to such an R as R_{unstable}.

The R_{unstable} are calculated using both odd and even numbers of polynomials to approximate the respective OS operators (i.e. both odd and even N). We also have in Table 4.9 the least stable eigenvalue for $R = 5000$, computed for $n = 1.25$, 1.01, 0.90, 0.50, $0.3\dot{3}$ and $\alpha = 1.02$. Here too we used both odd and even N.

From Tables 4.8 and 4.9 it is clear that for closed channel power-law flow where $1 > n \geq 0.5$ and $n > 1$ (i.e., n near 1) the eigenvalues are numerically unstable (i.e., they do not converge as N increases). However there is a definite pattern to this instability, in that the eigenvalues behave in distinct ways for odd and even N. For $n > 1$ (dilatant fluids), we find that as N increases where N is odd, R_{unstable} decreases and as N increases where N is even, R_{unstable} increases (see Table 4.8). As $|n-1|$ gets larger, these fluctuations become more extreme. ∞ denotes that there were not any numerically stable R_{unstable}.

	n					
N	1.50	1.25	1.01	0.90	0.50	$0.3\dot{3}$
180	$0.9523592 - 0.0578441i$	$-16.2554875 - 0.0522568i$	$0.2743835 - 0.0012867i$	$0.2802069 - 0.0042850i$	$1.0016598 - 0.0248568i$	$1.0108900 - 0.0154061i$
185	$0.2735872 + 0.0051688i$	$0.2732879 + 0.0029289i$	$0.2758215 - 0.0013105i$	$0.2780041 - 0.0042847i$	$1.0016046 - 0.0248745i$	$1.0108900 - 0.0154061i$
210	$0.9523572 - 0.0578431i$	$-13.8636668 - 0.0540308i$	$0.2745920 - 0.0012890i$	$0.2798876 - 0.0042823i$	$1.0016499 - 0.0248600i$	$1.0108900 - 0.0154061i$
215	$0.2731702 + 0.0052420i$	$0.2731337 + 0.0029433i$	$0.2758180 - 0.0013104i$	$0.2780279 - 0.0042845i$	$1.0016092 - 0.0248730i$	$1.0108900 - 0.0154061i$
240	$0.9523561 - 0.0578426i$	$-8.7351623 - 0.0498098i$	$0.2748073 - 0.0012917i$	$0.2796423 - 0.0042808i$	$1.0016434 - 0.0248620i$	$1.0108900 - 0.0154061i$
245	$0.2728385 + 0.0052986i$	$0.2730138 + 0.0029543i$	$0.2758153 - 0.0013104i$	$0.2780455 - 0.0042843i$	$1.0016122 - 0.0248720i$	$1.0108900 - 0.0154061i$

Table 4.9: Least stable eigenvalues for power-law fluids (4.11) — $R = 5000$ was held constant but $N = 180$, 185, 210, 215, 240, and 245. $\alpha = 1.02$. Note that the n for which the eigenmodes are numerically stable correspond with n for which R_{unstable} in Table 4.8 are numerically stable.

For $1 > n \geq 0.5$, we observe that as N increases where N is odd, R_{unstable} increases and as N increases where N is even, R_{unstable} decreases. We postulate than there exists a n_0

	n		
y	1.01	1.25	1.50
-6.2831E-03	-2.0718	-3.9694	-6.0214E+00
6.1230E-17	-2.8515	-2517.4983	-2.8190E+05
6.2831E-03	-2.0718	-3.9694	-6.0214E+00

Table 4.10: U_{yy} evaluated near $y = 0$ for power-law flows with $n = 1.01$, $n = 1.25$ and $n = 1.50$.

between 1 and 0.5 (i.e. $1 > n_0 > 0.5$) — as n approaches n_0 from above ($1 > n > n_0$ and decreasing) the numerical instability becomes more severe (see Table 4.9). As n decreases below n_0 the numerical instability becomes less severe. Curiously, the numerical instability disappears for strongly non-Newtonian fluids — the eigenvalues computed for $n < 0.5$ are numerically stable.

It seems the numerical instability observed in dilatant flows can be explained. For $n > 1$, U_{yy} is discontinuous at $y = 0$, i.e.

$$\lim_{y \to 0} U_{yy} = -\infty,$$

(see Figure 4.10), which also possibly explains why as n increases the results become more numerically unstable (the fluctuations in R_{unstable} become more extreme). The larger n the smaller (larger negative) the values of U_{yy} near 0 as illustrated in Table 4.10. However this does not explain why the eigenvalues behave differently for even and odd N. We recall that when N is even, $y = 0$ is included as a collocation point and not so when N is odd (see Section 4.1).

For $n < 1$, as n decreases below n_0 the flow profiles increase in smoothness (see Figure 4.10). These results strongly suggest that the U in (3.10) needs to be sufficiently smooth for the resulting eigenvalues to be numerically stable. $U_{yyy}(0)$ does not exist for $1 > n \geq 0.5$ ($U_{yy}(0)$ does not exist for $n > 1$) and we observe in Tables 4.8 and 4.9 that it is for these values of n that the eigenvalues are also numerically unstable. This singularity at

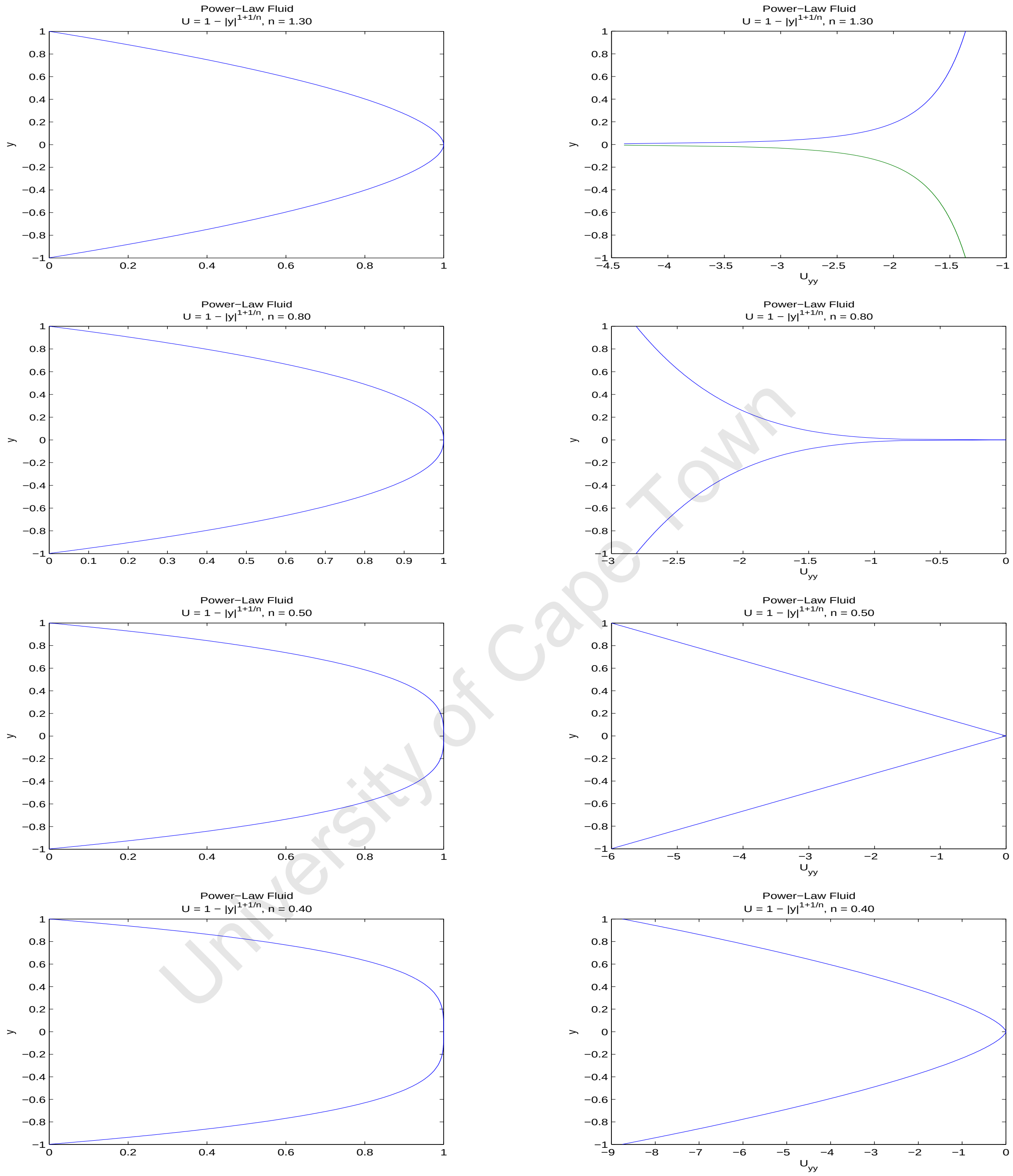

Figure 4.10: The smoothness of steady-state power-law velocity profiles for various values of n. On the left we have the power-law flow profile, U (4.11) for $n = 0.40$, 0.50, 0.80, 1.30 and on the right their corresponding U_{yy}.

$y = 0$ is also responsible for the different behaviour of the eigenmodes for odd and even N. $y = 0$ is included as a collocation point when N is even. U_{yyy} exists for $n < 0.5$ and the eigenvalues are stable.

n	R_{crit}	α_{crit}
1.00	5772.22	1.02056
0.40	37472.84	1.06500
$0.3\dot{3}$	52744.67	1.11000

Table 4.11: Critical Reynolds (R_{crit}) and wave- (α_{crit}) numbers for power-law flow (4.11) as predicted by the OS equation.

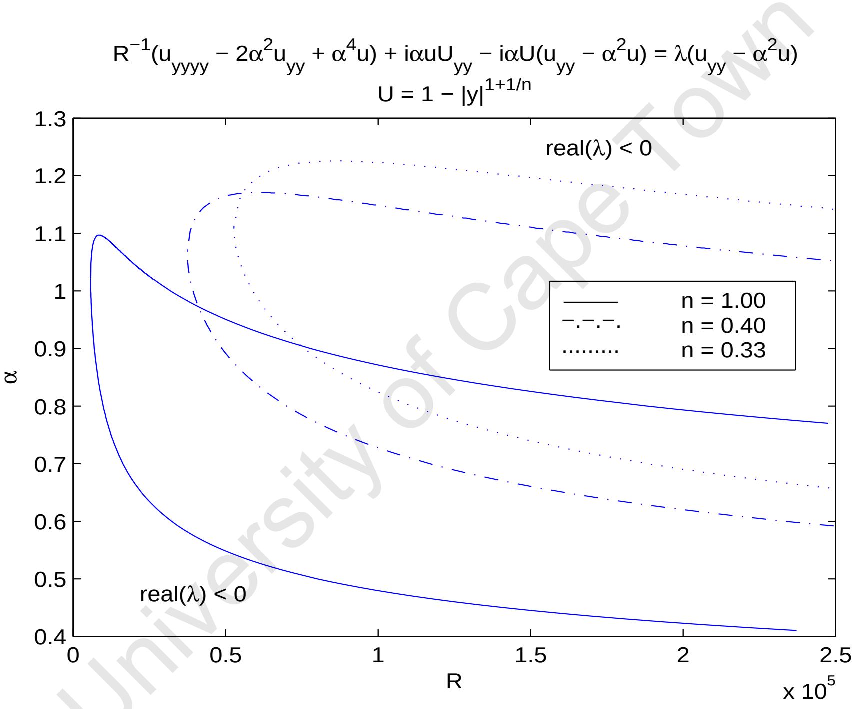

Figure 4.11: Marginal stability curves for power-law flow (4.11), approximated using the OS equation. The regions enclosed by the respective curves are the Reynolds number ranges for which unstable eigenmodes exist. $N = 150$. $n = 1.0$, 0.40 and $0.3\dot{3}$.

As explained the OS equation can possibly only be used as an approximate for the linear hydrodynamic stability of power-law fluids with n near 1. But it is for these n that the eigenvalues of the OS equation are numerically unstable. For $n < 0.5$ where the eigenvalues are stable, the Newtonian constant viscosity assumption is no longer appropriate and hence the results are unreliable (see Figure 4.9). Although the numerical instability renders any interpretation of these results rather speculative, the results seem to suggest for closed channel power-law flow (4.11) as n decreases, the critical Reynolds number at which the transition from laminar to turbulent flow is observed increases. Not only does this critical Reynolds number, R_{crit} increase, but also the critical wavenumber, α_{crit}. For Newtonian flow, i.e. $n = 1.00$, $R_{\text{crit}} = 5772.22$ and $\alpha_{\text{crit}} = 1.02056$ whereas for $n = 0.40$, $R_{\text{crit}} = 37472.84$ and $\alpha_{\text{crit}} = 1.065$ (see Table 4.11). Figure 4.11 depicts the marginal stability curves as predicted by the OS equation for power-law fluids where $n = 0.3\dot{3}$, 0.40 and 1.00. The areas enclosed by the respective curves are the Reynolds number ranges which have unstable eigenmodes associated with them, i.e. perturbations that grow with time.

The work of Hifdi *et. al.* [Hifd] done on the linear stability of channel entrance flow supports these findings for power-law flow. As part of their study they investigated the stability of sample flows akin to the two depicted in Figure 4.12. These sample profiles described as being top-hat and jet like in shape are obtained by perturbing the plane Poiseuille flow profile, i.e. $U = 1 - y^2$. The jet shape flow was obtained using $-\frac{\pi}{3}\cos\left(\pi\left(1-\frac{y}{2}\right)\right)$. Their results indicate that the top-hat shape flow is more stable than plane Poiseuille flow and the jet shape flow is less stable than the latter — more stable meaning that their respective transitions to turbulence occur at higher Reynolds numbers. The profiles of pseudoplastic power-law fluids are also top-hat in shape and we too found them to be more stable than plane Poiseuille flow. For the jet shaped dilatant flows our results were not numerically stable but may suggest that such flows would be less stable than plane Poiseuille flow. It would appear, as has likewise been deduced by Hifdi *et. al.,* that the shape of a symmetric profile influences its stability.

In Figures 4.13a - 4.13d we have the eigenvalue spectra for a power-law fluid, approximated using the OS equation with $n = 0.40$ and $\alpha = 1$. 250 polynomials were used to compute Figure 4.13a where $R = 10000$. $R = 40000$ in Figures 4.13b - 4.13d where 250, 300 and

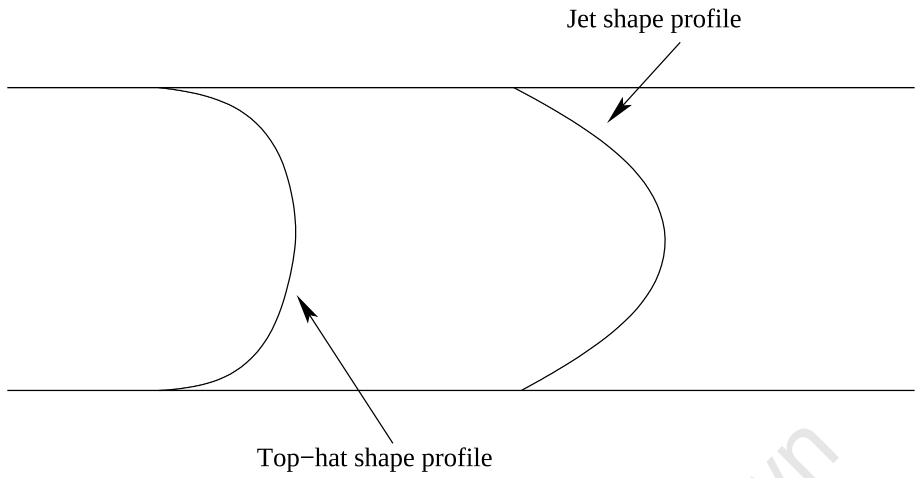

Figure 4.12: The stability of these top-hat and jet shape sample profiles were investigated by Hifdi *et. al.* [Hifd].

500 polynomials were used respectively. These power-law spectra approximations behave similarly to the plane Poiseuille spectra. Besides displaying a similar configuration, the split in the tail branch (see Figure 4.13b), is again overcome by increasing the number of polynomials used (see Figure 4.13c). The "triangle of numerical instability", at the intersection of the A, P and S branches of the spectrum (i.e. left, right and tail branches respectively) is also present. Here increasing the number of polynomials worsens the numerical instability and we postulate that as with plane Poiseuille flow employing 128-bit arithmetic will remedy the problem and result in a spectrum like the one depicted in Figure 4.13a. As observed with both plane Couette and plane Poiseuille flows, as R increases (i.e. see Figures 4.13a and 4.13c) more polynomials and a higher order of precision are required to obtain accurate spectra.

Besides its inappropriateness as a fluid model (see Section 1.3.1.1), when dealing with questions of hydrodynamic stability the power-law relation poses various numerical difficulties. As illustrated, these complications possibly stem from singularities in the respective profiles for $n > 1$ and $1 > n \geq 0.5$. In the next section we hope to extend our results by employing an alternate fluid model.

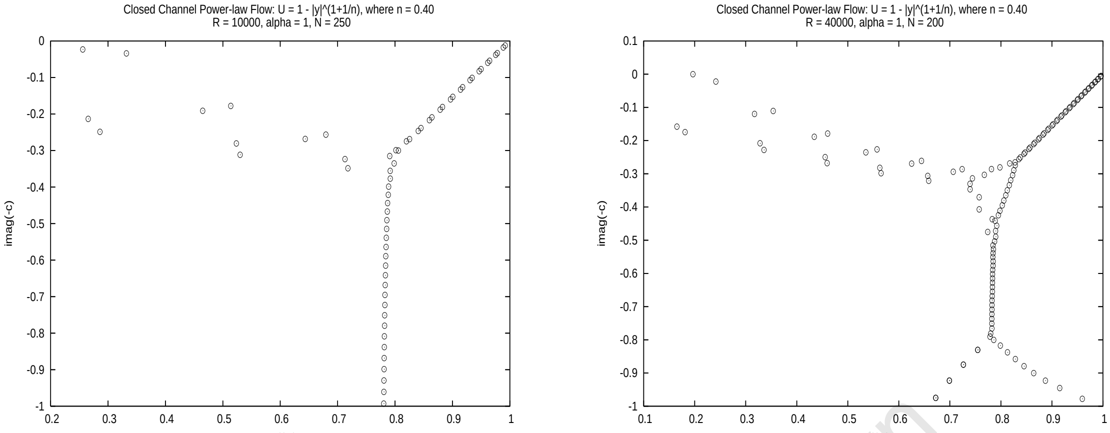

(a) $R = 10000, N = 250$ (b) $R = 40000, N = 250$

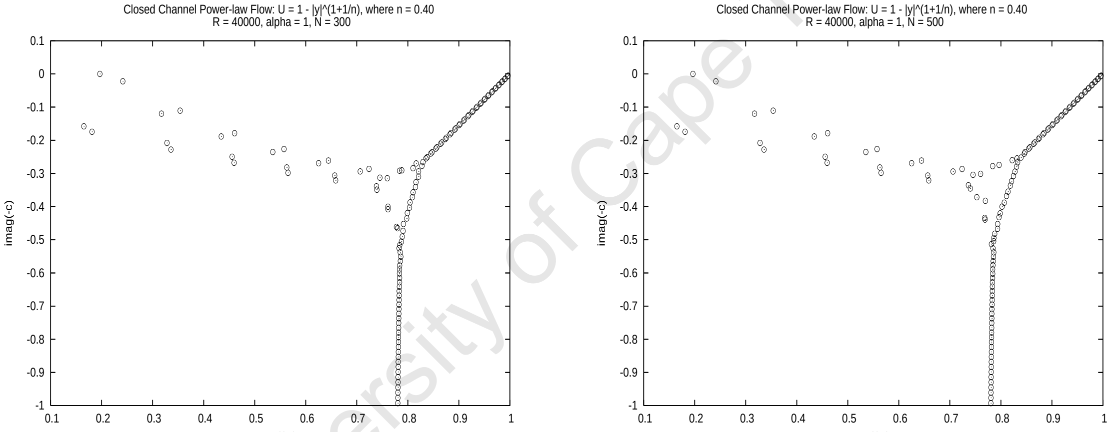

(c) $R = 40000, N = 300$ (d) $R = 40000, N = 500$

Figure 4.13: Approximate eigenvalue spectra for closed channel power-law flow ((4.11), $n = 0.4$), computed using the OS (3.10) equation. 250 polynomials were used to compute (a) with $R = 10000$. $R = 40000$ in (b) - (d) and $N = 250$, $N = 300$ and $N = 500$ respectively.

4.4.2 Closed channel Ellis flow

In Section 1.3.1.1 we showed that the power-law equation erroneously predicts that a pseudoplastic fluid approaches infinite viscosity as the shear stress τ approaches zero. To overcome this defect in its limiting behaviour, it has been proposed that an extra term be added to the power-law model. Ellis is believed to be the first to have made this suggestion [Mats]. The resulting Ellis model expresses the fluid viscosity as a function of the shear stress,

$$\frac{1}{\eta} = \frac{1}{\eta_0}\left(1 + \left|\frac{\tau}{\tau_{1/2}}\right|^{\gamma-1}\right), \tag{4.12}$$

where η_0 is the viscosity at zero shear and $\tau_{1/2}$ is the shear stress at which the viscosity is $\eta_0/2$. $\gamma - 1$ is the slope of the line obtained when $\log\left((\eta_0/\eta) - 1\right)$ is plotted against $\log\left|\tau/\tau_{1/2}\right|$. Table 4.12 contains values of these parameters for various fluids. The Ellis model, unlike the power-law model, exhibits the proper Newtonian behaviour in the limits of zero and infinite shear stress: when $\gamma > 1$, (4.12) approaches Newtonian behaviour at low shear stresses and when $\gamma < 1$ it tends to Newtonian behaviour equation at high shear stresses. If we set $\gamma = 1$ in (4.12) then we obtain the constant viscosity Newtonian model. The power-law model can be obtained from the Ellis model using Govier and Aziz's [Govi] formulation,

$$\frac{1}{\eta} = \chi_0 + \chi_1 \left|\tau\right|^{\gamma-1}, \tag{4.13}$$

Material	η_0	γ	$\tau_{1/2}$
Polystyrene	4×10^6	3.2	1.26×10^5
Aluminum soap	89.6	5.3	69.19
Polyethylene oxide	15.25	2.7	19.918
Hydroxylethycellulose	0.22	2.073	4.93
Blood	0.056	3.4	0.026

Table 4.12: Ellis parameter values for various fluids (source: [Myer]).

where $\chi_0 = 1/\eta_0$ and $\chi_1 = \left|\tau_{1/2}\right|^{1-\gamma}/\eta_0$ and setting $\chi_0 = 0$, $\gamma = 1/n$ and $\chi_1 = (1/K)^{1/n}$ [Darb]. Pseudoplastic and dilatant fluids would therefore have $\gamma > 1$ and $0 < \gamma < 1$ respectively. We however will not be investigating any dilatant flows.

Myers [Myer] investigated how well the Carreau, power-law and Ellis viscosity models predict the free surface flow of thin films. He used the Carreau model as the benchmark, an objective being to ascertain whether the Ellis model can give similar results to the Carreau. If so the Ellis model could be used to describe the flow of fluids normally described by the Carreau. The advantage of the Ellis over the Carreau is that explicit analytic results can be obtained for both thin film flow with a single free surface and channel flow. Myers improved the correspondence between the two by altering the parameter values of the former. This resulted in the following modified Ellis equation

$$\frac{1}{\eta} = \frac{1}{\eta_0}\left(1 + \left|\frac{\tau}{\beta}\right|^{\gamma-1}\right),$$

where β is now a free parameter as opposed to the shear stress corresponding to a particular viscosity reading. We will be using the parameter values as given for both the original (4.12) and Myers's modified Ellis models.

To solve the closed channel hydrodynamic stability problem for Ellis flow we require its steady-state profile. The flow is driven by a constant pressure gradient. We derive its laminar profile by imposing no-slip at both the top and bottom channel boundaries,

$$u\left(\pm 1\right) = 0.$$

4.4.2.1 Unidirectional flow approximation for Ellis flow

In the analysis we avoid the complexities introduced by modulus signs by only considering situations where the flow profiles have at most one turning point. The flow is governed by

$$2\eta_0 u_y = p_x\left(y - y_m\right)\left(1 + \left|\frac{p_x\left(y - y_m\right)}{\beta}\right|^{\gamma-1}\right), \tag{4.14}$$

and driven in the positive x direction by a negative pressure gradient $p_x < 0$ [Myer]. The fluid velocity increases until it reaches a maximum at $y = y_m$ (i.e. $\left.u_y\right|_{y=y_m} = 0$), after which it decreases. The derivation that follows is a special case of that presented by Myers

[Myer]. When $y < y_m$, we have $u_y > 0$ and

$$2\eta_0 u_y = -p_x \left[y_m - y + \left(\frac{p_x}{\beta}\right)^{\gamma-1} (y_m - y)^\gamma \right].$$

Integrating and applying $u(-1) = 0$

$$u = -\frac{p_x}{2\eta_0} \left[\frac{(y_m+1)^2 - (y_m - y)^2}{2} + \left(-\frac{p_x}{\beta}\right)^{\gamma-1} \frac{(y_m+1)^{\gamma+1} - (y_m - y)^{\gamma+1}}{\gamma+1} \right].$$

When $y > y_m$, we have $u_y < 0$ and

$$2\eta_0 u_y = -p_x \left[y - y_m + \left(\frac{p_x}{\beta}\right)^{\gamma-1} (y - y_m)^\gamma \right].$$

Integrating and applying $u(1) = 0$

$$u = -\frac{p_x}{2\eta_0} \left[\frac{(1-y_m)^2 - (y - y_m)^2}{2} + \left(-\frac{p_x}{\beta}\right)^{\gamma-1} \frac{(1-y_m)^{\gamma+1} - (y - y_m)^{\gamma+1}}{\gamma+1} \right].$$

The fluid flux, Q in the channel is obtained by integrating the expressions for u

$$\begin{aligned} Q_1 &= \int_{-1}^{y_m} u dy = -\frac{p_x}{2\eta_0} \left[\frac{(y_m+1)^3}{3} + \left(-\frac{p_x}{\beta}\right)^{\gamma-1} \frac{(y_m+1)^{\gamma+2}}{\gamma+2} \right] \\ Q_2 &= \int_{y_m}^{1} u dy = -\frac{p_x}{2\eta_0} \left[\frac{(1-y_m)^3}{3} + \left(-\frac{p_x}{\beta}\right)^{\gamma-1} \frac{(1-y_m)^{\gamma+2}}{\gamma+2} \right], \end{aligned}$$

and adding them

$$Q = -\frac{p_x}{2\eta_0} \left[\frac{(y_m+1)^3 + (1-y_m)^3}{3} + \left(-\frac{p_x}{\beta}\right)^{\gamma-1} \frac{(y_m+1)^{\gamma+2} + (1-y_m)^{\gamma+2}}{\gamma+2} \right]. \quad (4.15)$$

From this equation alone we are unable to derive an explicit expression for p_x. By the continuity of u at $y = y_m$ we obtain

$$0 = \frac{p_x}{2\eta_0}\left[\frac{(y_m+1)^2-(1-y_m)^2}{2} + \left(-\frac{p_x}{\beta}\right)^{\gamma-1}\frac{(y_m+1)^{\gamma+1}-(1-y_m)^{\gamma+1}}{\gamma+1}\right], \tag{4.16}$$

which has the unique solution $y_m = 0$. Combining equations (4.15) and (4.16), and since $y_m = 0$ results in

$$p_x = \frac{-Q\eta_0}{\frac{1}{3}-\frac{1}{\gamma+2}}. \tag{4.17}$$

Given the fluid flux we obtain the steady-state velocity profile

$$U = -\frac{p_x}{2\eta_0}\left[\frac{1-|y|^2}{2} + \left(-\frac{p_x}{\beta}\right)^{\gamma-1}\frac{1-|y|^{\gamma+1}}{\gamma+1}\right]. \tag{4.18}$$

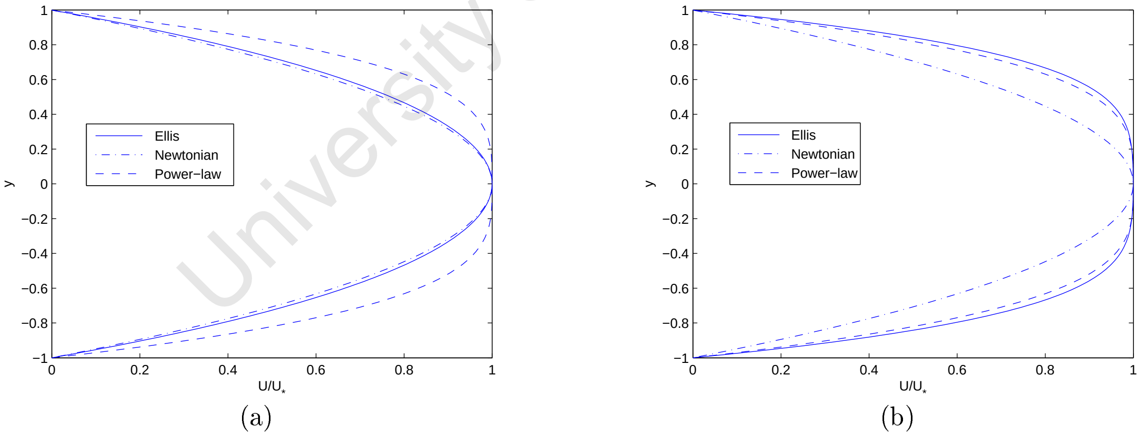

(a) (b)

Figure 4.14: Velocity profiles predicted by the Ellis (4.18), Newtonian and power-law ((4.11), $n = 0.4$) models for molten polystyrene for $Q = 0.005$ (left) and $Q = 0.05$ (right).

Both the plane Poiseuille and plane Couette OS (3.10) problems are solved with its steady-state profile, U reaching a maximum velocity of 1. In keeping with the fluid dynamics literature [Ache, Coll, Dong, Draz] for the Newtonian case, we scale the Ellis profiles using its maximum velocity obtained across the channel, U_*. Figures 4.14a and 4.14b depict the velocity profiles predicted by the Ellis, Newtonian and power-law (4.11) models for molten polystyrene for $Q = 0.005$ and $Q = 0.05$ respectively. The modified Ellis parameter values provided in [Myer] were used for this fluid (i.e. $\gamma = 3.164$ and $\beta = 1.373 \times 10^5$). $n = 0.4$ for molten polystyrene [Myer].

Unlike Newtonian and power-law channel flow, the magnitude of the fluid flux affects the shape of an Ellis flow profile (see Figures 4.14a and 4.14b). In the case of the former, the flux only influences the magnitude of the maximum velocity attained across the channel. The results for power-law flow suggest that the shape of a symmetric profile influences it's stability [Hifd]. If so, the stability of an Ellis fluid would depend on the fluid flux.

4.4.2.2 The Ellis Orr-Sommerfeld problem

As with power-law flow, we use the OS equation to study the linear stability of Ellis fluids within shear rate ranges where its rheology is weakly non-Newtonian. U in (3.10) is given by (4.18) and hence

$$U_{yy} = \frac{p_x}{\eta_0}\left[1 + \gamma\left(-\frac{p_x}{\beta}\right)^{\gamma-1}|y|^{\gamma-1}\right].$$

We scale the velocity profiles using its maximum velocity attained across the channel, U_*. Unlike power-law the non-Newtonian character of Ellis flow depends on more than one rheological constant. In the results that follow we use the parameter values of three fluids, i.e. molten polystyrene, aluminum soap and hydroxylethycellulose. Henceforth we refer to these fluids as model molten polystyrene, model aluminum soap and model hydroxylethycellulose respectively. Figures 4.15a and 4.15b depict the Ellis viscosity curves for model aluminum soap and model molten polystyrene respectively. As mentioned before and clearly illustrated in these figures, in the limit of zero shear stress (or zero shear rate) the Ellis model predicts that a fluid exhibits nearly Newtonian rheology (i.e., nearly constant viscosity). Figures 4.16a and 4.16b depict the Ellis velocity profiles for model

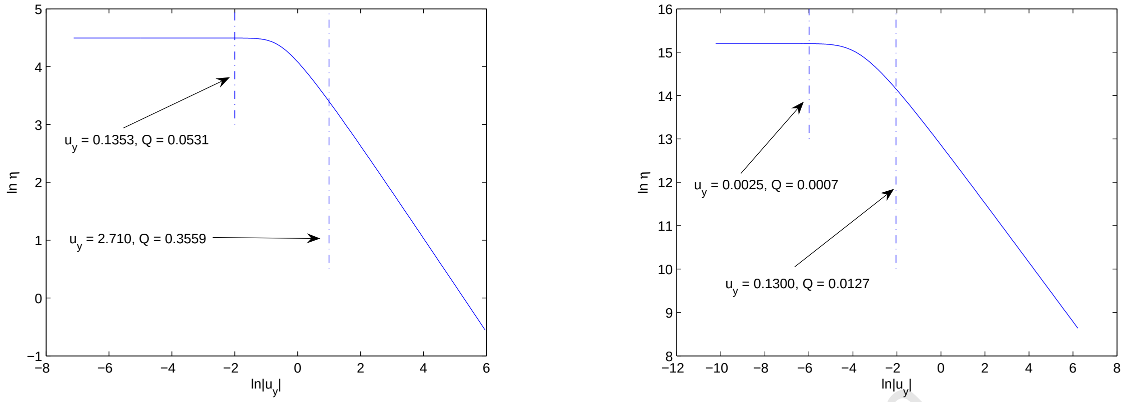

(a) (b)

Figure 4.15: Ellis viscosity curves for (a) aluminum soap and (b) molten polystyrene.

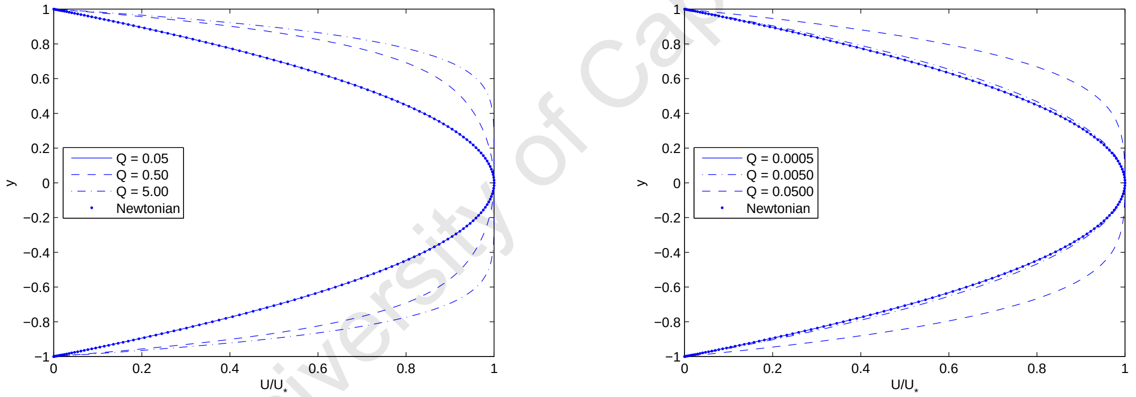

(a) (b)

Figure 4.16: Aluminum soap (a) and molten polystyrene (b) velocity profiles (4.18) for various Q, along with the Newtonian plane Poiseuille profile.

aluminum soap and model molten polystyrene respectively, along with the Newtonian plane Poiseuille profile. The shear rate, u_y depends on the fluid flux, Q (see equations (4.14) and (4.17)) and these figures show how these fluids deviate from the Newtonian norm as Q increases. The OS equation could therefore form a reliable estimate for the stability of Ellis flow below some critical shear rate, beyond which the Newtonian assumption would no longer be appropriate. Figures 4.15a and 4.15b demarcate the shear rate region

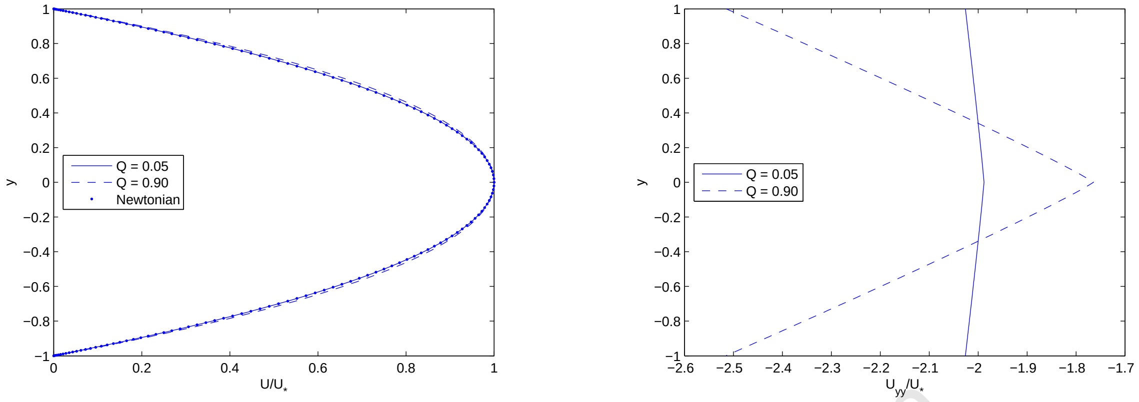

(a) (b)

Figure 4.17: (a) Model hydroxylethycellulose velocity profiles (4.18) for various Q, along with the Newtonian plane Poiseuille profile and their corresponding (b) U_{yy}.

for model aluminum soap and model molten polystyrene, along with the corresponding Q wherein which the Newtonian rheology breaks down. The critical shear rate would lie in this range.

Table 4.13 shows the R_{unstable} for model aluminum soap, model molten polystyrene and model hydroxylethycellulose. Given α, R_{unstable} is the least Reynolds number with an unstable eigenmode. We used $\alpha = 1$ and $N = 150$, 200, 300, 400 and 500. In Figures 4.17a and 4.17b, we have for $Q = 0.05$ and $Q = 0.90$, the Ellis velocity profiles for model hydroxylethycellulose and its second derivatives respectively. They show along with Table 4.13, that if U is not sufficiently smooth then the eigenvalues are not numerically stable (see model hydroxylethycellulose for $Q = 0.90$). We will be omitting model hydroxylethycellulose from further calculations.

At low shear rates we find as expected for model aluminum soap and model molten polystyrene, that the flow becomes unstable at an R near the Newtonian $R_{\text{crit}} \equiv 5772.22$. $R_{\text{crit}} = 5772.25$ (for $Q = 0.005$) and $R_{\text{crit}} = 5772.50$ (for $Q = 0.00005$) for model aluminum soap and model molten polystyrene respectively. Both these shear rates lie well within the Newtonian range of the respective fluids (see Figures 4.15a and 4.15b). As the fluid flux increases R_{crit} increases and α_{crit} decreases (see Table 4.14). Numerically stable results are obtained for weakly non-Newtonian Ellis flows provided the steady-state profile is sufficiently smooth. U_{yyy} is not continuous for weakly non-Newtonian power-law profiles and the corresponding eigenvalues are numerically unstable. The Newtonian assumption is not appropriate for power-law profiles for which the OS eigenvalues are numerically stable. The OS equation therefore does not provide a reliable analysis of the linear hydrodynamic stability of weakly non-Newtonian flows when using the power-law model. These results seem to indicate that the Ellis is superior to the power-law model in this regard.

Model aluminum soap					
	N				
Q	100	200	300	400	500
0.0050	5814.83	5814.83	5814.83	5814.83	5814.83
0.0500	5827.98	5827.98	5827.98	5827.98	5827.98
0.1272	6612.48	6612.48	6612.48	6612.48	6612.48
Model molten polystyrene					
	N				
Q	100	200	300	400	500
0.0005	5849.60	5849.60	5849.60	5849.60	5849.60
0.0026	7146.62	7146.62	7146.62	7146.62	7146.62
Model hydroxylethycellulose					
	N				
Q	100	200	300	400	500
0.0005	5815.61	5815.61	5815.61	5815.61	5815.61
0.0050	5824.02	5824.02	5824.02	5824.02	5824.02
0.0500	5923.60	5923.60	5923.60	5923.60	5923.60

Table 4.13: R_{unstable} (the least R with an unstable eigenmode), computed using the OS equation with 100, 200, 300, 400 and 500 polynomials for model aluminum soap, model molten polystyrene and model hydroxylethycellulose. $\alpha = 1$.

We conclude by investigating the behaviour of the eigenvalues that result from approximating the linear stability of weakly non-Newtonian Ellis flows with the OS equation. Fig-

Model aluminum soap			Model molten polystyrene		
Q	α_{crit}	R_{crit}	Q	α_{crit}	R_{crit}
0.0050	1.021	5772.25	0.00005	1.021	5772.50
0.0500	1.020	5786.46	0.00050	1.020	5809.28
0.1272	1.004	6610.58	0.00260	0.999	7146.62
0.2000	0.927	13847.70	0.00500	0.960	11921.27

Table 4.14: Critical Reynolds and wave- numbers for model aluminum soap and model molten polystyrene, approximated using the OS equation. $N = 300$.

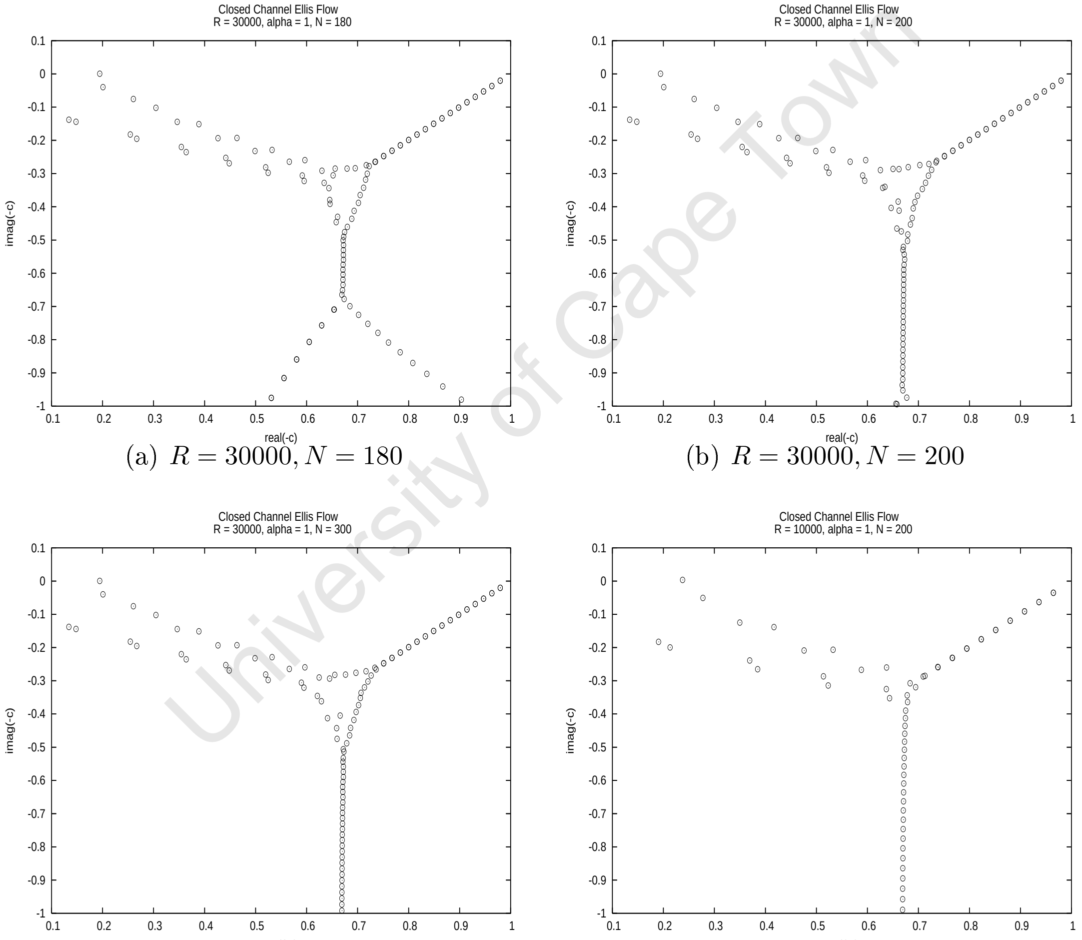

(a) $R = 30000, N = 180$

(b) $R = 30000, N = 200$

(c) $R = 30000, N = 300$

(d) $R = 10000, N = 200$

Figure 4.18: Approximate Ellis eigenvalue spectra for the closed channel flow of model molten polystyrene, computed using the OS equation. We vary R and the number of polynomials N employed in the approximations. $Q = 0.001$, $\alpha = 1$.

ures 4.18a - 4.18d depict the approximate eigenvalue spectra for model molten polystyrene. They were computed for $N = 180$, 200, 300 and 200 respectively and $Q = 0.001$. $R = 30000$ in Figures 4.18a - 4.18c and $R = 10000$ in Figure 4.18d. The approximate Ellis eigenvalues behave no differently than the Newtonian and power-law eigenvalues, exhibiting the same structure with the A, P and S branches as N varies. For $R = 30000$ the split in the S branch (i.e. tail) is resolved by increasing the number of the polynomials employed (see Figures 4.18a and 4.18b). The triangle of instability at the intersection of the three branches results from rounding errors. Increasing the precision to 128-bit arithmetic for $R = 30000$ is expected to result in a spectrum with the same structure as that computed for $R = 10000$ (see Figure 4.18d). When we increase the number of polynomials as we do in Figure 4.18c the observed gets worse.

The OS equation describes the growth of infinitesimal disturbances to the Newtonian Navier-Stokes equation. Solutions to the OS equation depend only on the boundary conditions and steady-state flow approximation of the flow. We investigated the linear hydrodynamic stability of Newtonian closed channel flows (i.e. plane Poiseuille and plane Couette), Newtonian open channel flow and weakly non-Newtonian closed channel flows by solving the OS equation for their respective flow profiles and boundary conditions. A pseudospectral differentiation technique developed by Trefethen [Tref 01] was used to determine the modes of these OS operators. Plane Poiseuille flow as documented in the relevant literature was found to be stable for Reynolds numbers less than 5772.22 and plane Couette was found to be stable for all Reynolds numbers [Ache, Chap, Draz, Schm, Tref 01].

Gravity driven Newtonian open channel flow down an incline was approximated using pressure driven flow in a channel half-filled with fluid. Using this hypothetical scenario our results seemed to suggest that Newtonian flow channel is stable for all Reynolds numbers. Our analysis does not include the instabilities that arise from variations in the free surface which may account for the inconsistencies with the instabilibilties observed in practise for this flow.

We used the power-law and Ellis models to investigate the stability of weakly non-Newtonian closed flows. These results indicate that flow profiles need to be suffciently smooth to yield numerically stable modes. Weakly non-Newtonian power-law flows are those with n near 1, but it is for these n that the power-law profiles are not sufficiently smooth. The eigenmodes for $n \leq 0.5$ were numerically stable. Although inferences from results for these n are highly speculative, since the assumptions of weakly non-Newtonian flow no longer hold, they suggest along with the numerically unstable results near 1 that pseudoplastic closed channel flow is more stable than Newtonian closed channel flow. As n decreases power-law flows becomes more stable. This same result was found to hold for weakly non-Newtonian Ellis flow.

Hwang *et. al.* [Hwan] and Rousset *et. al.* [Rous] investigated the linear stability of non-Newtonian power-law and pseudoplastic Carreau flows down an inclined plane respectively. Hwang *et. al.*'s results show that decreasing n in the power-law model destabilises the flow. They used the integral method to derive nonlinear evolution equations about the film thickness and local flow. The method of normal mode was then applied to linearised evolution equations to determine the onset of instability. Rousset *et. al.* derived a generalised eigenvalue problem by discretising the OS equation. They showed that the stability of a fluid depends on the angle of inclination of the slope. The cot of this angle is proportional to the critical Reynolds number. This proportionality factor decreases when the flow becomes more pseudoplastic. In our analysis increasing the angle of inclination of the slope amounts to decreasing the negative pressure gradient that drives the flow. This would increase the maximum velocity attained across the channel. For the closed channel

Newtonian OS problem it can easily be shown that an increase in the maximum velocity across the channel results in a proportional decrease in the critical Reynolds number, i.e. increasing the pressure gradient decreases the stability of the flow. Both these analyses [Hwan, Rous] model variations in the free surface and the angle of the slope; and their effects on the stability of the respective flows. Our model only accounts for viscous effects.

Bibliography

[Abdu] Abdullah A. A. & Lindsay K. A., 1991. *Some remarks on the computation of the eigenvalue of linear systems.* Math. Models Methods Appl. Sci. 1, 153-165.

[Ache] Acheson D. J., 1990. *Elementary fluid dynamics.* Oxford University Press: Oxford.

[Bake] Baker P. J. & Jacobs B. E. A., 1979. *A guide to slurry pipeline systems.* BHRA Fluid Engineering: Cranfield.

[Berl] Berlamont J. & Verreet G., 1988. *Rheology and non-Newtonian behaviour of sea and estuarine mud,* in Cheremisinoff N. P. (ed.). Encyclopedia of fluid mechanics - Volume 7 - Rheology and non-Newtonian flows. Gulf: Houston.

[Brow] Brown G. G. & Associates, 1950. *Unit Operations.* John Wiley & Sons, Inc.: New York.

[Chan] Chanson H., 1999. *The hydraulics of open channel flow*, Chapter 4. Wiley: New York.

[Chap] Chapman S. J., 2002. *Subcritical transition in channel flow.* Journal of Fluid Mechanics 451, 35-97.

[Char 1] Charpin J. P. F. & Myers T. G., 2005. *Modelling thin film flow with erosion and deposition.* Advances in Water Resources 28, 761-772.

[Char 2] Charpin J. P. F., Myers T. G., Lombe M. & de Hill P, 2006. *Transportation of a water based slurry in an open furrow launder or stream.* Technical Report.

[Clap] Clapp R. M, 1961. *Turbulent heat transfer in pseudoplastic non-Newtonian fluids.* International Developments in Heat Transfer 3, 652.

[Coll] Collins G. E., 2002. *The Orr-Sommerfeld equation: Classical and modern techniques.* PhD thesis, University of California, Santa Barbara.

[Cour] Course Team, 1984. *Mathematical methods and fluid mechanics. Unit 1, Properties of a fluid.* Open University Press: Milton Keynes.

[Cous] Coussot P, 1997. *Mudflow rheology and dynamics.* Balkema: Rotterdam.

[Darb] Darby R, 1988. *Hydrodynamics of slurries and suspensions,* in Cheremisinoff N. P. (ed.). Encyclopedia of fluid mechanics - Volume 5 - Slurry flow technology. Gulf: Houston.

[Dong] Dongarra J. J., Straughan B & Walker D. W., 1996. *Chebyshev tau-QZ algorithm methods for calculating spectra of hydrodynamic stability problems.* Applied Numerical Mathematics 22, 399-434.

[Draz] Drazin P. G. & Reid W. H., 1981. *Hydrodynamic stability.* Cambridge University Press: Cambridge.

[Duto] du Toit, H., 1986. *Finite element analysis of eigenvalue problems in the stability of fluid motions.* Masters thesis, University of Cape Town, Cape Town.

[Eckh] Eckhardt B., Schneider T. M., Hof B. & Westerweel J., 2007. *Turbulence transition in pipe flow.* Annu. Rev. Fluid Mech. 2007 39, 447-468.

[Famu] Famularo J. & Happel J., 1965. *Sedimentation of dilute suspensions in creeping motion.* AIChE Journal 11 (6), 981-988.

[Frie] Friedlander S. & Yudovich V., 1999. *Instabilities in fluid motion.* Notices of the AMS 46 (11), 1358-1366.

[Gott 84] Gottlieb D., Hussaini M. Y. & Orszag S. A, 1984. *Introduction: Theory and applications of spectral methods,* in Voight R. G., Gottlieb D. & Hussaini M. Y. (eds.). Spectral methods for partial differential equations. Siam: Philadelphia.

[Gott 77] Gottlieb D. & Orszag S. A., 1977. *Numerical analysis of spectral methods: Theory and application*s. SIAM: Philadelphia.

[Govi] Govier G. W. & Aziz K., 1977. *The flow of complex mixtures in pipes.* Krieger: Florida.

[Hifd] Hifdi A., Touhami M. O & Naciri J. K, 2004. *Channel entrance flow and its linear stability.* Journal of Statistical Mechanics: Theory and Experiment, P06003.

[Huan] Huang W. & Sloan M. H., 1994. *The pseudospectral method for solving differential eigenvalue problems.* Journal of Computational Physics 111, 399-409.

[Hugh] Hughes W. F., 1979. *An introduction to viscous flow.* McGraw-Hill: New York.

[Hwan] Hwang C., Chen J., Wang J. & Lin J., 1994. *Linear stability of power law liquid film flows down an inclined plane.* Journal of Applied Physics 27, 2297-2301.

[Jose] Joseph D. D., 1976. *Stability of fluid motions.* Springer-Verlag: Berlin.

[Juli] Julien P. Y., 1994. *Erosion and Sedimentation.* Cambridge University Press: Cambridge.

[Kita] Kitanovski A., Vuarnoz D., Ata-Ceasar D., Egolf P. W., Hansen T.M. & Doetsch C., 2004. *The fluid dynamics of ice slurry.* International Journal of Refrigeration 28, 37-50.

[Linc] Lin C. C., 1955. *The theory of hydrodynamic stability.* Cambridge University Press: Cambridge.

[Luio] Lui K. M & Ortiz E. L., 1987. *Tau method approximation solution of high-order differential eigenvalue problems defined in the complex plane, with an application to Orr-Sommerfeld stability equation.* Communications in Applied Mathematics 3, 187-194.

[Mars] Marshak S. & Prothero D. R., 2005. *Earth: Portrait of a planet (2nd Ed).* W. W. Norton: New York.

[Mats] Matsuhisa S. & Bird R. B., 1965. *Analytical and numerical solutions for laminar flow of non-Newtonian Ellis fluid.* AIChE Journal 11 (4), 588-595.

[Metz] Metzner A. B. & Reed J. C., 1955. *Flow of non-Newtonian fluids - Correlation of the laminar, transition and turbulent-flow regime.* AIChE Journal 1 (4), 434-440.

[Mill] Miller R. W., 1989. *Flow measurement engineering handbook.* McGraw-Hill: New York.

[Moor] Moore F., 1959. Brit. Ceram. Soc. Trans 58, 470-494.

[Myer] Myers T. G., 2005. *Application of non-Newtonian models to thin film flow.* Physical Review E 72, 066302.

[Nach] Nachtsheim P. R., 1964. *An initial value method for the numerical treatment of the Orr-Sommerfeld equation for the case of plane Poiseuille flow.* N.A.S.A Tech. Note, D-2414.

[Neof] Neofytou P. & Drikakis D., 2003. *Non-Newtonian flow instability in a channel with a sudden expansion.* Journal of Non-Newtonian Fluid Mechanics 111, 127-150.

[Octa] GNU Octave. www.octave.org (accessed on 09 Jan 2007).

[Orsz] Orszag S. A., 1971. *Accurate solution of the Orr-Sommerfeld stability equation.* Journal of Fluid Mechanics 50 (4), 689-703.

[Pate] Patel B. R., 1999. *Internal flows,* in Schetz J. A. & Fuhs A. E. (ed.). Fundamentals of fluid mechanics. John Wiley & Sons, Inc.: New York.

[Peer] Peerless S. J., 1967. *Basic fluid mechanics.* Pergamon Press: London.

[Perr] Perry R. H., 1984. *Perry's chemical engineering handbook.* McGraw-Hill: New York.

[Rous] Rousset F., Millet S., Botton V. & Ben Hadid H., 2007. *Temporal stability of Carreau fluid flow down an incline.* Journal of Fluids Engineering 129, 913-920.

[Ryan] Ryan N. W. & Johnson M. W., 1959. *Transition from laminar to turbulent flow in pipes.* AIChE Journal 5 (4), 433-435.

[Schm] Schmid P. J & Henningson D. S., 2001. *Stability and transition in shear flows.* Springer-Verlag: New York.

[Shen] Shen S. F., 1954. *Calculated amplified oscillations in plane Poiseuille and Blasius flows.* J. Aero. Sci. 21, 62-64.

[Slat 95] Slatter P. T., 1995. *Transitional and turbulent flow of non-Newtonian slurries in pipes.* PhD thesis, University of Cape Town, Cape Town.

[Slat 86] Slatter P. T., 1986. *The rheological characterisation of non-Newtonian slurries.* MSc thesis, University of Cape Town, Cape Town.

[Thom 87] Thomas A. D. & Wilson K. C., 1987. *New analysis of non-Newtonian turbulent flow - yield-power-law fluids.* Canadian Journal of Chemical Engineering 65, 335-338.

[Thom 85] Wilson A. D. & Thomas K. C., 1985. *A new analysis of the turbulent flow of non-Newtonian fluids.* Canadian Journal of Chemical Engineering 63, 539-546.

[Thom 64] Thomas D. G., 1964. *Transport characteristics: Part IX. Representation of periodic phenomenon on a flow regime diagram for dilute suspension transport.* AIChE Journal 10 (3), 303-308.

[Thom 61a] Thomas D. G., 1961. *Transport characteristics of suspensions: II Minimum transport velocity for flocculated suspensions.* AIChE Journal 7 (3), 423-430.

[Thom 61b] Thomas D. G., 1961. *Transport characteristics of suspensions: III Laminar flow properties of flocculated suspensions.* AIChE Journal 7 (3), 431-437.

[Thom 53] Thomas L. H., 1953. *The stability of plane Poiseuille flow.* Phys. Rev. 91, 780-783.

[Tref 01] Trefethen L. N., 2001. *Spectral methods in matlab.* Siam: Philadelphia.

[Tref 93] Trefethen L. N., Trefethen A. E., Reddy S. C. & Driscoll T. A., 1993. Hydrodynamic stability without eigenvalues. Science 261 (5121), 578-587.

[Vlas] Vlasak P. & Chara Z., 1999. *Laminar and turbulent experiments with yield-power law slurries.* Power Technology 104, 200-206.

[Wilc] Wilcox D. W., 2000. *Basic Fluid Mechanics (2nd Ed).* DCW Industries: California.

[Xujg] Xu J., Gillies R., Small M. & Shook C. A., 1993. *Laminar and turbulent flow of kaolin slurries.* 12thInternational conference on slurry handling and pipeline transport . Hydrotransport 12, 595.

[Yama] Yamaguchi H., 2008. *Engineering fluid mechanics.* Springer: Dordrecht.

[Zhan] Zhang J., 1998. *Study notes for CPE 124: Particle technology.* http://lorien.ncl.ac.uk/ming/particle/cpe124main.htm (accessed on 26 Jan 2006).

Appendix A

```
% CHEB compute D = differentiation matrix, x = Chebyshev grid
% Author: Trefethen [Tref]
function [D,x] = cheb(N)
        if N==0
            D=0;
            x=1;
            return
        end

        x = cos(pi*(0:N)/N)';
        c = [2; ones(N-1,1); 2].*(-1).^(0:N)';
        X = repmat(x,1,N+1); dX = X-X';
        D = (c*(1./c)')./(dX+(eye(N+1))); % off-diagonal entries
        D = D - diag(sum(D')); % diagonal entries
```

Appendix B

```
% ORRSOM
% Author: Trefethen [Tref]
% Modified: Zareer van der Fort
N = 100; alpha = 1.02; R = 5773; I = eye(N-1);

% 2nd- and 4th-order differentiation matrices:
[D,x] = cheb(N); D2 = D^2;

S = diag([0; 1 ./(1-x(2:N).^2); 0]);
D4 = (diag(1-x.^2)*D^4 - 8*diag(x)*D^3 - 12*D^2)*S;

D2 = D2(2:N,2:N);
D4 = D4(2:N,2:N);

% Orr-Sommerfeld operators A,B and eigenvalues:
A = (D4 - 2*(alpha^2)*D2 + (alpha^4)*I)/R - 2i*alpha*I ...
    - 1i*alpha*diag(1-x(2:N).^2)*(D2-(alpha^2)*I);
B = D2-(alpha^2)*I;

[ee] = eig(inv(B)*A);
```